ABSTRACT

Title of Dissertation:	HYDROGEN SEPARATION AND CARBON CAPTURE BY CARBON MOLECULAR SIEVE MEMBRANES DERIVED FROM INTERFACIALLY POLYMERIZED POLYARAMIDS
	Gaurav Murali Iyer Doctor of Philosophy, 2023
Dissertation directed by:	Professor Chen Zhang, Dept of Chemical and Biomolecular Engineering

Due to its high energy density and zero-emission combustion, hydrogen (H_2) has emerged as a clean fuel for energy generation and transportation. Also, H_2 is an important chemical used in petrochemical refining, metal production, and fertilizer manufacture. In the United States, more than 10 million metric tons of H_2 is produced each year by steam methane reforming, which gives 100 million metric tons of carbon dioxide (CO_2) by-product. Downstream H_2/CO_2 separation is therefore needed to produce high-purity H_2 product while simultaneously capturing the CO_2 by-product. State-of-the-art separation technologies such as pressure-swing adsorption (PSA) and amine absorption are energy intensive with large footprints. Membrane-based H_2/CO_2 separation provides an energy-efficient alternative with smaller footprints. Commercial implementation of membrane-based H_2/CO_2 separation requires scalable membranes with high H_2/CO_2 selectivity to produce high-purity H_2 product.

The overarching goal of this PhD dissertation is to understand the formation and pore structure-transport property relationships in novel carbon molecular sieve (CMS) membranes derived from interfacially polymerized aromatic polyamides (polyaramids) for H_2/CO_2 separation.

Polyaramid precursor hollow fiber membranes were fabricated by solution spinning of an uncrosslinked polyaramid precursor synthesized by stirred interfacial polymerization, which gave polyaramid-derived CMS membranes following pyrolysis. The formation, pore structure, and transport properties of the novel polyaramid-derived CMS membranes were systematically investigated. The polyaramid-derived CMS membrane pyrolyzed at 925 °C showed unprecedented H_2/CO_2 separation performance under single-gas permeation. Further increasing the pyrolysis temperature to 1050 °C dramatically enhanced the mixed-gas H_2/CO_2 separation factor to more than one order of magnitude higher than the most selective CMS membrane reported in literature. Modeling further demonstrates the attractiveness of the polyaramid-derived CMS membrane for enrichment of highly-pure H_2 from the reaction product of steam methane reforming. Finally, the effect of precursor amide moiety on CMS membrane pore structure and transport properties was studied by comparing the polyaramid-derived CMS membrane with CMS membranes derived from a polyimide precursor and a polyamide-imide copolymer precursor under identical pyrolysis conditions. The results show that introducing precursor amide moiety is a powerful tool to tailor the H_2/CO_2 transport properties of CMS membranes via controlling the precursor hydrogen bonding and CMS membrane pore structure.

HYDROGEN SEPARATION AND CARBON CAPTURE BY CARBON MOLECULAR SIEVE MEMBRANES DERIVED FROM INTERFACIALLY POLYMERIZED POLYARAMIDS

by

Gaurav Murali Iyer

Dissertation submitted to the Faculty of the Graduate School of the
University of Maryland, College Park, in partial fulfillment
of the requirements for the degree of
Doctor of Philosophy
2023

Advisory Committee:
Professor Chen Zhang, Dept of Chemical & Biomolecular Engineering, Chair
Professor Srinivasa R. Raghavan, Dept of Chemical & Biomolecular Engineering
Professor Kyu Yong Choi, Dept of Chemical & Biomolecular Engineering
Professor Taylor J. Woehl, Dept of Chemical & Biomolecular Engineering
Professor Robert M. Briber, Dept of Materials Science & Engineering, Dean's Representative

This dissertation is dedicated to my parents and grandparents for their unconditional love and support.

Acknowledgements

The past five years of my PhD life at University of Maryland – College Park have played an important role in my personal and professional development. First and foremost, I would like to express my humblest gratitude to my PhD advisor – Prof. Chen Zhang for allowing me to pursue my PhD studies and research as a part of his group. This PhD would not have been possible without his continued guidance, support, and encouragement throughout my PhD tenure. He has been next to a parent for me, and I cannot thank him enough. His work ethic, professionalism and dedication and humility will continue to inspire me throughout my professional career. I would like to thank all my lab members – Lu Liu, Ching-En Ku and Joseph Whitmore for all their help provided on the research activities throughout my PhD research.

Besides my advisor and lab members, I would like to thank all my committee members: Prof. Srinivasa Raghavan, Prof. Kyu Yong Choi, Prof. Taylor Woehl and Prof. Robert Briber for agreeing to be on my PhD Dissertation Committee and for their valuable inputs on my PhD dissertation. I would also like to acknowledge Prof. Dongxia Liu for her valuable recommendations on my PhD proposal. I would like to appreciate the support from Dr. Jiancun Rao from the AIMLab – Maryland NanoCenter, Dr. Peter Zavalij from the X-ray Crystallographic Center, and Dr. Karen Gaskell from the Surface Analysis Center for helping with the material characterization and imaging studies. Research is next to impossible without monetary support, so I would also like to thank all the funding agencies – National Science Foundation, American Chemical Society Petroleum Research Fund, United States Department of

Energy, Minta Martin Foundation and Maryland Energy Innovation Institute for supporting my research presented in this dissertation.

I am extremely indebted to my friends – Dr. Kanishk Gohil, Dr. Bhargava Teja Sallapalli, Akash Warty, Anirudh Mathur, Siddharth Raghu Srimathi, Bhuvsmita Bhargava, Tejaswi Tammareddy, Saumit Deshpande, Abhiruk Bhattacharya, Omkar Thorat, Abhishek Bhave, Aniket Bharamgonda, Kirti Khanna, Yashaarth Todi, Tejaswi Nori, Vivek Manepalli, Roshith Mittakolu (and the list goes on…) for literally being my "family away from home". The past five years of my PhD life would not have been so enjoyable, fascinating, and entertaining without all of you. I am extremely grateful to have friends like you.

Finally, I would like to thank my parents, grandparents, and relatives for their unconditional love and continued belief in me throughout my PhD.

Table of Contents

List of Tables

List of Figures

membrane was performed at 1 bar and 35°C. Permeation tests on the CMS membranes were performed at 10 bar and 35°C.

Figure 4.11: Comparing the H_2/CO_2 separation performance of polyaramid-derived CMS membrane (MTI-925) with other CMS membranes reported in literature. The labels are indicated as "polymer precursor-pyrolysis temperature".

Figure 4.12: Mixed-gas H_2/CO_2 permeation in MTI-925 using an equimolar H_2/CO_2 mixture at 2 bar and 35°C.

Figure 4.13: Comparing the H_2/CO_2 mixed-gas separation performance of aramid-derived CMS membrane with CMS membranes reported in literature.

Figure 4.14: (A) H_2 and (B) CO_2 sorption isotherms (35°C) for polyaramid-derived CMS membranes derived at different pyrolysis temperatures.

Figure 4.15: Effect of pyrolysis temperature on H_2/CO_2 ideal selectivity, diffusion selectivity, and sorption selectivity in polyaramid-derived CMS membranes.

Figure 4.16: H_2 and CO_2 permeation plots in MTI-800 and MTI-925. The insets illustrate the determination of permeation time lags (θ).

Figure 4.17: FTIR spectra of the MTI polyaramid precursor and polyaramid-derived CMS membranes.

Figure 4.18: (A) WAXD patterns of the MTI polyaramid and polyaramid-derived CMS membranes; (B) Effect of pyrolysis temperature on the bulk density of polyaramid-derived CMS membranes (The line was drawn to guide the eye). The dashed line represents the bulk density of the MTI polyaramid precursor.

Figure 4.19: Raman spectra of polyaramid-derived CMS membranes.

membranes and CMS membranes. Single-gas permeation tests on the precursor membranes was performed at 1 bar and 35°C. Single-gas permeation tests on the CMS membranes were performed at 10 bar and 35°C. Mixed-gas permeation tests on the CMS membranes were performed at 2 bar and 35°C using an equimolar H_2/CO_2 feed mixture. (Solid symbols: single-gas permeation results; hollow symbols: mixed- gas permeation results; stars: permeation results of CMS membranes; squares: permeation results of precursor polymer membranes).

Figure 6.8: (A) H_2 sorption isotherms and (B) CO_2 sorption isotherms (35°C) in CMS membranes.

Figure 6.9: H_2/CO_2 diffusion selectivity and H_2/CO_2 sorption selectivity in CMS membranes.

Figure 6.10: Characterizing the CMS membrane pore structure using CO_2 physisorption at 0°C. (A) CO_2 sorption isotherms (0°C), (B) Pore size distribution curves; (C) Cumulative pore volume.

Figure 6.11: XPS survey spectra of CMS membranes with indicated elemental composition.

Figure 6.12: High resolution XPS N1s spectra of (A) PI-derived CMS membrane; (B) PAI-derived CMS membrane and (C) PA-derived CMS membrane.

Figure 6.13: High resolution XPS O1s spectra of (A) PI-derived CMS membrane; (B) PAI-derived CMS membrane and (C) PA-derived CMS membrane.

Figure 6.14: High resolution XPS C1s spectra of (A) PI-derived CMS membrane; (B) PAI-derived CMS membrane and (C) PA-derived CMS membrane.

List of Abbreviations

SMR: Steam-methane reforming

PSA: Pressure-swing adsorption

MEA: Monoethanolamine

PZ: Piperazine

MOF: Metal-organic framework

ZIF: Zeolite imidazolate framework

PBI: Polybenzimidazole

PIM: Polymer of intrinsic microporosity

TFC: Thin-film composite

MPD: m-phenylene diamine

TMC: Trimesoyl chloride

NIPS: Non-solvent induced phase separation

RO: Reverse osmosis

FFV: Fractional free volume

IPC: Isophthaloyl chloride

TPC: Terephthaloyl chloride

CMS: Carbon molecular sieve

PA: Polyaramid

PI: Polyimide

PAI: Polyamide-imide

MTI: MPD-TPC/IPC in-house synthesized polyaramid

NMP: N-methyl pyrrolidone

THF: Tetrahydrofuran

DMAc: N,N-Dimethylacetamide

FTIR: Fourier Transform Infrared Spectroscopy

DSC: Differential Scanning Calorimetry

TGA: Thermogravimetric Analysis

WAXD: Wide-Angle X-ray Diffraction

SEM: Scanning Electron Microscopy

XPS: X-ray Photoelectron Spectroscopy

DFT: Density Functional Theory

NLDFT: Non-local Density Functional Theory

Chapter 1: Introduction

1.1 Overview of hydrogen production

As the world strives to achieve net zero emissions over the next decades, transitioning to a hydrogen-based economy is one of the key pillars in achieving the decarbonization goals of the global energy system. Hydrogen (H_2) is an important large volume chemical primarily used as a chemical feedstock in ammonia, methanol, food, and drug production, as well as in petrochemical and refinery processing. Other uses include metal fabrication, semiconductor manufacturing, glass manufacturing, and thermal processing.[1] Figure 1.1 indicates the global H_2 demand by sector, as of 2020.[2] The global H_2 demand was about 90 million tons in 2020, most of which was utilized by the refining and chemicals sectors. Refineries consumed about 40 million tons of H_2 (~44.4%) each year as feedstock and reagents or as an energy source. Chemical production demanded about 45 million tons of H_2 (~50%) each year with roughly three-quarters directed to ammonia production and one-quarter accounted for by methanol production. The iron and steel industry consumed ~ 5 million tons of H_2 each year accounting for 5.6% of the global H_2 utilization. Although H_2 offers tremendous potential as a clean energy carrier due to its high energy density (119 MJ/kg) and zero-emission combustion, the adoption of H_2 for energy-related applications such as the transport sector, H_2-based fuels, and electricity generation has been comparatively insignificant, with the uptake limited to the fuel cell electric vehicle deployment in the past decade.[3] Hence, the roadmap to achieving “Net zero by 2050” needs to observe a significant boost in rolling out hydrogen-based technologies across

many parts of the energy sector, which is only going to contribute to increasing H_2 demands across the globe over the next decades.[2]

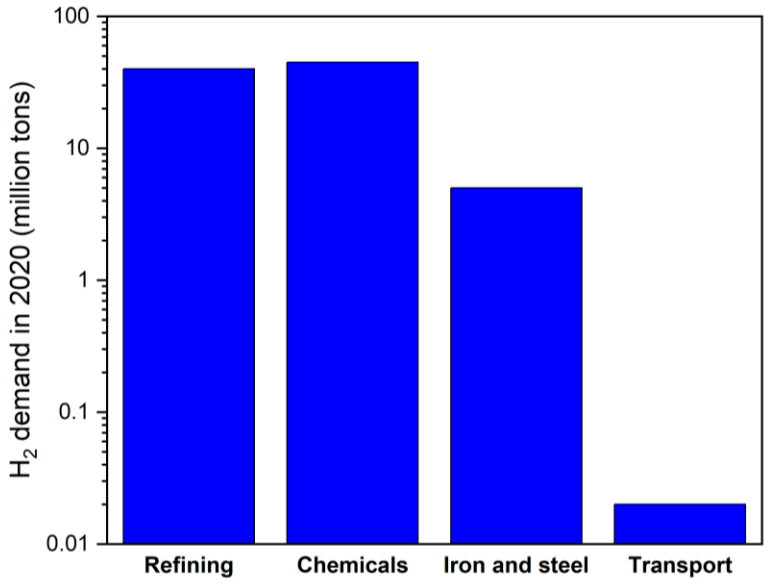

Figure 1.1: Global hydrogen demand by sector in 2020.[2]

Industrial-scale H_2 is produced by steam-methane reforming (SMR), coal gasification, and electrolysis of water.[4] Grey hydrogen is the most common form of hydrogen produced from natural gas through SMR. Blue hydrogen involves production of hydrogen from SMR or gasification accompanied by 85-95% carbon capture and storage. Green hydrogen is the cleanest form of hydrogen produced by electrolysis of water by using renewable energy sources such as solar or wind power.[5] In SMR, CH_4 in natural gas reacts with steam at high temperature (700-1000°C) and high pressure (3-25 bar) in the presence of Ni-based catalyst to produce syngas, which is predominantly a mixture of carbon monoxide (CO) and H_2. Coal gasification involves the reaction of coal with steam or oxygen under high pressures and temperatures to form syngas. CO present in the syngas produced by SMR or gasification then reacts

with steam through a series of high temperature (310-450°C) and low temperature (150-250°C) water-gas shift reactions in the presence of Fe-Cr and Cu-Zn catalysts, respectively. The water-gas shift reactors produce H_2 /CO_2 mixture at pressure exceeding 7 bar and temperature of 150-250°C[4, 6, 7] Downstream purification is required to separate H_2 and CO_2 to obtain high-purity H_2 and to capture the CO_2 to minimize carbon footprint of the process. In electrolysis of water, electricity is used to split H_2O molecules into molecular H_2 and O_2 gases, and it does not require any further purification steps.[4]

Figure 1.2 shows the percentage of annual global H_2 production and annual H_2 production in the United States by process as of 2020.[8] Globally, ~98% of the total H_2 is produced from fossil fuel feedstocks, out of which about 76% is produced by SMR while about 22% is produced by coal gasification. Electrolysis of water accounts for the remaining 2% of global H_2 production. Due to abundant low-cost shale gas, the United States relies on SMR (95%) more than coal gasification (4%) than the rest of the world for H_2 production.

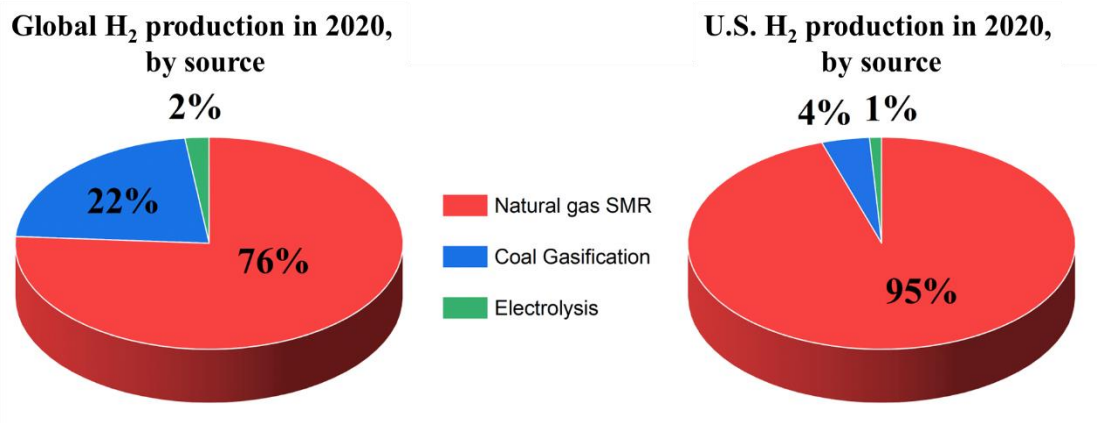

Figure 1.2: Hydrogen production in the United States and the world in 2020 by source.[8]

Steam-methane reforming ($1.43-$2.27 per kg H_2) and gasification processes ($1.16-$1.63 per kg H_2 for coal feed; $1.31-$2.06 per kg H_2 for coal/biomass feed) possess a significant economic advantage for producing large-scale blue H_2 – simultaneous H_2 production with CO_2 capture and storage. Electrolysis of water with electricity provided by renewable sources, is the most eco-friendly method to produce H_2; however, it only accounts for ~2% of global H_2 production because of its cost ineffectiveness ($5-$6 per kg of H_2). Considering the sizable economic benefit of producing H_2 from carbon-neutral processes using fossil fuel sources as against processes using zero-carbon electricity, SMR and gasification will seemingly be the most cost-effective processes for industrially producing H_2 in the foreseeable future.[8]

Hydrogen in its purest form (>99.995%) is required for aircraft and space-vehicle ground support systems. Hydrogen with >99.97% purity is required for fuel cells in vehicles while >99.9% is required for fuel cells in stationary applications. Hydrogen used as industrial fuel for power generation or as a heat source is required to be of >99.9% purity. >98% hydrogen purity is required in internal combustion engines transportation applications.[9] Hence, purifying the crude H_2 product from water gas shift reactors is important to achieve the target purity levels.

1.2 Hydrogen separation and carbon dioxide capture technologies

Figure 1.3 shows schematic process flow diagrams of H_2 production processes using steam methane reforming and coal gasification. Purification is required to treat the shifted syngas product from the low temperature water-gas shift reaction which is fed at temperatures of 150-250°C and pressures > 7 bar. For example, coal-derived syngas mainly contains ~56% H_2, ~41% CO_2 with trace quantities of H_2O vapor and

other light gases.[10] Natural gas-derived syngas in an SMR plant contains 74.1% H_2, 18.5% CO_2, 6.9% CH_4 and 0.1% CO.[1] Regardless of the production process, the downstream purification process mainly involves separation of H_2 from its major by-product CO_2 to produce a high purity H_2 product stream.

Blue hydrogen production involves simultaneous production of H_2 from conventional reforming or gasification processes along with capture and sequestration of the by-product CO_2.[11] H_2/CO_2 separation is a thermodynamic non-spontaneous process which requires large amount of energy input.[12] Therefore, to achieve economic competitiveness, developing efficient H_2/CO_2 separation processes is critical. Pressure-swing adsorption (PSA) is by far the most widely used commercial separation process to purify H_2. PSA works on the principle of selective adsorption of gases on solid adsorbents at high pressures, and desorption of gases as the pressure under reduced pressure. Due to differences in adsorption capacities, H_2 can be separated from CO_2. The major advantage of PSA is the capability to bring down the level of impurities significantly and produce up to 99.999% pure H_2 product; however its disadvantage lies in its low recovery rate of hydrogen (up to 80%) owing to the losses during the desorption step.[12-14] Cryogenic separation is another process widely commercialized for H_2 purification, which involves cooling the feed gases to extremely low temperatures below the boiling point of CO_2 (-78.5°C) allowing CO_2 to liquefy and separate to produce a purified H_2 stream. Cryogenic separation without distillation is advantageous due to high H_2 recovery and low cost; however, the H_2 product purity is compromised. Cryogenic separation with distillation improves the purity >99.5% but incurs high operating cost and energy consumption.[12-14]

The tail gas from the separation unit containing CO_2, hydrocarbons and other impurities is recycled to the reforming unit to generate heat producing flue gas exhaust containing CO_2. CO_2 from the flue gases is captured for blue H_2 production. Absorption-based separation by amine scrubbing is used for CO_2 capture.[15, 16] The most commonly studied amine solvent is monoethanolamine (MEA), while most researchers also study piperazine (PZ). CO_2 capture takes place by reactive absorption of CO_2 with the amine via carbamate and bicarbonate formation. Solvent is regenerated by heating which drives the equilibrium of the carbamate and bicarbonate formation reactions in the backward direction. However, amines are corrosive and harmful for the environment. Moreover, high temperatures can cause thermal degradation of amines and losses due to evaporation.[17]

These state-of-the-art commercialized separation technologies are energy intensive, expensive, and require large footprints. These separation technologies account for ~30% of the total H_2 production cost.[7] Hence, there is a demand for sustainable separation technologies that are more cost-effective and energy-efficient.

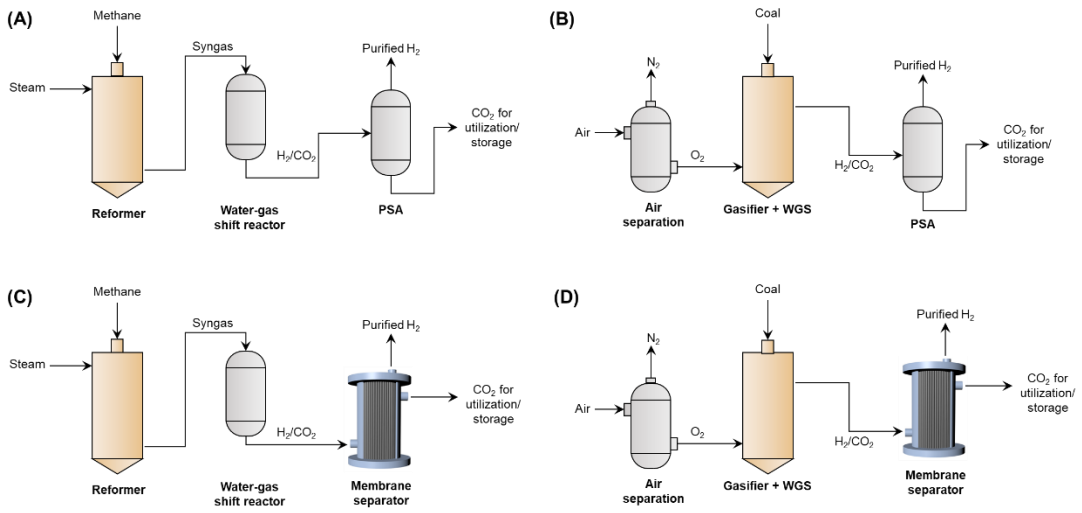

Figure 1.3: Process flow schematics showing (A) Hydrogen production using natural gas reforming with PSA; (B) Hydrogen production by coal gasification with PSA; (C) Hydrogen production by natural gas reforming with membrane separation; (D) Hydrogen production by coal gasification with membrane separation.

1.3 Membrane-based hydrogen separation and carbon dioxide capture

Membrane separation is a promising alternative to thermally driven chemical separations such as distillation and absorption. A membrane is a physical barrier that provides enriched streams by allowing selective permeation of specific components from a feed mixture. Separation by membranes relies on transmembrane pressure difference and does not require any adsorbent/absorbent regeneration or phase change, thereby incurring much smaller energy inputs compared to distillation, PSA, and amine absorption. In addition to energy efficiency, membranes are known for their modular design, small footprint, and low maintenance.

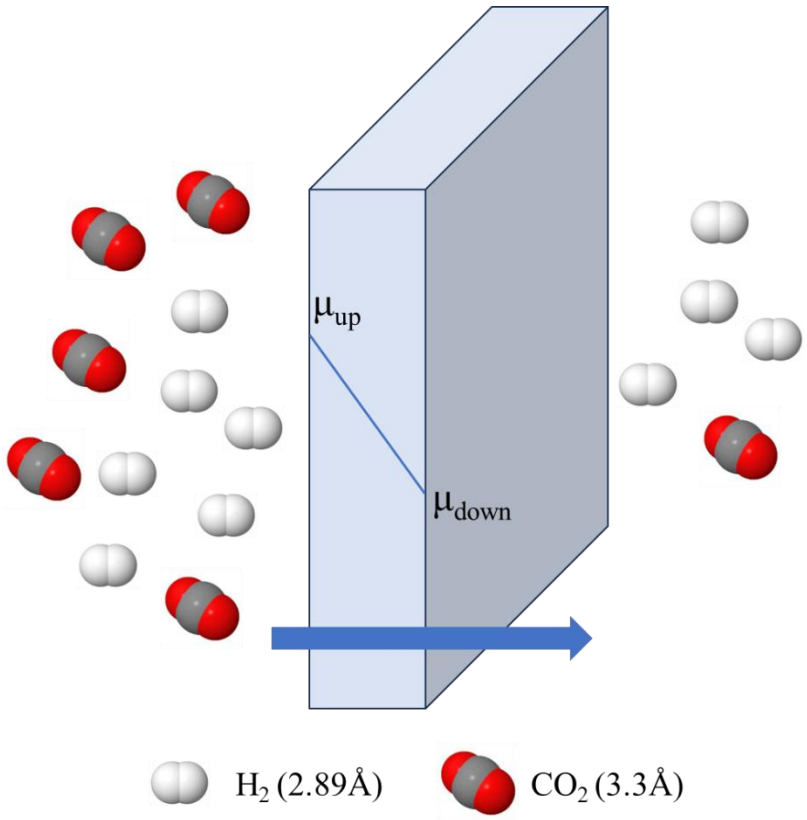

Figure 1.4: Schematic membrane-based separation process for H_2/CO_2 separation.

The key to commercialization of new membrane processes is the development of high-performance materials that can provide high gas permeability enabling small membrane separator footprint and system costs while simultaneously achieving high selectivity to enhance product purity under a given product recovery.[11] Molecular permeation through membranes often follows the sorption-diffusion mechanism, which will be discussed in detail in Chapter 2 of this dissertation. According to the sorption-diffusion theory, the permeability of a specific component can be expressed as the product of the diffusivity and sorption coefficient, while the selectivity for a specific gas pair can be expressed as the product of diffusion selectivity and sorption selectivity. The diffusivity of a component depends on its molecular size while the sorption

coefficient depends on its condensability. Table 1.1 shows the kinetic diameters (Å) and critical temperatures (K) of H_2 and CO_2. Figure 1.4 shows a schematic of membrane based H_2/CO_2 separation process. Most membrane based H_2/CO_2 separations rely on favorable H_2/CO_2 diffusion selectivity since H_2 has a smaller kinetic diameter (2.89Å) than CO_2 (3.3Å). While the kinetic diameter difference of 0.41Å is not the smallest among some other gas pairs (e.g., 0.16 Å for the N_2/CH_4 pair), H_2/CO_2 is often regarded as one of the most difficult gas pairs to separate. This is because CO_2 (critical temperature of 304 K) is much more condensable than H_2 (critical temperature of 33 K) and H_2/CO_2 sorption selectivity is thus often much smaller than unity working against the favorable H_2/CO_2 diffusion selectivity. Thus, it is critical to develop membranes with precise molecular differentiation between H_2 and CO_2 and ultra-high H_2/CO_2 diffusion selectivity.[11]

Table 1.1: Kinetic diameters and critical temperatures for H_2 and CO_2.[11]

Component	Kinetic diameter (Å)	Critical temperature (K)
H_2	2.89	33
CO_2	3.30	304

1.3 Membrane materials for H_2/CO_2 separation

The first commercially employed gas separation membrane was PRISM^{TM} membrane developed by Permea Inc., a Monsanto company in 1979, now a division of Air Products.[18] The membrane was initially used for purification of H_2 from NH_3, Ar, and CH_4 from the purge gas in the Haber-Bosch process. The application was soon extended to H_2/light hydrocarbon separations in refineries and H_2/CO ratio adjustment in syngas plants.[19] Since the introduction of gas separation membrane technology,

several industrially important membrane applications such as air separation by Air Products and Air Liquide, and natural gas treatment by Honeywell UOP have been established.[20-23]

Membrane-based H_2/CO_2 separation, however, has not been commercialized at large scale. The United States Department of Energy has set membrane performance targets for H_2 purification from syngas.[24] The economic and ecological benefits of employing a membrane based H_2/CO_2 separation discussed by Merkel and coworkers suggests that hydrogen production cost can be significantly reduced by achieving H_2/CO_2 selectivities greater than 10 in membrane applications.[25] Membrane Technology & Research Inc. has developed commercial Proteus^{TM} membrane offering H_2 mixed gas permeance of 500 GPU and H_2/CO_2 separation factor of ~11 at 150°C.[7, 26] Membrane technology has observed rapid development in the past decades driven by the advancement of membrane process engineering, with a number of membrane materials being studied by the membrane research community.

Polymeric membranes are the most commonly studied membrane materials for gas separations.[27] However, polymeric membrane materials exhibit a strong permeability-selectivity trade-off relationship, described by Robeson upper bounds, which makes it difficult to achieve simultaneous high permeability and high selectivity.[28] Specifically, commercial polymeric membranes such as cellulose acetate (Separex^{TM}), polysulfone (PRISM^{TM}) and polyimide (Ube^{TM}) have low H_2/CO_2 selectivity < 4 and therefore and not suitable for H_2/CO_2 separation.[29] Moreover, most polymeric membrane materials suffer from plasticization under high pressure highly condensable and aggressive gas feeds, making them inefficient for stable long-

term operation.[30] Several other membrane materials such as palladium[31], zeolites[32], ceramic[33], mixed-matrix[34, 35], graphene oxide[36, 37], metal-organic frameworks (MOFs)[38], zeolite imidazolate frameworks (ZIFs)[39] have been developed for H_2/CO_2 separation. Hydrogen-permeable metallic membranes made of palladium and its alloys are the most widely studied membrane materials for H_2 purification due to their high H_2 permeability, chemical compatibility with aggressive gas feeds, and their theoretically infinite hydrogen selectivity.[40] Hydrogen permeation through Pd occurs by dissociation of molecular hydrogen to monoatomic form and its rapid diffusion through the Pd lattice. Significant development has been taking place in palladium membrane development with over an order of magnitude improvement in H_2 permeance since the 1960s.[40] Graphene-based membranes have also gained significant interest due to the single atom layer thickness which can provide ultra-high H_2 permeance. Ultra-thin graphene-oxide membranes with ~1.8nm thick separation layers have shown H_2/CO_2 selectivity of 3400.[37] However, achieving commercial H_2 purification is still challenging due to several factors such as poor separation performance, expensive membrane fabrication, poor stability under realistic feed conditions, and difficulty to fabricate membranes with thin and defect-free separation layers at large scale.[41]

Carbon molecular sieve (CMS) membranes are amorphous nanoporous carbon membranes made by pyrolysis of polymeric precursor membranes. CMS membranes exhibit a unique pore structure consisting of ultramicropores (< 7Å) and micropores (7-20Å), enabling high permeability and high selectivity overcoming the Robeson upper bound for several gas separations such as O_2/N_2, CO_2/CH_4, N_2/CH_4, C_2H_4/C_2H_6,

etc.[42-44] Their rigid structure offers stability under high-temperature and high-pressure conditions, along with excellent plasticization resistance under high pressure condensable feeds containing CO_2 and hydrocarbons.[45] CMS membranes can also be fabricated in the hollow fiber format with good mechanical flexibility and strength, making them suitable for highly scalable hollow fiber modules with high packing densities.[46] Thus, CMS membranes are promising candidates for large-scale membrane applications.

CMS membranes have also been studied for H_2/CO_2 separation. CMS membrane pore structure and gas separation performance are governed by several factors, among which are polymer precursor chemistry and pyrolysis conditions.[47, 48] Several classes of polymer precursors have been studied to fabricate CMS membranes for H_2/CO_2 separation, which include polyimides[49], polybenzimidazoles (PBIs)[10], polymers of intrinsic microporosity (PIMs)[50], and cellulose-based polymers[41, 51]. Although Matrimid® polyimide-derived CMS membranes can give ultra-high H_2/CH_4 selectivity above 40000 and CO_2/CH_4 selectivity above 3600, they are not very attractive for H_2/CO_2 separation. Zhang et al. showed that Matrimid®-derived CMS hollow fiber membranes with H_2 permeability of 230 Barrer and H_2/CO_2 selectivity of 8.5.[43] Hatori et al. showed that Kapton® polyimide-derived CMS membranes with H_2/CO_2 ideal selectivity of 343 at 50°C with 2 bar feed.[49]

Polybenzimidazoles (PBIs) have been used as polymer precursors to fabricate CMS membranes for H_2/CO_2 separation. Omidvar et al. recently demonstrated PBI-derived CMS membranes at 900°C having H_2/CO_2 mixed-gas selectivity of 53 at 150°C.[10] Hu et al. showed that CMS membranes derived from PBI crosslinked with

pyrophosphoric acid (PPA) at 600°C demonstrate H_2 permeability of 140 and H_2/CO_2 selectivity of 58.[11] Hosseini and Chung developed CMS membranes from blends of PBI and Matrimid® polyimide (50:50), which provide H_2 permeability of 324 Barrer and H_2/CO_2 selectivity of 8.8 at 35°C.[52]

Cellulose-based polymers and ladder polymers like PIMs have also been studied as CMS membrane precursors for H_2/CO_2 separation. Lei et al. showed cellulose-derived CMS hollow fiber membranes with remarkable H_2/CO_2 mixed-gas selectivity of 40 at 70°C.[41, 51] Cellophane films pyrolyzed at 600°C have demonstrated H_2 permeability and H_2/CO_2 selectivity at 30°C.[53] Hazazi et al. recently reported CMS membranes derived from a ladder polymer of intrinsic microporosity - CANAL, showing H_2/CO_2 mixed-gas separation factor of 174 at 100°C.[50] Additionally Hosseini and Chung have demonstrated Torlon® polyamide-imide copolymer-derived CMS membranes at 800°C providing H_2 permeability of 390 Barrer and H_2/CO_2 selectivity of 9.1, which is the only report on polyamide-imide copolymer-derived CMS membranes for H_2/CO_2 separation.[52]

1.4 Interfacially-polymerized polymers

Synthesis of polymers by interfacial polymerization was first reported by Wittbecker and Morgan in 1959.[54] Interfacial polymerization is a facile and easily scalable technique, which commonly involves a polycondensation reaction between two highly reactive monomers dissolved in two immiscible liquids, forming a polymer product localized to the interface between the immiscible phases.[55] Polymers such as polyamides, polyesters, polyurethanes, polycarbonates, etc. can be easily synthesized by interfacial polymerization. 1,3-phenylene diamine, diaminomesitylene,

hexamethylene diamine, piperazine, 2,4-diaminobenzenesulfonic acid are some of the commonly used aqueous phase monomers for polyamide synthesis, while bisphenol-A and substituted bisphenols are commonly used aqueous phase monomers for synthesizing polyesters.[56] Sebacoyl chloride, phthaloyl chloride, isophthaloyl chloride, terephthaloyl chloride and trimesoyl chloride are commonly used organic phase monomers.[56] The polymer formation occurs on the organic phase side of the interface due to the highly unfavorable partition coefficient of the organic phase monomer into the aqueous phase. Hence, polymer formation at the interface occurs by diffusion of the aqueous phase monomer through the growing polymer layer at the interface into the organic phase. Therefore, reactants are more likely to react with the growing polymer at the interface instead of other monomers, enabling synthesis of high molecular weight polymers under ambient reaction conditions.[55, 56] Figure 1.5(A-B) shows a schematic of the interfacial polymerization reaction in unstirred and stirred systems.

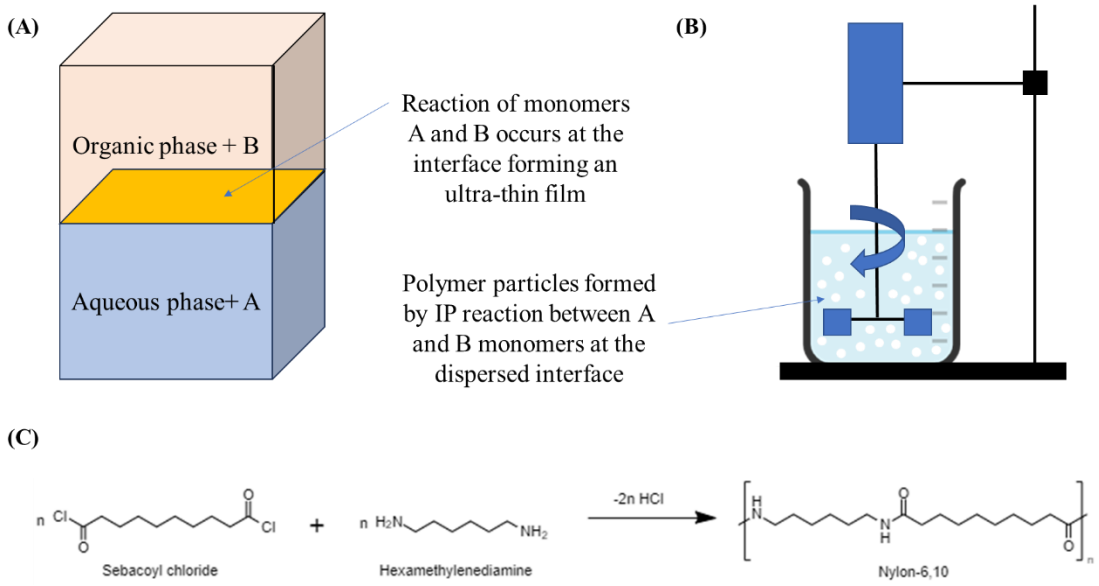

Figure 1.5: Schematic representation of the interfacial polymerization reaction in (A) unstirred and (B) stirred systems; (C) Reaction chemistry for Nylon-6,10 synthesis.[56]

A very common example of interfacial polymerization is the "nylon rope trick" experiment, which involves formation of a Nylon-6,10 polyamide film by reacting hexamethylene diamine in aqueous phase and sebacoyl chloride in organic phase, as shown in Figure 1.5C. The film can be pulled from the interface as a continuous collapsed tube.[56] Interfacial polymerization without stirring has a self-limiting nature leading to formation of an ultra-thin film at the interface. As the polymerization proceeds, the aqueous phase monomer encounters the growing polymer film which increasingly hinders the diffusion of the monomer into the organic phase, hence limiting the polymerization beyond film formation. Interfacial polymerization with stirring enables continuous replenishment of the reaction zone by repeated creation of a fresh interface for polymerization to occur. Hence, stirring significantly improves the

polymerization yield and the polymer product is obtained as a powder, as the polymer is formed at the interface of dispersed droplets.[56]

The polymer product yield and molecular weight is affected by a combination of process variables like stirring speed, concentration and purity of reactants, reaction rate, nature and purity of solvents, and additions of acid acceptors.[56] Faster stirring speed generally improves the polymer yield and molecular weight by faster replenishment of fresh interface for polymer formation. The molecular weight of the polymer synthesized by interfacial polymerization is far less sensitive to reactant non-equivalence compared to melt or solution polymerization. The reactant stoichiometry at the interface is a function of monomer concentrations, diffusivities, solubilities, and reactivities. Hence, optimization of reactant concentration for every combination of monomers is required. In general, higher monomer reactivity and lower solubility in the opposite phase is favored.[55] Monomer purity, especially of the diacid chloride monomer is an important factor affecting the polymer yield and molecular weight. Hydrolysis of the diacid chloride monomer or oligomers with diacid chloride end groups during the polymerization reaction is the principle competing side reaction.[56] The hygroscopic nature of the diacid chloride can have an adverse effect on the polymer product yield and molecular weight by causing hydrolytic attack on reaction intermediates favoring the side reaction due to moisture exposure. The polymerization reaction rate needs to be faster than the competing hydrolysis side reaction to complete the polymerization reaction before the polymer is immobilized in the precipitated state. Using polar solvents usually indicates a net gain in the polymerization rate by increasing the polarity of the medium. Although certain polar solvents can potentially

cause phase miscibility, the improvement is because of polar solvents being better solvents or swelling agents for several condensation polymers. Addition of an inorganic base in the aqueous phase acts as an acid acceptor to neutralize the acidic by-product. Hydrolysis side reaction is inhibited by using weakly alkaline acid acceptors like sodium carbonate (Na_2CO_3), contributing to improvement in polymer yield and molecular weight of the product.[56]

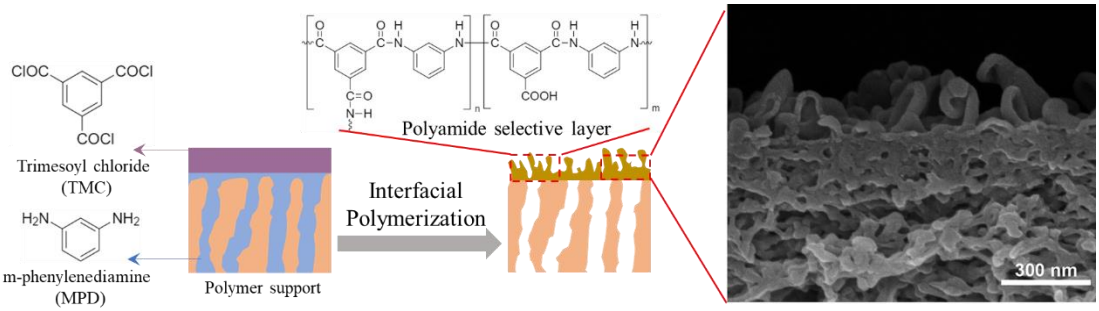

Figure 1.6: Formation process and SEM image of a polyamide selective layer by interfacial polymerization.[7]

Interfacial polymerization was pioneered by John Cadotte in the late 1970s to fabricate thin-film composite (TFC) membranes.[57] Commercially known as the FT-30 membrane, it was fabricated as a thin selective polyaramid layer by in situ interfacial polymerization using m-phenylene diamine (MPD) in the aqueous phase and trimesoyl chloride (TMC) in the organic phase, on the surface of porous polymeric supports. A schematic representation of formation of ultra-thin polyamide membrane using interfacial polymerization on porous supports along with the polyamide chemistry and SEM image of the selective layer are shown in Figure 1.6. The polymer substrate is first soaked in the aqueous phase solution containing MPD. The surface of the soaked substrate is then cleared off excess aqueous phase droplets using a rubber roller. The

substrate is then soaked in the organic phase solution for the polymerization reaction to take place at the surface of the substrate. The composite membrane is then cured at high temperature and dried.[7] Compared to the commercial cellulose acetate asymmetric membranes made by non-solvent induced phase separation (NIPS) – pioneered by Loeb and Sourirajan in the 1960s, the TFC membrane made by interfacial polymerization showed exceptional water flux and NaCl rejection for seawater and brackish water desalination, hence becoming the gold standard for RO membrane application.[58] In the past decade, these TFC membranes have been implemented across 15,000 desalination plants, accounting for about 90% of the global desalination membrane market.[7]

1.5 Polyaramid membranes for gas separations

While polyaramids are broadly used for desalination membranes and are among the most commercially successful membrane materials, they are conventionally seen as unfit for gas separation applications as they are known to exhibit low gas permeabilities under ambient conditions with dry gas feeds owing to their strong hydrogen bonds and consequently low fractional free volume (FFV).[59] Ali et al. recently developed polyaramid-derived thin-film composite membranes and studied the effect of process parameters such as polymerization reaction time, organic phase monomer concentration and reaction temperature.[7] The FT-30 membrane developed by Cadotte demonstrated Knudsen diffusion gas transport implying presence of surface defects, hence unsuitable for gas separation. However, the work by Ali et al. showed that systematically tuning the reaction time plugged the surface defects by additional polymer formation, hence providing defect-free, ultra-thin membranes with attractive

H_2/CO_2 separation performance. The ultra-thin defect-free TFC membranes demonstrated highly attractive H_2/CO_2 mixed-gas selectivity of ~50 with H_2 permeance of 350 GPU at 140°C. The H_2/CO_2 separation performance surpassed the permeance/selectivity upper bound by a significant margin.

Ekiner and Vassilatos developed monolithic asymmetric polyaramid hollow fiber membranes for H_2/CH_4 separation.[60, 61] They used the DuPont family of polyaramids with H_2 permeability ranging from 4000 to 400 centiBarrers and H_2/CH_4 selectivity ranging from 75 to 600. The polyaramids used for hollow fiber fabrication were copolymers synthesized by solution polymerization, using 50:50 mole ratio of diaminomesitylene (DAM) and MPD with a 70:30 mole ratio of IPC and TPC and 1:1 weight blend of copolymers of MPD-IPC/TPC and DAM-IPC/TPC with the same mole ratio of IPC and TPC. Hollow fiber membranes were spun from a polymer dope containing 27wt% polymer and 30wt% (based on the polymer) of $LiNO_3$ in N,N-Dimethylacetamide. The effect of spinning parameters such as fiber take-up rate and air-gap height on the gas separation performance and mechanical properties of the hollow fiber membranes were systematically studied. This is the only commercial application of polyaramid membranes for gas separation commercialized by Air Liquide as the MEDAL^{TM} membranes for high-temperature hydrogen/hydrocarbon separation.

1.5 Research objectives

Polyaramids are an overlooked class of polymer precursors for CMS membrane formation. Jones and Koros reported the formation of polyaramid-derived CMS membranes in 1994.[62] However, no details in CMS membrane structure or separation

performance were reported. Zhang and co-workers coated the outer surface of defective polyimide precursor hollow fibers by in situ interfacial polymerization of crosslinked polyaramid. Pyrolysis of the polyaramid-coated polyimide hollow fiber gave CMS hollow fiber membranes with outstanding separation performance for CO_2/CH_4 and CO_2/N_2 separation.[46, 63] This work indicated that it was possible to fabricate CMS membranes using polyaramids. More recently, White et al. studied polyaramid-derived CMS for organic solvent separation,[64] in which CMS powders were used for equilibrium and kinetic sorption measurements without formation of membranes. To the best of our knowledge, there are no reports investigating polyaramid-derived CMS membranes for separation applications prior to this PhD investigation. We hypothesize that the strong inter-chain hydrogen bonding in polyaramids can provide CMS membranes with highly refined ultramicropores and outstanding diffusion selectivity required for efficient H_2/CO_2 differentiation. Another advantage of polyaramid-derived CMS membrane is the possibility to fabricate ultra-thin CMS membranes with simultaneous high permeance and high selectivity by pyrolysis of ultra-thin interfacially polymerized polyaramid precursor membranes.

The overarching goal of this PhD dissertation is to understand the formation and pore structure-transport property relationships in novel carbon molecular sieve (CMS) membranes derived from interfacially polymerized polyaramids for H_2/CO_2 separation. The specific research objectives of this PhD dissertation are outlined below.

1. **Investigate the formation and gas transport properties of CMS membranes derived from polyaramid**

Because formation of polyaramid-derived CMS membranes have not been reported, we first investigated the polyaramid precursor chemistry suitable for CMS membrane formation and the methods to fabricate CMS membranes using polyaramid precursors. We identify conditions to synthesize a high molecular weight polyaramid by stirred interfacial polymerization. We fabricate polyaramid dense films by solution casting and characterized the polymer properties and suitability for CMS membrane formation. We also fabricate asymmetric polyaramid hollow fiber membranes by dry-jet/wet-quench spinning, which were used to provide polyaramid-derived CMS hollow fiber membranes suitable for gas permeation studies. We then systematically examined the effect of pyrolysis temperature on the pore structure and gas separation performance of polyaramid-derived CMS membranes.

2. **Investigate the H_2/CO_2 separation performance of polyaramid-derived CMS membranes under realistic syngas operating conditions.**

Following the study on the intrinsic H_2/CO_2 transport properties in Objective 1, we focus on an investigation of the membrane's H_2/CO_2 separation performance under realistic syngas operating conditions using mixed-gas feeds. The effect of operating temperature and feed pressure on the H_2 permeability and H_2/CO_2 separation factor are systematically studied. Additionally, the long-term stability of the polyaramid-derived CMS membrane under realistic syngas separation conditions is evaluated.

3. **Elucidate the role of precursor amide moiety on pore structure-transport property relationship of CMS membranes.**

Because no polyaramid-derived CMS membranes have been studied prior to this PhD work, this objective elucidates the role of precursor amide moiety on the pore structure and gas transport properties in CMS membranes. We fabricated CMS membranes using a polyimide precursor and a polyamide-imide precursor at identical pyrolysis conditions with the polyaramid-derived CMS membrane made in Objective 1. The pore structure and gas transport properties of CMS membranes derived from polyaramid, polyimide, and polyamide-imide were compared to establish correlations between precursor amide moiety and inter-chain hydrogen bonding, CMS membrane pore structure, and CMS membrane separation performance.

1.6 Dissertation organization

Following the introduction chapter, this dissertation includes six additional chapters. Chapter 2 highlights the necessary background and theory to assist understanding of the presented research in this dissertation as well as provide a literature review for CMS membranes. Chapter 3 gives a detailed description of the materials, experimental methods, equipment, and characterization techniques used in the presented research. Chapters 4-6 are the main body chapters highlighting the results and discussions pertaining to the three research objectives stated in the previous section. Chapter 4 discusses the investigation of membrane formation and separation performance in polyaramid-derived CMS membranes. Chapter 5 reports the investigation of H_2/CO_2 separation performance of polyaramid-derived CMS membranes under realistic syngas operating conditions. Chapter 6 focuses on

developing an understanding of the structure-transport property relationship based on the effect of precursor amide moieties on the CMS membranes separation performance. Chapter 7 provides a summary of the key findings in this research, along with concluding remarks and future recommendations to continue pursuing this research.

Chapter 2: Background and theory

2.1 Overview

This chapter covers the necessary background and theory behind the research presented in this dissertation. Section 2.2 highlights the theory of molecular transport through membranes including permeation, sorption, and diffusion. Section 2.3 covers the structural characteristics of carbon molecular sieve (CMS) membranes. Section 2.4 explains the formation of CMS membranes and the factors affecting the molecular transport and separation in CMS membranes. Finally, section 2.5 describes the theory of asymmetric hollow fiber membrane fabrication and discusses the key parameters affecting the fabrication process.

2.2 Gas transport in membranes

Membranes essentially act as selective barriers to gas transport. From a feed mixture of gases, a membrane selectively allows certain gaseous components to penetrate through into the permeate stream, while rejecting the other gaseous components remaining in the retentate stream. Gas transport through membranes have been found to follow several transport mechanisms: (1) Knudsen diffusion; (2) Selective surface adsorption and surface diffusion; (3) Molecular sieving; (4) sorption-diffusion.[65, 66] A schematic illustration of each of these transport mechanisms is shown in Figure 2.1.

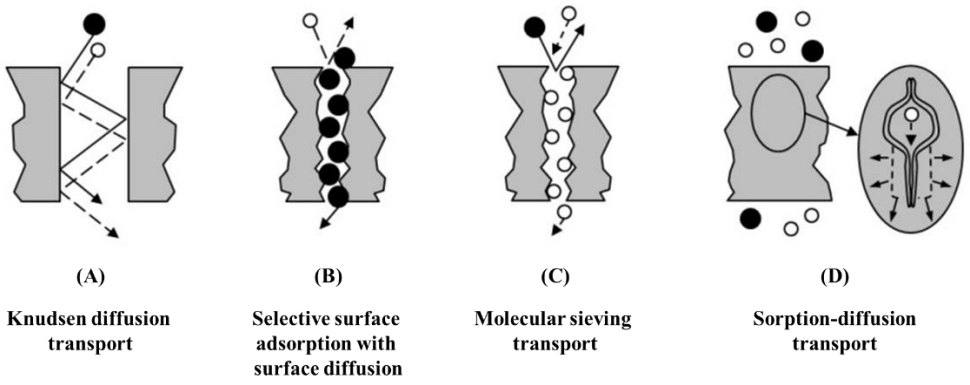

Figure 2.1: Mechanisms for selective gas transport through membranes.[65]

Knudsen diffusion of gases is known to occur when the pores in the membrane are of sizes smaller than the mean free path of the permeating gas molecules.[67] The selection between gaseous penetrants is dependent on the molecular weight of the gases as

$$\alpha_{A/B} = \sqrt{\frac{M_B}{M_A}} \tag{2.1}$$

where, $\alpha_{A/B}$ represents the Knudsen diffusion selectivity of gas A over gas B, and M_A (g/mol) and M_B (g/mol) represent the molecular weights of gas A and gas B, respectively. Selective adsorption transport is based on one of the gaseous penetrants preferentially adsorbing on the surface of the membrane and diffusing through the membrane by hopping from one sorption site to another, while the other gaseous penetrants are rejected.[65] Transport by molecular sieving takes place when gaseous penetrants are preferentially sieved by the porous structure of the membrane based on size and shape.[65, 66] Gases with the right shape and smaller size can travel through the porous structure of the membrane much faster than the other gases. In sorption-

diffusion mechanism, gas transport through the membrane is governed by both the molecular size (diffusivity) and condensability (solubility) of the penetrants. Sorption-diffusion transport is the commonly followed mechanism by polymeric and molecular sieve membranes.

2.2.1 Permeation

Gas transport in dense polymeric and CMS membranes follows sorption-diffusion transport mechanism. Figure 2.2 illustrates the assumptions made for gas transport through a membrane by sorption-diffusion mechanism. According to the sorption-diffusion mechanism, gas molecules sorb on the high-pressure upstream side of the membrane, diffuse through the membrane across a chemical potential gradient and then desorb on the low-pressure downstream side of the membrane.[66, 68] μ_1 and μ_2 represent the chemical potential of permeating species on the upstream and downstream side of the membrane, respectively; p_1 and p_2 represents the pressure on the upstream and downstream side of the membrane, respectively; l is the membrane thickness and N_A is the flux of permeation. Sorption-diffusion membrane transport mechanism assumes the pressure p_1 applied on the high-pressure upstream side to be constant throughout the membrane. Additionally, the fluid on either side of the membrane is assumed to be in equilibrium with the gas-membrane interface on either side of the membrane. The chemical potential gradient across the membrane is expressed as a concentration gradient which is the driving force for gas permeation.

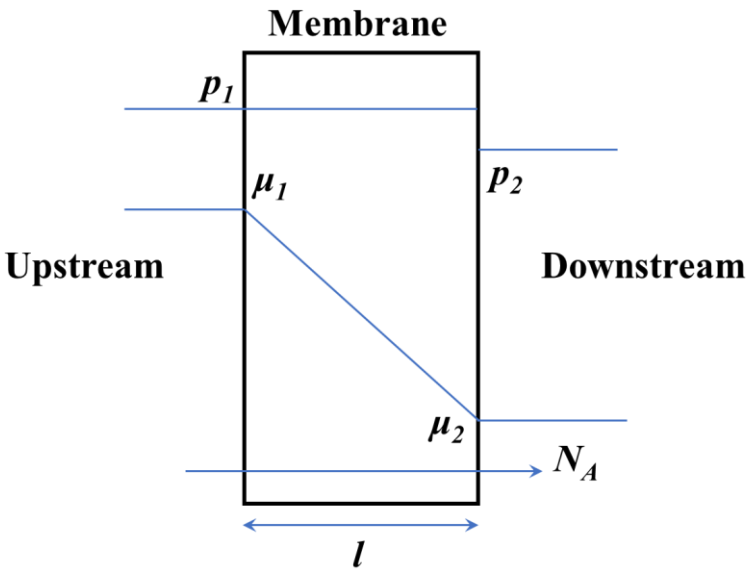

Figure 2.2: Schematic representation of the assumptions for gas permeation through dense membranes following sorption-diffusion mechanism. Reproduced from [69].

Gas permeability is used to characterize the productivity of the membrane which selectivity is used to characterize the separation efficiency of the membrane.[23, 68] Permeability of gas A is defined as the steady-state flux of gas A (N_A, $cm^3(STP)/cm^2.s$) normalized by the membrane thickness (l, cm) and trans-membrane partial pressure driving force (Δp_A, cmHg).

$$P_A = \frac{N_A \cdot l}{\Delta p_A} \tag{2.2}$$

The unit of permeability is "Barrer" defined as

$$1\ Barrer = 10^{-10}\,\frac{cm^3(STP).cm}{cm^2.s.cmHg} \tag{2.3}$$

When the membrane thickness cannot be unambiguously determined, permeance is used to characterize the productivity of the membrane, which is defined

as the steady-state permeation flux normalized by the trans-membrane partial pressure driving force.

$$\left(\frac{P}{l}\right)_A = \frac{N_A}{\Delta p_A} \tag{2.4}$$

The unit of permeance is "Gas Permeance Unit" (GPU), defined as

$$1\ GPU = 10^{-6}\frac{cm^3(STP)}{cm^2.s.cmHg} \tag{2.5}$$

Selectivity of a membrane is defined as the ratio of gas permeabilities or permeances.

$$\alpha_{A/B} = \frac{P_A}{P_B} = \frac{\left(\frac{P}{l}\right)_A}{\left(\frac{P}{l}\right)_B} \tag{2.6}$$

In the case of sorption-diffusion membranes, gas permeability can also be defined as the product of diffusivity (D_A, cm^2/s) and sorption coefficient (S_A, $cm^3(STP)/cm^3.cmHg$). Selectivity can thus be defined as the product of diffusion selectivity (D_A/D_B) and sorption selectivity (S_A/S_B).

$$P_A = D_A \cdot S_A \tag{2.7}$$

$$\alpha_{A/B} = \frac{D_A}{D_B} \cdot \frac{S_A}{S_B} \tag{2.8}$$

2.2.2 Sorption

Sorption coefficient (S_A) of a penetrant is defined as the equilibrium quantity of gas sorbed (C_A, $cm^3(STP)/cm^3$) at a particular pressure (p_A, cmHg) in the membrane.[68]

$$S_A = \frac{C_A}{p_A} \tag{2.6}$$

The sorption coefficient of gases in a membrane is strongly affected by the condensability of the gas molecule and the interaction with the sorbent. Critical temperature (T_C, K) is considered as a good measure of condensability; gases with a higher critical temperature tend to have a higher condensability and hence strongly sorbing in membranes.

In polymeric membranes, the gaseous penetrant can sorb into Henry's law regions of dense polymer matrix as well as Langmuir regions of molecular scale non-equilibrium microvoids or holes.[70] In the dense polymer matrix, sorption follows Henry's law and takes place through ordinary dissolution by dilation of the matrix. This type of sorption happens in both glassy and rubbery polymers. Langmuir sorption takes place by hole-filling in the microvoids in the polymer matrix which correspond to the non-equilibrium excess free volume in glassy polymers. Hence, sorption in glassy polymers follows dual-mode sorption model.[68, 71]

$$C_A = C_{DA} + C_{HA} = k_{DA}p_A + \frac{C'_{HA}b_A p_A}{1 + b_A p_A} \tag{2.6}$$

where, C_A (cm^3(STP)/cm^3) is the total sorbed concentration of gas penetrant A, C_{DA} (cm^3(STP)/cm^3) is the sorbed concentration in the Henry's region, C_{HA} (cm^3(STP)/cm^3) is the sorbed concentration in Langmuir region, k_{DA} (cm^3(STP)/cm^3.cmHg) is the Henry's law constant, p_A (cmHg) is the partial pressure, C_{HA}' (cm^3(STP)/cm^3) is the Langmuir sorption capacity (hole-filling) and b_A ($cmHg^{-1}$) is the Langmuir affinity constant.

However, in CMS membranes due to absence of dilation in the rigid CMS structure, gas sorption in most of the CMS membranes occurs in the CMS micropores and follow the Langmuir sorption model.[72, 73] Figure 2.3 provides a schematic plot of the sorption isotherms following different models.

$$C_A = C_{HA} = \frac{C'_{HA} b_A p_A}{1 + b_A p_A} \tag{2.7}$$

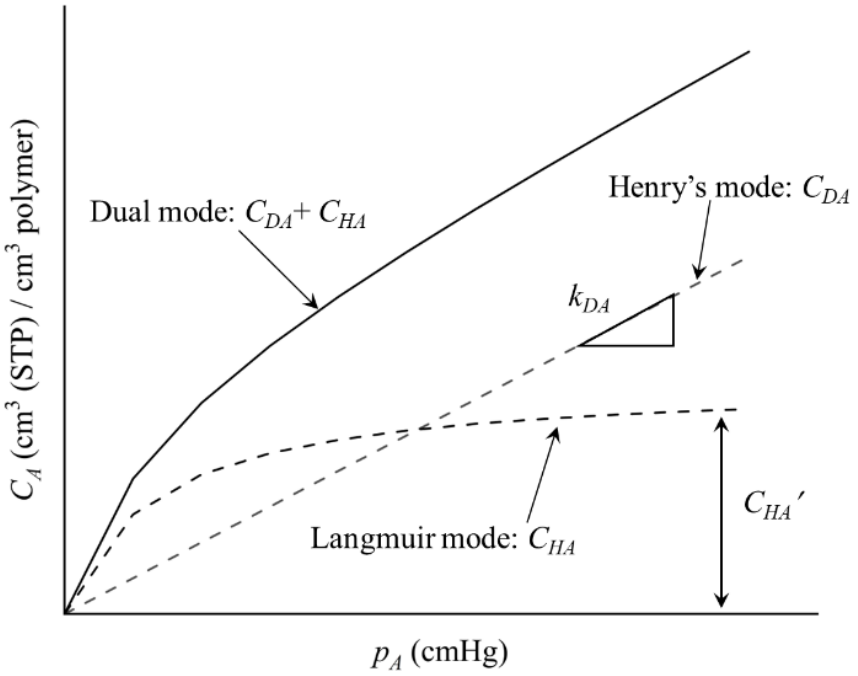

Figure 2.3: Illustration of Henry's sorption contribution and Langmuir sorption contribution to the dual-mode sorption isotherm. Reproduced from [69].

More recently, dual-mode sorption of gaseous penetrants was reported in CMS membranes.[74] Dual-mode sorption in CMS membranes occurs due to presence of majority microporous domains (Langmuir regions) in equilibrium with a small volume fraction of minority continuous phase (Henry's region). Due to the difference in physical nature of dual-mode sorption behavior in glassy polymer membranes and

CMS membranes, the Henry's region of continuous phase is referred to as "C" while the Langmuir microporous region is referred to as "L", instead of "D" (dissolved) and "H" (hole) in glassy polymers. The structural evolution of the CMS membranes is explained in greater detail in section 2.4.

Therefore, the dual-mode sorption model for CMS membranes can be expressed as

$$C_A = C_{CA} + C_{LA} = k_{CA}p_A + \frac{C'_{LA}b_A p_A}{1 + b_A p_A} \tag{2.8}$$

where, C_{CA} (cm^3(STP)/cm^3) is the sorbed concentration in the CMS continuous phase, C_{LA} (cm^3(STP)/cm^3) is the sorbed concentration in microporous Langmuir region, k_{CA} (cm^3(STP)/cm^3.cmHg) is the continuous mode's sorption constant, p_A (cmHg) is the partial pressure, C_{LA}' (cm^3(STP)/cm^3) is the Langmuir sorption capacity and b_A ($cmHg^{-1}$) is the Langmuir affinity constant.

In the case of multi-component mixtures, competitive sorption occurs as multiple components in the mixture compete to occupy the same sorption sites. Competitive sorption prefers the penetrant having a larger Langmuir affinity constant *b*. Hence, for gaseous mixtures, the dual-mode sorption model for multi-component mixtures can be modified as

$$C_i = k_{Ci}p_i + \frac{C'_{Li}b_i p_i}{1 + \sum b_i p_i} \tag{2.9}$$

2.2.3 Diffusion

Diffusion of gaseous penetrant molecules takes place through random jumps from one sorption site to the next in the membrane. Diffusivity (D_A) of gaseous

penetrant is a measure of its mobility through the membrane and is a function of jump frequency (f_A , s^{-1}) and average diffusion jump length (λ_A, cm).[71]

$$D_A = \frac{f_A \lambda_A^2}{6} \tag{2.10}$$

Diffusion of a sorbed gaseous penetrant in polymeric membranes takes place in the repeatedly created and reorganized transient gaps between the polymeric chains. These transient gaps are formed due to thermal rearrangements in the polymeric chains due to their continuous segmental motions.[68, 71] A sufficiently large dilation of the polymeric chains enables a transient gap through which the sorbed penetrant can execute a diffusion jump. Diffusion is an activated process; the sorbed penetrant is in normal state while embedded in the sorption site, whereas it is in an activated state while diffusing through the transient gap between the polymeric chains. Figure 2.4 shows diffusion of gas molecules through polymeric membranes. The factors affecting the penetrant diffusivity in polymeric membranes include the penetrant molecular size, packing between polymeric chains and mobility of polymeric chains, and the cohesive energy.[75]

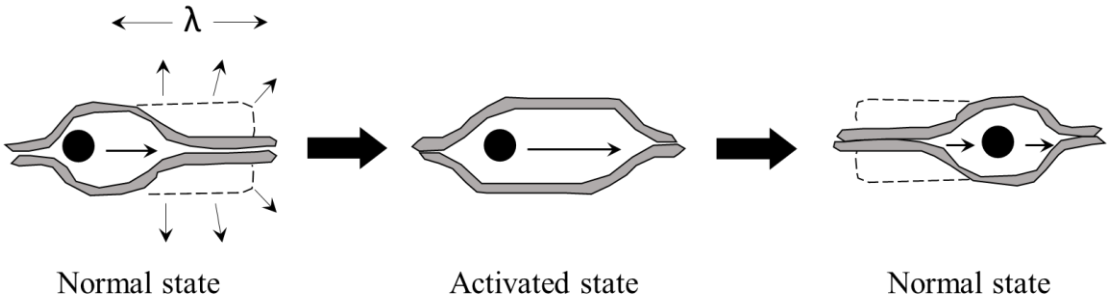

Figure 2.4: Conceptual representation of gas diffusion in polymeric membranes. Reproduced from [69].

Gas diffusion in CMS membranes is different due to the rigid pore structure.[72, 73, 76] It takes place via activated diffusion jumps from one micropore sorption site to another through the restrictive ultramicropores. Gaseous penetrants must overcome the repulsive energy from the restrictive and rigid ultramicropores to complete a diffusion jump from one micropore sorption site to another. Gas molecules present in the micropore sorption sites are in the normal state of a diffusion jump, while those going through the ultramicropores are in the activated state. Figure 2.5 shows diffusion of gas molecules through CMS membranes. Unlike in polymeric membranes, both penetrant size and shape are important factors affecting activated diffusion in CMS membranes. The rigid ultramicropores in CMS membranes can efficiently differentiate between gaseous penetrants based on size and shape, leading to high diffusion selectivity.

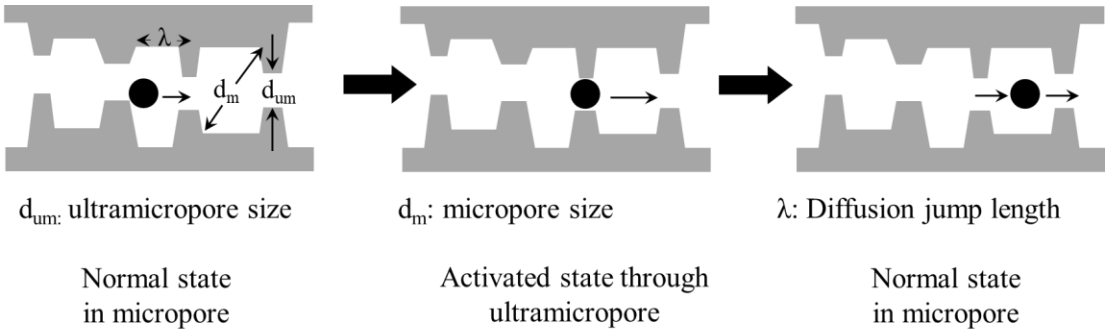

Figure 2.5: Conceptual representation of gas diffusion in CMS membranes. Reproduced from [69].

2.2.4 Temperature dependence of permeation, sorption, and diffusion

Both permeation and diffusion are activated processes; their temperature dependence can be described using an Arrhenius relationship.[68, 71, 77]

$$P_A = P_{A0} \exp\left(-\frac{E_{PA}}{RT}\right) \tag{2.11}$$

$$D_A = D_{A0} \exp\left(-\frac{E_{DA}}{RT}\right) \tag{2.12}$$

Gas sorption in membranes on the other hand, can be described using a van't Hoff expression.

$$S_A = S_{A0} \exp\left(-\frac{\Delta \mathrm{H_{SA}}}{RT}\right) \tag{2.13}$$

where, P_{A0} (cm^3(STP).cm/cm^2.s.cmHg), D_{A0} (cm^2/s) and S_{A0} (cm^3(STP)/cm^3.cmHg) are pre-exponential factors, E_{PA} (J/mol) is the permeation activation energy, E_{DA} (J/mol) is the diffusion activation energy, ΔH_{SA} (J/mol) is the heat of sorption, R (J/mol.K) is the universal gas constant and T (K) is the absolute temperature.

Combining equations 2.11-2.13 with 2.7 shows that the permeation activation energy is a sum of diffusion activation energy and heat of sorption. [68, 77, 78]

$$E_{PA} = E_{DA} + \Delta H_{SA} \tag{2.14}$$

Additionally, the pre-exponential factors are arranged to give,

$$P_{A0} = D_{A0} \cdot S_{A0} \tag{2.15}$$

Since the heat of sorption is usually negative, permeation activation energy is generally lower than diffusion activation energy, meaning that temperature dependence of permeation is less pronounced compared to temperature dependence of diffusion. However, the decrease in sorption coefficient is generally dominated by the increase in diffusivity, leading to an overall increase in permeability with temperature.

2.3 Structure of carbon molecular sieve (CMS) membranes

Carbon molecular sieve (CMS) membranes are derived from polymeric precursors via high temperature pyrolysis beyond their thermal decomposition temperature. Pyrolysis of any carbonaceous precursor yields coke or char.[79] Precursors that go through a liquid phase during pyrolysis before decomposition yield graphitizable carbon or coke. On the other hand, precursors that do not pass through a liquid phase prior to decomposition during pyrolysis yield non-graphitizable carbon or char.[79, 80]

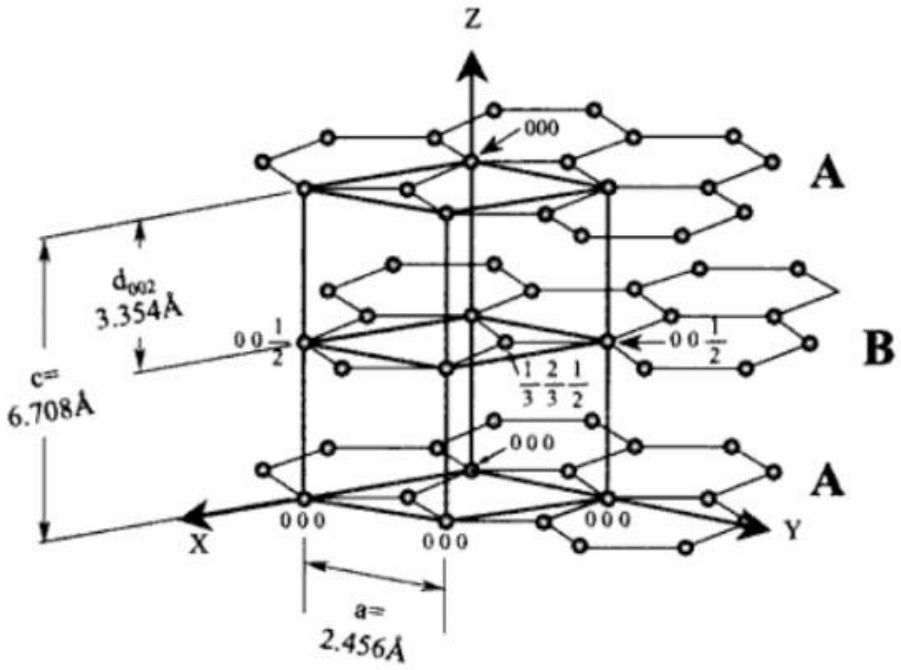

Figure 2.6: Crystal structure of graphite with ABAB stacking.[79]

Figure 2.6 shows the crystal structure of hexagonal graphite, with carbon atoms arranged in layers or lamellae parallel to each other in an AB-AB type stacking sequence.[79, 80] Any carbon form can be a derivative of a graphitic structure although

with incorporation of defects.[80] Coke is an anisotropic carbonaceous material with parallel arrangement of graphitic lamellae with the capability of assuming long-range order on heat treatment. Char is an isotropic carbonaceous material with randomly bent, twisted, and imperfectly arranged lamellae which remains in the amorphous form. The imperfect arrangement of graphitic lamellae could be due to inclusion of bonded heteroatoms like hydrogen, oxygen, nitrogen, etc. as well as holes due to deviation from true lattice configurations. These imperfections contribute to the material porosity.[81]

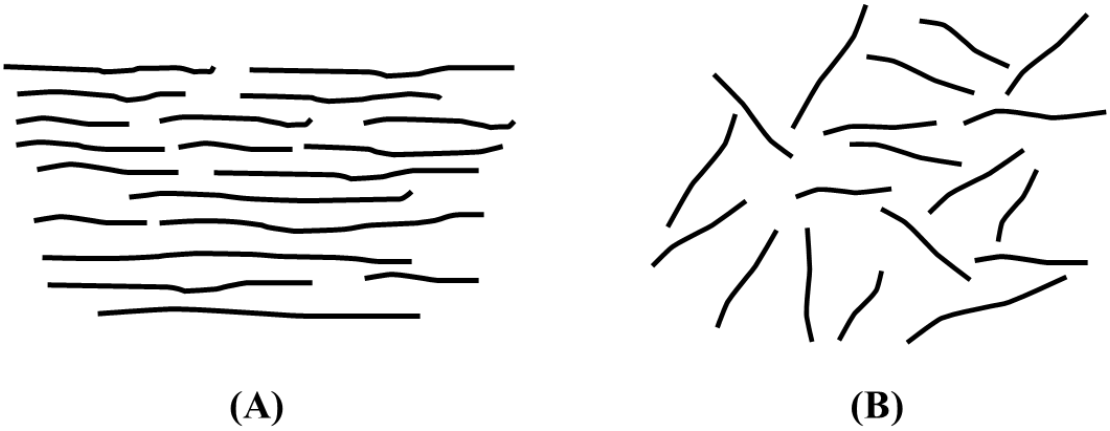

Figure 2.7: Schematic representation of lamellar arrangements in (A) anisotropic carbon and (B) isotropic carbon.

Figure 2.7 shows schematic cartoons of graphitic lamellar arrangements in anisotropic and isotropic carbonaceous materials.[81] CMS membranes made by controlled pyrolysis of polymeric precursors, form a turbostratic ribbon-like structure with very small extent of long-range order, essentially considered isotropic carbon.[79, 81] Polymers that yield both coke and char can be considered as CMS membrane precursors as both have very little long-range order in the early stages of

decomposition. However, polymers that form char are often considered as the practical starting precursors due to the isotropic, amorphous non-graphitizable properties of char. The pores in CMS membranes are formed due to imperfectly packed and highly disordered sp^2-hybridized graphite-like sheets. Molecular-sieving carbons, unlike other rigid molecular sieving materials such as zeolites, possess an amorphous structure with a wide pore size distribution. An idealized CMS pore structure can be characterized as slit-like with a bimodal pore size distribution consisting of larger micropore chambers (7-20Å) connected by smaller ultramicropore windows (< 7Å). The idealized CMS pore structure is shown in Figure 2.8. This unique combination of ultramicropores and micropores enables CMS membranes to simultaneously high permeability and selectivity for gas separations.[73, 82]

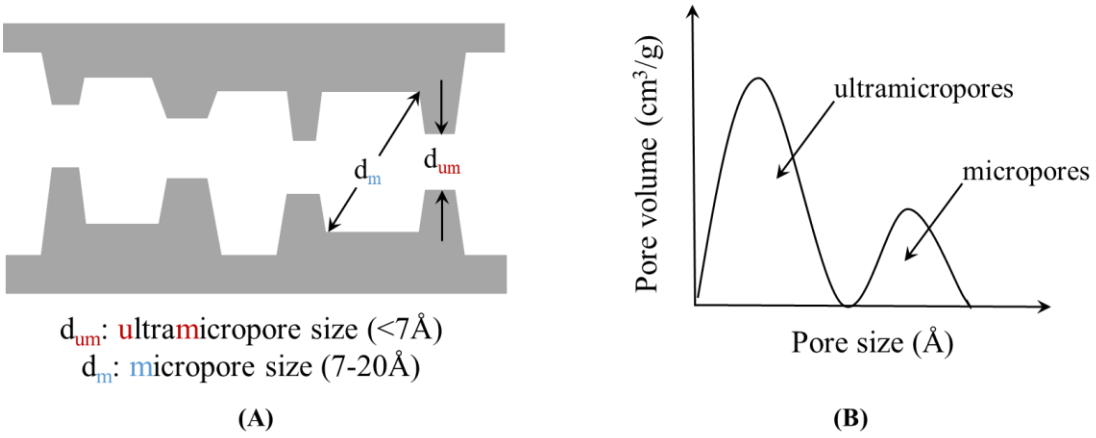

Figure 2.8: (A) Idealized CMS pore structure (B) Typical bimodal pore size distribution in CMS membranes.

2.4 Formation of CMS membranes

2.4.1 Structural evolution during pyrolysis

As discussed earlier, CMS membranes are formed by controlled pyrolysis of polymeric precursors above their thermal decomposition temperature. In general, the pyrolysis protocol constitutes a "ramp" phase from room temperature to the final pyrolysis temperature, followed by a thermal "soak" phase at the final pyrolysis temperature and subsequently a "cool" phase from the final pyrolysis temperature back to room temperature.[83]

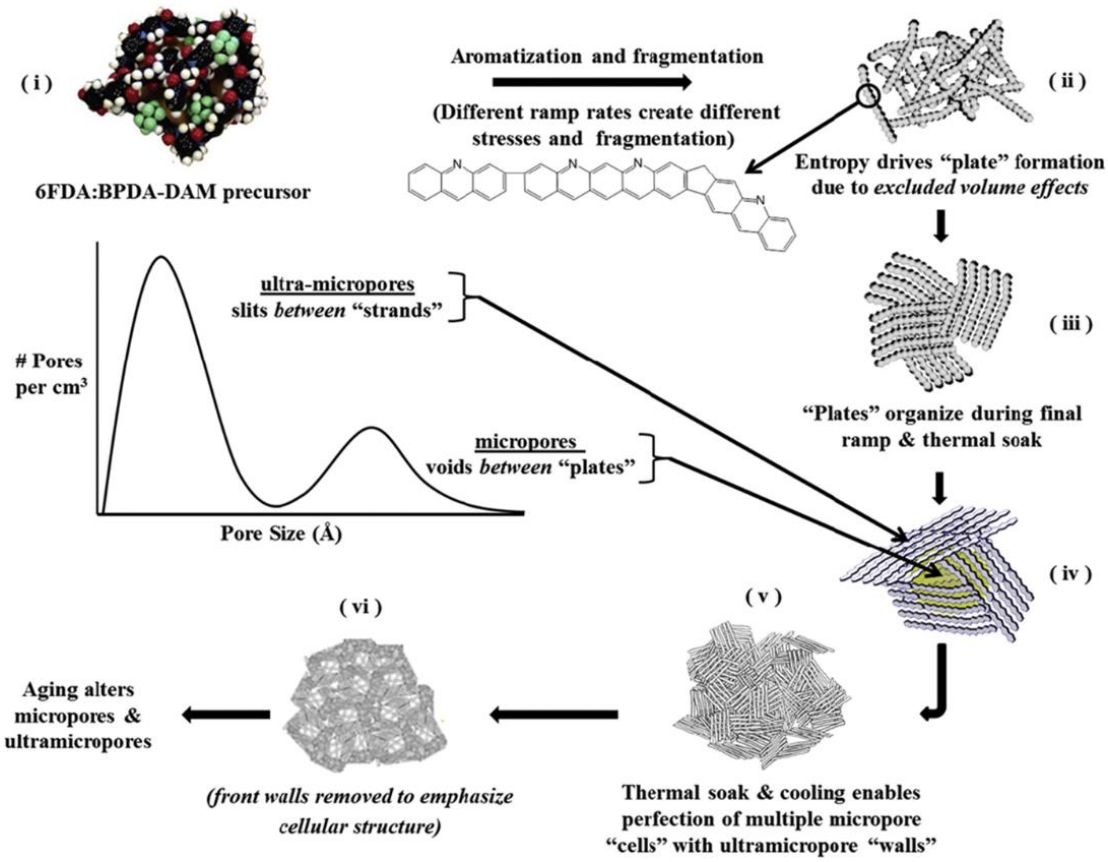

Figure 2.9: Envisioned structural evolution of CMS during pyrolysis.[83]

During the pyrolysis process, the random polymer coils undergo several structural changes to form a rigid carbonized CMS pore structure. The evolution of the structural changes during the pyrolysis process was envisioned by Rungta et al., in 2017 for CMS membranes derived from 6FDA:BPDA-DAM precursor and is illustrated in Figure 2.9.[83] The carbonization process involves complex chemical reactions including cleavage, dehydrogenation, condensation, isomerization, etc. with elimination of small molecules and subsequent rearrangement of carbon atoms into stable six-membered rings forming disordered carbon lamellae.[84, 85] During the "ramp" phase, polymeric chains undergo fragmentation and aromatization to form rigid highly aromatic carbon strands.[83] The fragmentation of the polymeric chains takes place during the early stages of pyrolysis involving polymer backbone scissions and subsequent formation of free radicals. Carbonization occurs by elimination of small volatile components such as water, methanol, methane, carbon dioxide etc., during the "ramp" phase. The hypothetical reaction pathways during pyrolysis have been visualized for PIM-1[86] and crosslinked polyaramid[64] precursors previously in literature and are shown in Figure 2.10. As the final pyrolysis temperature is reached, almost all the aliphatic carbon is converted to aromatic carbon in the amorphous carbon lamellae, forming rigid aromatized carbon strands.[81] These randomly oriented aromatized carbon strands align and organize into plates. This is an entropy-driven phenomenon as the plates are in an overall higher entropy state. During the "soak" phase, the plates are imperfectly packed due to kinetic restrictions hindering perfect organization. An idealized micropore "cell" is formed, consisting of imperfectly packed plates with each plate comprising imperfectly packed strands. The spacing

between adjacent strands form the ultramicropores while the large space enclosed by the imperfectly packed plates forms the micropore. Through the thermal "soak" and "cool" phase, adjacent micropore cells coalesce by sharing ultramicroporous "walls" and the resulting idealized amorphous CMS pore structure with micropores separated by ultramicropores in the micropore plate walls is formed.[83]

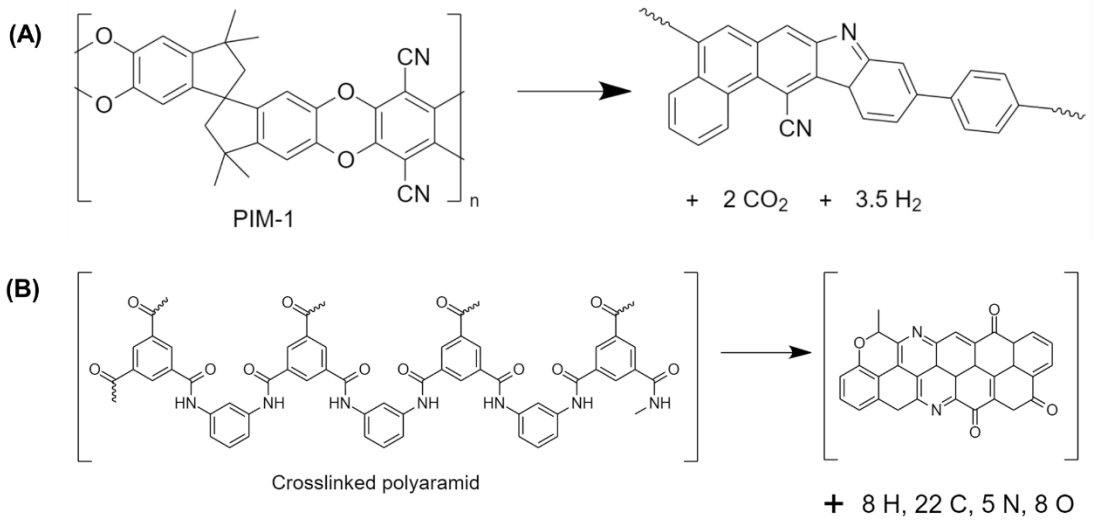

Figure 2.10: Hypothetical reaction pathways during pyrolysis of (A) PIM-1, (B) Crosslinked polyaramid. Note that many pyrolytic reactions can be envisioned.

Sanyal et al. in 2020 demonstrated dual-mode sorption behavior in CMS membranes and provided innovative insights on the CMS structural evolution during pyrolysis to explain the dual-mode sorption behavior.[74] In addition to the idealized micropore cells forming the microporous "Langmuir domains" in the CMS membranes, the presence of another domain was proposed. This domain was predominantly a continuous network of disordered aromatized orphan strands between and around the Langmuir domains, called the "continuous domain". This continuous

domain was responsible for Henry's sorption contribution to the dual-mode sorption behavior.

Physical aging phenomenon is observed in CMS membranes post-synthesis, wherein the imperfectly packed plates undergo partial densification to achieve thermodynamically more stable states. Physical aging is known to cause minor diffusion selectivity changes with significant reduction in sorption and diffusion selectivity in CMS membranes.[87] Hays et al. in 2020 discovered "slit bypass pores" as the major contributor to physical aging in CMS membranes.[88] Slit bypass pores are caused due to edge imperfections between neighboring ultramicroporous plates formed during the kinetically hindered imperfect packing of the plates during the "soak" phase. Their study also highlighted that physical aging in CMS membranes can be controlled under CO_2 storage conditions due to continuous self-diffusion circulation of CO_2 molecules through the slit bypass pores which hinders pore tightening during the aging phenomenon.

2.4.2 CMS membrane configuration

CMS membranes, like polymeric membranes, can be made in both supported and unsupported configurations.[89] Supported CMS membranes can be fabricated from polymeric precursor membranes cast over flat-sheet porous substrates or tubular porous inorganic substrates. Unsupported CMS membranes or free-standing CMS membranes can be made as a flat-sheet film or hollow fiber (dense homogeneous or asymmetric). While supported membranes are usually used for lab-scale studies, the inorganic tubular supports are quite cost intensive for industrial scale membrane fabrication. Hollow fiber membranes are the preferred configuration due to their high

membrane surface area-to-volume ratio. Free-standing dense films are considered the most suitable for material characterization studies. Hollow fiber membranes were of particular focus in this research due to their excellent scalability and industrial viability.

2.4.3 Polymer precursor

The chemistry of the polymer precursor is known to govern the gas transport properties of the CMS membranes. Several classes of polymers have been studied as CMS membrane precursors including polyimides[42, 45, 49, 90-93], polybenzimidazoles[10, 52], polymers of intrinsic microporosity[50, 94, 95], polyvinylidene fluoride/chloride[96, 97], cellulose-based polymers[41, 98], etc. High glass transition temperature, high carbon residual weight, ease of processability, strong mechanical properties and attractive separation performance are among the desired characteristics for a polymer to qualify as a CMS membrane precursor.

Studying the correlation between polymer precursor chemistry and CMS membrane pore structure and transport properties has been an attractive area for membrane researchers. Several studies highlight this relationship by pyrolyzing different polymeric precursors under identical pyrolysis conditions and performing a comparison study of the pore structure and separation performance of the different CMS membranes.[47, 73, 99] Glass transition temperature, Fractional free volume (FFV), polymer backbone structure, symmetry, and mobility, can all affect the gas separation properties of the CMS membranes. Higher FFV polymer precursors with bulkier side groups produce CMS membranes with higher permeability and lower selectivity for a series of gas pairs. High polymer backbone rigidity and aromaticity in the polymeric precursor is known to provide more mechanically robust CMS

membranes.[47] Polymer precursors with higher glass transition temperature have been reported to have greater resistance to substrate densification during asymmetric CMS hollow fiber membrane fabrication, resulting in higher permeance. [69]

Hence, choosing an adequate polymer precursor as a starting material is critical to successfully fabricate CMS membranes for specific gas separation applications. In this research, the role of precursor chemistry and interchain interactions in achieving attractive H_2/CO_2 separation properties is specifically highlighted in Chapter 6.

2.4.4 Pyrolysis conditions

Polymer precursors are heated under controlled pyrolysis conditions beyond their thermal decomposition temperature to produce CMS membranes. The pyrolysis heating protocol and conditions are of vital importance in achieving the desired separation performance in the CMS membranes. The controlled parameters include: (1) Pyrolysis temperature; (2) Thermal ramp rate; (3) Thermal soak time; (4) Pyrolysis atmosphere.

Gas separation performance of CMS membranes is strongly affected by the final pyrolysis temperature. An increase in pyrolysis temperature leads to compaction of the CMS pore structure, giving refined ultramicropores which predominantly improves size selection thereby increasing diffusion selectivity. Therefore, with an increase in pyrolysis temperature, lower gas permeability and higher selectivity is expected.[44, 48, 100-102] Zhang et al in 2017 reported a synergistic increase in diffusion and sorption selectivity in CMS membranes produced at higher pyrolysis temperatures.[43] Refined ultramicropores at higher pyrolysis temperatures increased the diffusion selectivity in several gas pairs, while improving the exclusion of larger

penetrants from the CMS micropores, leading to a synergistically increased sorption selectivity. The optimum pyrolysis temperature depends on the polymer precursor and the target separation application. In general, gas pairs with similar sized molecules demand higher pyrolysis temperatures while gas pairs with largely different molecular sizes prefer lower pyrolysis temperatures. Figure 2.11 shows a schematic representation of the effect of pyrolysis temperature on the CMS pore structure.

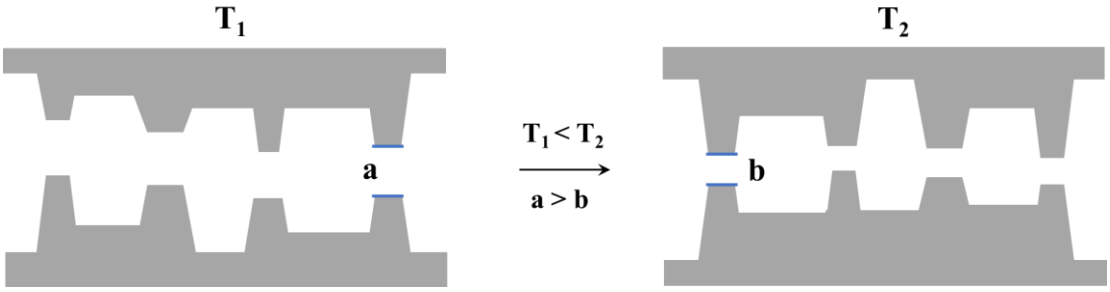

Figure 2.11: Schematic depiction of effect of pyrolysis temperature on CMS pore structure.

Thermal ramp rate can influence the total pyrolysis time and the rate of evolution of volatile molecules during the carbonization process. A smaller ramp rate implies a slower evolution of volatiles and longer pyrolysis time which allows for a greater extent of pore sintering, leading to smaller average pore size and lower permeability.[78, 103] Thermal soak time also affects the CMS pore structure by causing a pore sintering effect. Longer soak time favors pore sintering leading to narrower average pore size, which decreases permeability.[73, 104]

Pyrolysis atmosphere is controlled by maintaining an inert gas purged environment or vacuum inside the pyrolysis chamber. Vacuum or inert gas purging enables prevention of undesired loss of polymeric precursor by oxidation. Previous

reports have indicated that vacuum pyrolysis gives more selective and less permeable CMS membranes[82, 105]; however, vacuum pyrolysis lacks reproducibility in the CMS membrane fabrication process. Hence, inert gas purging is preferred for practical application. Previous studies have investigated the effect of inert gas flow rate on CMS gas separation properties, revealing an increase in permeability with a negligible change in selectivity using higher flow rates.[105] A higher purge gas flow rate enhances convective mass transport of volatile by-products during pyrolysis resulting in a more open CMS pore structure with higher permeability.[105] Oxygen doping is also studied to tune the molecular sieving properties of CMS membranes.[47, 106-109] Carbonization at elevated temperatures causes trace amount of oxygen in the purge gas to selectively chemisorb on the edges of the carbon lamellae which form the ultramicropores. Oxygen doping has reportedly been used to improve selectivity and largely maintain permeability, hence fine tuning the molecular sieving sites of the CMS ultramicropores. Figure 2.12 provides a schematic representation of the effect of oxygen doping on the CMS pore structure.

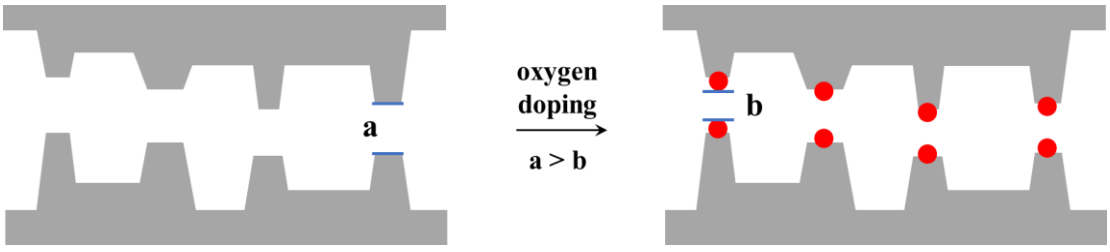

Figure 2.12: Schematic depiction of effect of oxygen doping on CMS pore structure.

In this research, the influence of pyrolysis temperature will be discussed in Chapter 4.

2.5 Formation of asymmetric polymer hollow fiber membranes

Hollow fiber membrane geometry is used as the final membrane format in this research owing to its high membrane surface area-to-volume ratio which enables smaller membrane footprint. The formation of polymer precursor hollow fiber membranes was the first step, pyrolysis of which produces CMS hollow fiber membranes in the final step.

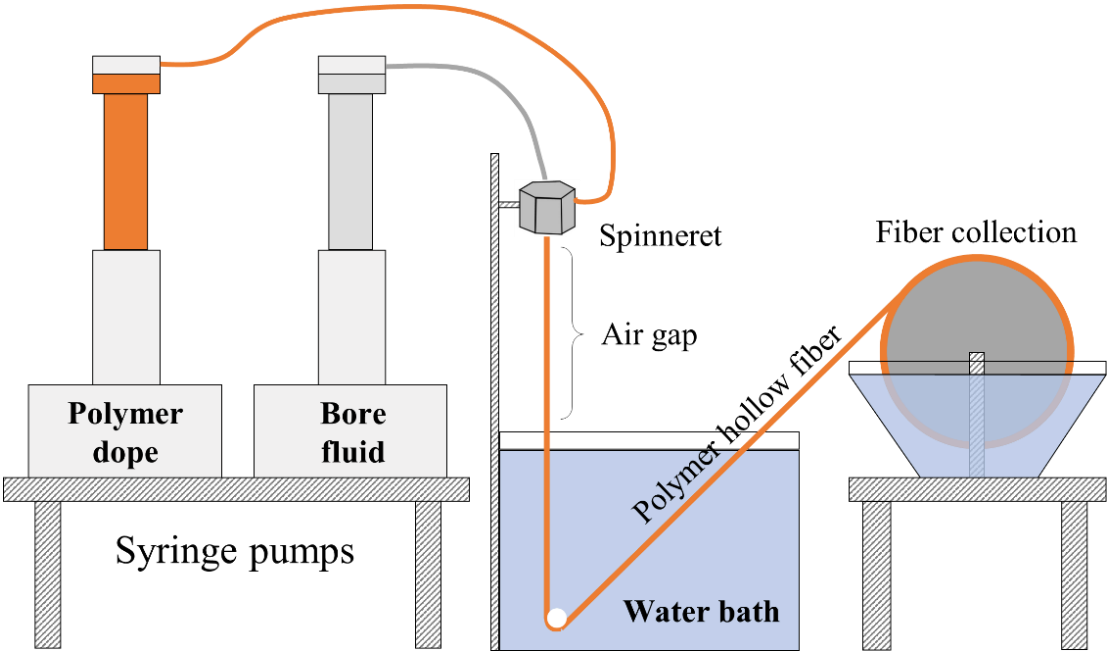

Figure 2.13: Schematic diagram of the custom-built hollow fiber spinning system.

Table 2.1: Key parameters in dry-jet/wet-quench spinning process.[69]

Dope composition	Air gap	Quench bath temperature
Bore fluid composition	Take-up rate	Quench bath composition
Dope/bore fluid flow rate	Spinning temperature	Humidity

Polymer solutions used to fabricate hollow fiber membranes are referred to as "dopes". A dope typically consists of polymers, solvents, non-solvents, and additives.

Asymmetric polymer hollow fiber membranes constitute a dense skin layer over a porous substructure, which are produced through a dry-jet/wet-quench spinning process.[69] The schematic of the dry-jet/wet-quench spinning apparatus is shown in Figure 2.13. The important spinning parameters are listed in Table 2.1. The spinning process involves coextrusion of the spinning dope and bore fluid through a spinneret in an air gap (dry-jet) which is then immersed into a water quench bath (wet-quench). The "dry-jet" forms the dense skin layer while the "wet-quench" produces the porous substructure.[69]

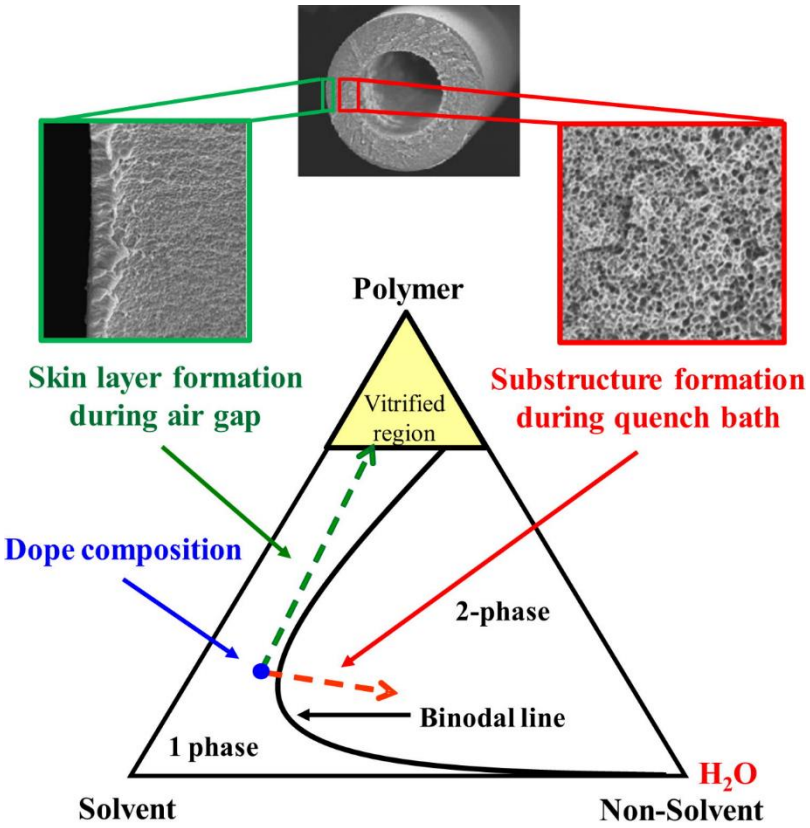

Figure 2.14: Ternary phase diagram indicating formation of asymmetric hollow fiber membrane during dry-jet/wet-quench spinning process.[69]

The qualitative trajectories of dope composition during the spinning process are shown in Figure 2.14. A good dope composition is one which lies close to the binodal curve but in the single-phase region for rapid phase separation. The concentration of the polymers, solvents, non-solvents, and additives are optimized to achieve this optimum dope composition.[110-112] In the air gap, the dry-jet undergoes evaporation of volatile components and its composition is driven to the vitrified region leading to formation of a dense layer on the outer surface of the fiber. In the quench bath, the wet-quench exchanges solvent with the excess non-solvent in the bath and phase separation is induced. Precipitation of the polymer solution in the quench bath causes the fiber to gain mechanical strength and the porous substructure of the fiber is formed during the phase separation step. The hollow fiber configuration is formed due to coextrusion of the dope with a bore fluid. The bore fluid is a neutral fluid which occupies the space that forms the hollow lumen of the fiber. This bore fluid can be further removed during solvent exchange and drying steps.[69]

Chapter 3: Materials and Experimental methods

3.1 Overview

This chapter describes the various materials and experimental procedures used in this research. Section 3.2 provides details on the different materials used to carry out the experimentation, categorized as polymers, gases, and other chemicals. Information regarding the commercial polymers used in this work is also given in this section. Section 3.3-3.8 explains the detailed experimental procedures including polymer synthesis, membrane fabrication and membrane characterization.

3.2 Materials

Materials used in this research can be broadly classified into three categories – polymers, gases, and other chemicals.

3.2.1 Polymers

In this research, polyaramid (PA) was chosen as the polymer of focus to be used as a precursor to develop carbon molecular sieve membrane for gas separation. The polyaramid used was an in-house polymer MPD-TPC/IPC (MTI), synthesized using the procedure described in section 3.3. Two more polymers have been used in this research, which are commercially available polymers under the tradenames Matrimid® - a polyimide (PI), and Torlon® - a polyamide-imide (PAI). Matrimid® 5218 polyimide was provided by Huntsman Corporation (Salt Lake City, UT). Torlon® 4000T-LV polyamide-imide was provided by Solvay Materials (Alpharetta, GA). The polymer structures are indicated in Figure 3.1.

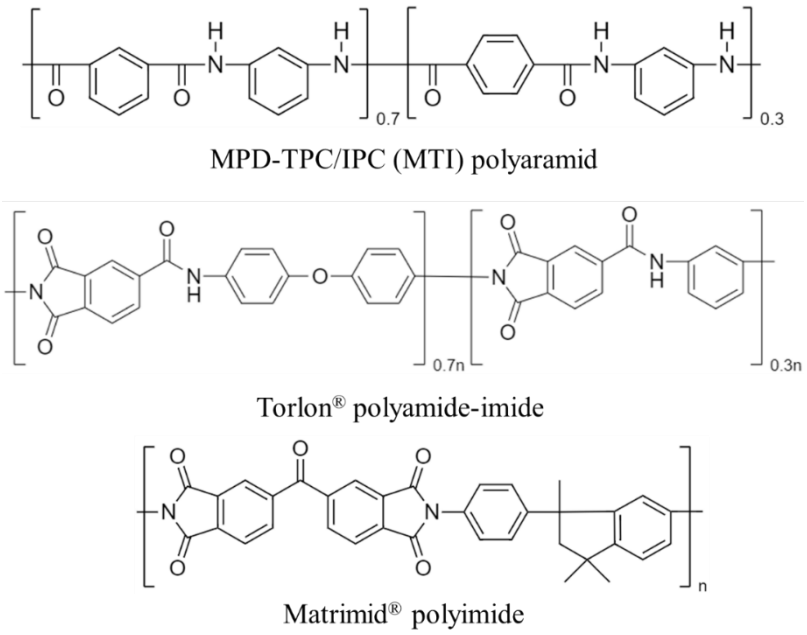

Figure 3.1: Chemical structures of polymers used in this research.

3.2.2 Gases

H_2 and CO_2 (UHP Grade, Airgas) were used for single-gas permeation and sorption experiments to evaluate the intrinsic H_2/CO_2 separation performance of the polymer precursor and CMS membranes. In addition, a binary mixture of 50 mol % H_2 and 50 mol% CO_2 (certified mixture, Airgas) was used for mixed-gas permeation experiments and a binary mixture of 10 mol% H_2 and 90 mol% CO_2 (certified mixture, Airgas) was used for high temperature mixed-gas permeation experiments in the CMS membranes. Other gases used for polymer precursor membrane and CMS membrane characterization include He (UHP Grade, Airgas), N_2 (UHP Grade, Airgas), and CH_4 (UHP Grade, Airgas). Ar (UHP Grade, Airgas) was used for inert gas purging during pyrolysis.

3.2.3 Other chemicals

1,3-phenylenediamine (MPD, 99%), sodium carbonate (≥99.5%, anhydrous), tetrahydrofuran (THF, ≥99.0%, anhydrous with 250 ppm BHT as inhibitor), chloroform (≥99%, anhydrous), dichloromethane (≥99.8%, anhydrous), 1,2-dichloroethane (≥99.8%, anhydrous), ethanol (≥99.5%, anhydrous), benzene (≥99.9%), isopropyl alcohol (≥99.5%), and 1-methyl-2-pyrrolidone (NMP, anhydrous, 99.5%) were obtained from Sigma Aldrich (St. Louis, MO). Hexane (≥98.5%, mixture of isomers), N-methylpyrrolidone (NMP, ≥99.0%), and methanol (≥99.8%) were obtained from VWR (Radnor, PA). Isophthaloyl chloride (IPC, ≥99.0%), terephthaloyl chloride (TPC, ≥99.0%), Isopar™ G, dimethyl sulfoxide (DMSO, ≥99.8%), dimethylformamide (DMSO, ≥99.8%), and N,N-dimethylacetamide (DMAc, ≥99.8%, anhydrous) were purchased from Fisher Scientific™ (Pittsburgh, PA). All chemicals were used without further purification.

3.3 Polymer synthesis

The MTI polyaramid was an in-house polymer used in this research as a CMS membrane precursor. The polyaramid powder is synthesized by stirred interfacial polymerization.[56, 113] MPD dissolved in the aqueous phase reacts with a mixture of IPC and TPC dissolved in the organic phase at the interface of the two immiscible phases being continuously replenished by vigorous stirring. For the synthesis, an aqueous phase solution of 4.326 g (0.04 mol) MPD and 8.48 g (0.08 mol) sodium carbonate (acid acceptor) dissolved in 120 mL de-ionized (DI) water was prepared in a glass jar. While the aqueous phase solution in the glass jar was stirred at high speed

(2000 rpm) using an overhead mechanical stirring setup, an organic phase solution of 5.68 g (28 mmol) IPC and 2.44 g (12 mmol) TPC dissolved in 150 mL THF was rapidly poured into the aqueous phase and the stirring was continued for 5 minutes. The polyaramid was obtained as a white precipitate suspended in the reaction mixture. After the stirring was stopped, the reaction mixture was quenched in a methanol/water (50/50 wt%) bath (3 L). The polymer was recovered by vacuum filtration followed by washing in copious amount of methanol for 72 hours. After being dried in a fume hood for 12 hours, the polymer was further dried under vacuum at 110 °C for 12 hours. Figure 3.2 shows a schematic of the polymer synthesis process along with pictures of the synthesis setup and the synthesized polyaramid powder.

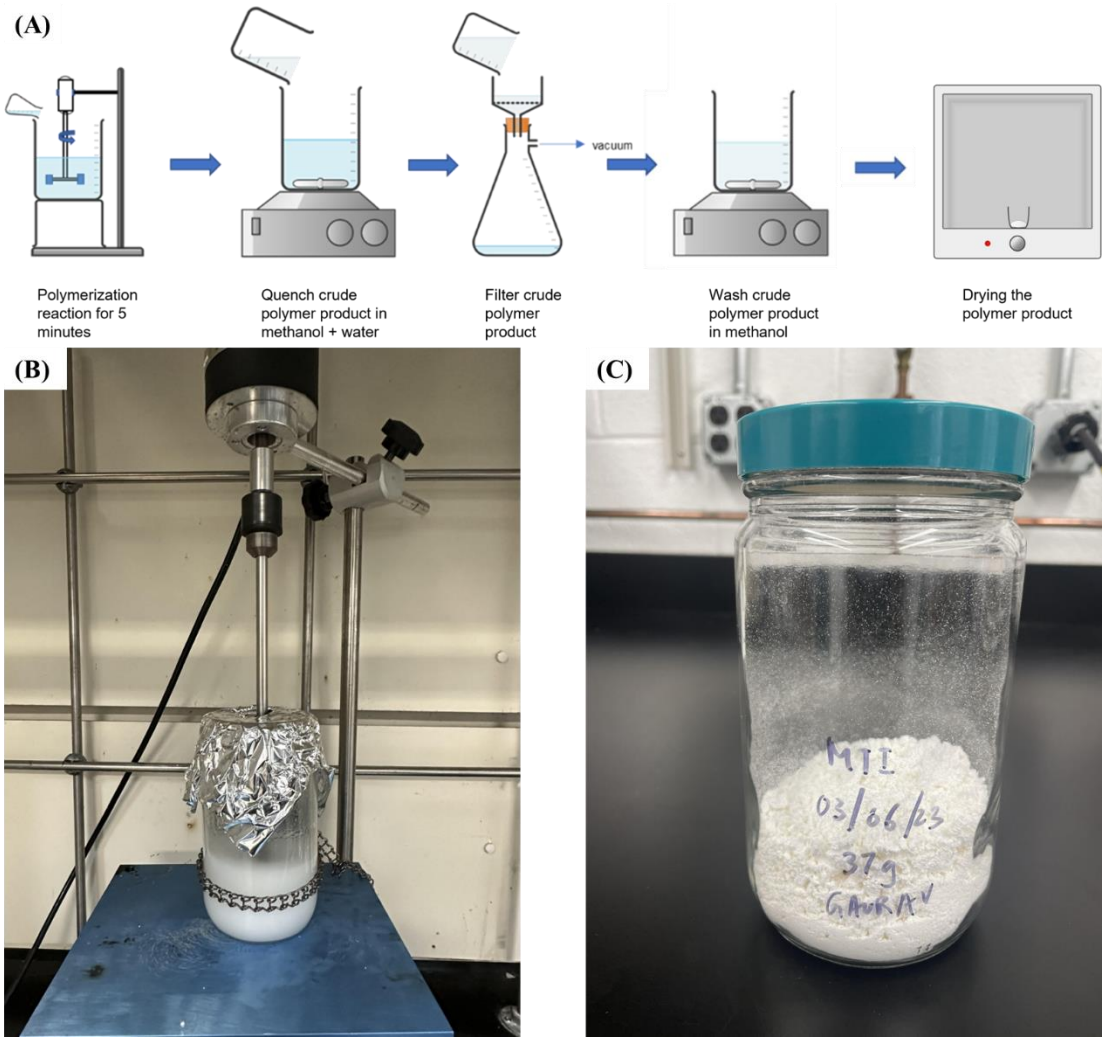

Figure 3.2: (A) Schematic of polymer synthesis process; Photos of (B) Polymer synthesis setup using stirred interfacial polymerization and (C) Final dried MPD-TPC/IPC (MTI) polyaramid powder.

3.4 Formation of polymer precursor membrane

Fabrication of CMS membranes is done in two steps: (1) formation of polymer precursor membranes; (2) pyrolysis of polymer precursor membranes made in step 1. This section describes the procedure for step 1, i.e., fabrication of polymer precursor membranes, while section 3.2 describes the procedure for step 2, i.e., pyrolysis of polymer precursor membranes. In this research, polymer precursor membranes have

been fabricated in the dense film configuration and the hollow fiber configuration. The fabrication procedure for both the configurations is discussed here in detail.

3.4.1 Polymer precursor dense film membrane formation

Dense film membranes are the preferred configuration to study intrinsic properties of novel membrane materials. In this research, polymer precursor dense film membranes were fabricated using a solution-casting technique (Figure 3.3).[114] Dense films were cast using the three polymers mentioned in section 3.2.1.

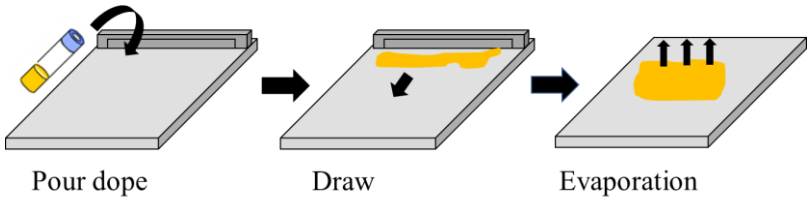

Figure 3.3: Schematic of the generalized dense film casting process by solution-casting technique. Reproduced from [115].

All the polymer powders were vacuum dried at 110°C for 12 hours before preparing dense film casting solutions. Since Matrimid® polyimide could be dissolved in low-boiling organic solvents such as THF, a polymer casting solution was prepared by dissolving 20 wt% of the polyimide in THF. A clean glass plate treated with Siliclad® (Geleste Inc.) was used as a substrate for the film casting. Siliclad® treatment increased the hydrophobicity of the glass casting surface to ease the removal of the vitrified nascent film. The entire casting apparatus was placed inside a polyethylene glove bag (Glass-col LLC, Terre Haute, IN) which was purged with N_2 at least three times and saturated with THF vapor for at least three hours before the film casting. The

THF saturated environment inside the glove bag helped in reducing the solvent evaporation rate enabling formation of smoother films. The homogeneous polymer solution was then spread on the clean Siliclad® treated glass plate using a stainless-steel casting knife with ~ 28 mil clearance. The nascent polymer film was then left for vitrification for 12 hours before removing from the glove bag. The polymer film was then peeled off from the glass plate and annealed under vacuum at 110°C to remove the residual solvent. This film was fabricated by Lu Liu for her Ph.D. research and kindly obtained from her for the experimental work pertaining to this research.[116]

A modified casting procedure[114] was used for MTI polyaramid and Torlon® polyamide-imide as they could not be dissolved in low-boiling organic solvents like THF. Since these polymers were soluble in high-boiling polar aprotic organic solvents such as DMAc and NMP, for the MTI polyaramid, a polymer casting solution was prepared by dissolving 16 wt% of the polyaramid in DMAc while for Torlon® polyamide-imide, a polymer casting solution was prepared by dissolving 24 wt% of the polyamide-imide in DMAc. The polymer solution was spread on a clean borosilicate glass plate using the stainless-steel casting knife with ~ 28 mil clearance. An untreated borosilicate glass plate was used for this casting procedure due to a possible de-wetting effect previously observed for relatively more hydrophilic polymers leading to challenges with uniformly spreading the polymer solution on the hydrophobic Siliclad® treated glass plate. The nascent polymer film on the glass plate was heated in an oven with natural convection for 12 hours for solvent evaporation. The vitrified polymer film was peeled off from the glass plate and soaked in a methanol bath for 12 hours at room temperature to remove any residual solvent. The film was then fastened flat on a clean

aluminum plate, dried in the fume hood for 12 hours followed by the vacuum oven at 210°C for 24 hours. The Torlon® polyamide-imide dense film membrane was fabricated by Ching-En Ku and provided for the purpose of this research.

3.4.2 Polymer precursor hollow fiber membrane formation

In this research, polymer precursor hollow fiber membranes were made from MTI polyaramid, Torlon® polyamide-imide, and Matrimid® polyimide by dry-jet/wet-quench spinning in a custom-built hollow fiber spinning system.[46] All polymer powders were vacuum dried at 110°C for 12 hours prior to dope preparation. The dope was prepared in a Qorpak® glass jar and homogenized for 2-4 weeks on a dope roller. The homogeneous dope was then loaded into a 1000 mL syringe pump (ISCO Inc., Lincoln, NE) and degassed overnight. The bore fluid was loaded into another 500 mL syringe pump. The dope and bore fluid were co-extruded through a spinneret with in-line filters between the syringe pump and spinneret. Thermocouples were used for temperature control in the spinneret, dope lines and syringe pumps. The co-extruded dope and bore fluid enter a water quench bath through an air gap to induce phase separation. The phase-separated polymer fiber line is continuously collected on a rotating take-up drum. The fibers were collected and rinsed in de-ionized water baths for three days, in which the de-ionized water was replaced every 24 hours. The fibers were then solvent exchanged in three separate methanol baths for 20 minutes each followed by three separate hexane baths for 20 minutes each. The solvent exchanged fibers were then dried in the fume hood for 12 hours and vacuum dried at 75°C for 12 hours.

Matrimid® polyimide hollow fibers were prepared by Lu Liu and kindly provided for the purpose of this research.[116] Torlon® polyamide-imide hollow fibers were prepared by Ching-En Ku and kindly provided for the purpose of this research.

3.5 Formation of CMS membrane

This section describes step 2 of the procedure to fabricate CMS membranes, i.e., pyrolysis of the polymer precursor membranes.

3.5.1 Pyrolysis setup

The pyrolysis was conducted in a temperature controlled three-zone tube furnace (MTI Corporation, Richmond, CA). Three separate temperature controllers connected individually to their corresponding thermocouples provided a uniform temperature distribution inside the pyrolysis chamber, i.e., the quartz tube (MTI Corporation, Richmond, CA). The ends of the quartz tube were sealed using silicone O-rings (MTI Corporation, Richmond, CA) between an assembly of stainless-steel flanges (MTI Corporation, Richmond, CA). The furnace was operated under inert gas purging, equipped with a mass flow controller (MTI Corporation, Richmond, CA) for controlling the flow rate of purge gas, and an oxygen analyzer (Rapidox 2100Z, Cambridge Sensotec, Saint Ives, UK) to monitor the oxygen level in the quartz tube throughout the pyrolysis process.[69, 115] A schematic of the pyrolysis setup is shown in Figure 3.5.

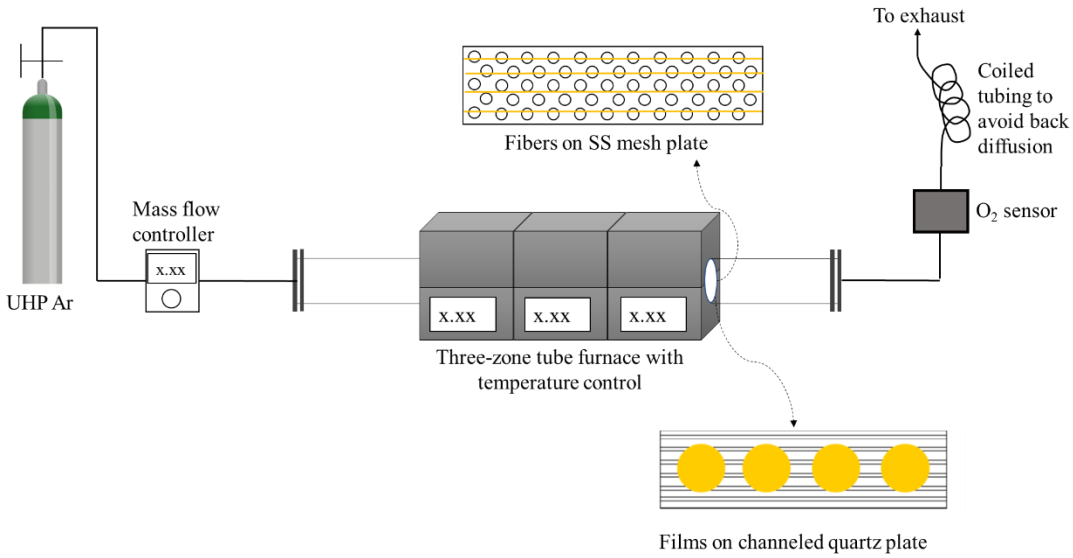

Figure 3.5: Schematic diagram of the pyrolysis setup. Reproduced from [115].

3.5.2 Pyrolysis protocol

The protocol for the dense film pyrolysis and hollow fiber pyrolysis were the same, except for the loading step. The dense films were loaded into the quartz tube on a channeled quartz plate (United Silica Products, Franklin, NJ) while the hollow fibers were loaded on a stainless-steel plate with a wire mesh (McMaster Carr, Robbinsville, NJ) to hold the fibers in place. The quartz tube was under continuous argon purging at 200 cm^3/min. The heating protocol was started after the oxygen concentration in the quartz tube was < 5ppm. The widely reported thermal "ramp and soak" protocol was used for the pyrolysis.[115] The protocol is as follows:

1) Room temperature to 250 °C, 13.3 °C/min
2) 250 °C to T_f - 15, 3.85 °C/min (T_f: Final pyrolysis temperature)
3) T_f - 15 to T_f, 0.25° C/min
4) Dwelling at T_f for 120 minutes

5) Natural cooling down to room temperature

3.6 Gas permeation

Gas permeation measurements were performed using polymer precursor dense film membranes, polymer precursor hollow fiber membranes and CMS hollow fiber membranes. CMS dense film membranes could not be used for permeation measurements because of the challenges associated with curling and crinkling of the films during pyrolysis. Therefore, for the purpose of evaluating intrinsic gas transport properties in the CMS membranes, dense-wall CMS hollow fiber membranes with unambiguously determined wall thickness were used instead of CMS dense films.[43]

For polymer precursor dense film permeation, the film had to be mounted on a permeation cell.[115] The film was first masked by sandwiching between impermeable aluminum tapes, with a known area of the film exposed. The masked film was mounted on the permeation cell over layers of stainless-steel porous filters and Whatman® filter papers providing support to the masked film. The interface between the tape and the film was then sealed by applying Duralco® 4525 (Cotronics Corporation) epoxy. A typical permeation cell assembly is shown in Figure 3.6.

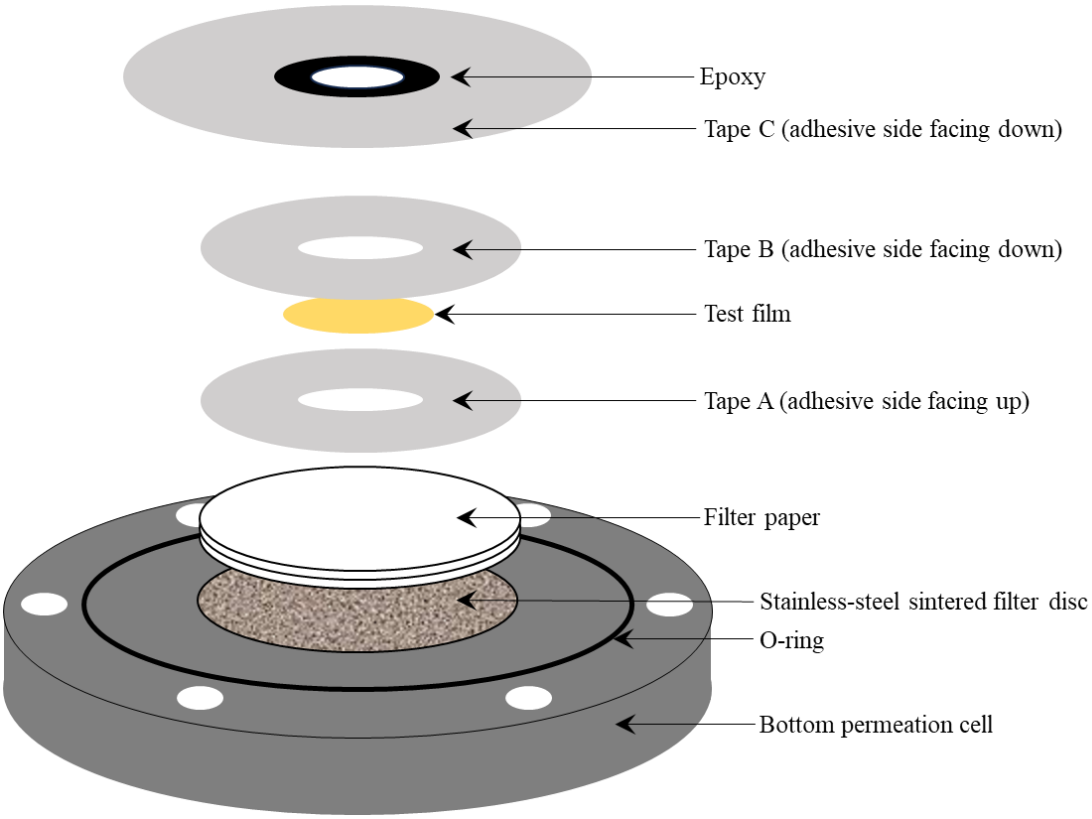

Figure 3.6: Schematic of dense film masking on permeation cell. Reproduced from [115].

For hollow fiber membrane permeation, the fibers were assembled into hollow fiber membrane modules as shown in Figure 3.7.[69] The hollow fiber membrane modules were constructed using Swagelok® tubing and fittings. Epoxy sealing was required to isolate the shell side from the bore side. 3M™ Scotch-Weld™ DP-100 5-minute epoxy was used for permeation measurements under ambient conditions, while Duralco® 4525 epoxy was used for high temperature permeation measurements.[102]

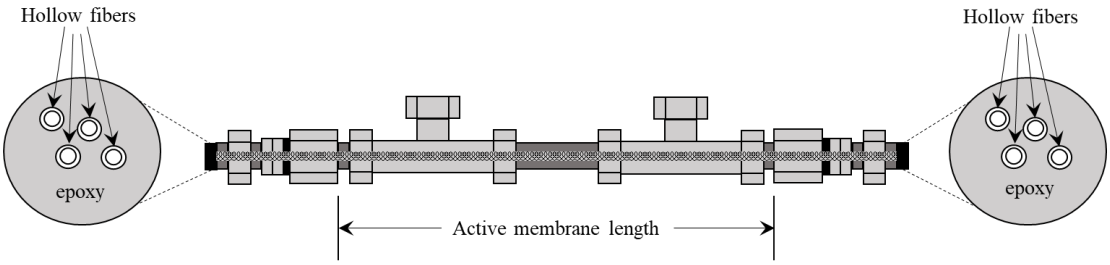

Figure 3.7: Schematic of hollow fiber membrane module. Reproduced from [69].

3.6.1 Single-gas permeation

Single-gas permeation was performed by connecting the permeation cell or the hollow fiber membrane module in a constant volume-variable pressure permeation system.[69] He, H_2, CO_2, N_2 and CH_4 were used as test gases for the single-gas permeation measurements. All tests were performed at 35°C. 1 bar feed was used for dense film membrane permeation while 10 bar feed was used for hollow fiber membrane permeation. Figure 3.8 shows a schematic representation of the custom-built constant volume-variable pressure permeation system in our lab.

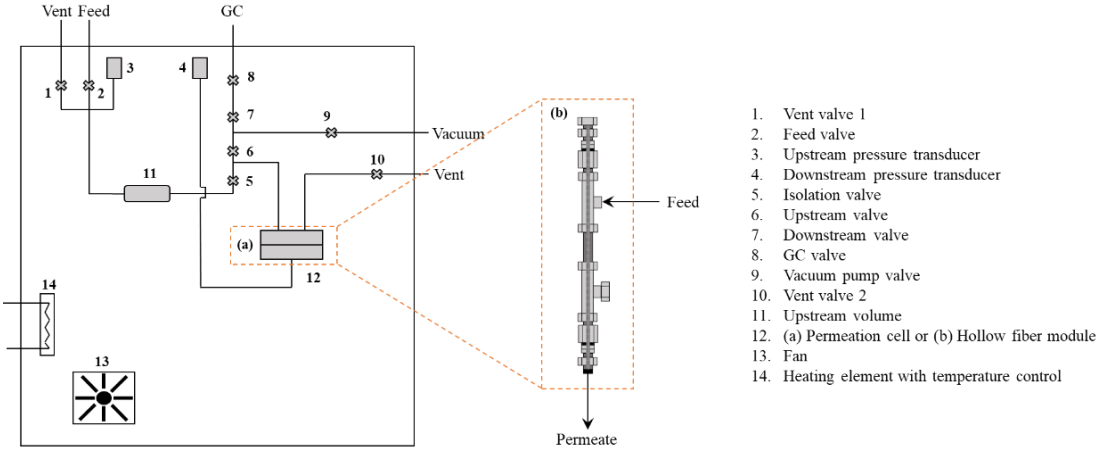

Figure 3.8: Schematic diagram of constant volume permeation system used for gas permeation measurements in (a) dense film membrane and (b) hollow fiber membrane. Reproduced from [115].

Before the permeation flux measurement, the upstream and downstream side were evacuated for a minimum of 12 hours. The outgassing rate in the downstream volume was measured and preferably kept under 1% of the gas permeation rate. The upstream was pressurized on the shell side with the test gas at the desired feed pressure and the rise in downstream pressure versus time was recorded in LabVIEW (National Instruments, Austin, TX) until the permeation reached 10 times the time lag. For switching to a different test gas, the process was repeated from the evacuation stage.

Gas permeability (P, Barrer) and ideal selectivity ($\alpha_{A/B}$) can be calculated as follows.

$$P = \frac{273.15 \times 10^{10} \times Vl}{760 \times AT \left(P_0 \times \frac{76}{14.7}\right)} \left(\frac{dP}{dt}\right) \tag{3.1}$$

$$\alpha_{A/B} = \frac{P_A}{P_B} \tag{3.2}$$

where, dp/dt (torr/s) is the slope of downstream pressure versus time, V (cm^3) is the downstream volume, l (cm) in the membrane thickness, T (K) is the absolute temperature in the permeation system, A (cm^2) is the active membrane area, and Δp (psia) is the upstream pressure. P_A (Barrer) and P_B (Barrer) are the permeabilities of gas A and gas B, respectively.

Diffusivity can be estimated from the permeation time-lag obtained from the permeation plot as shown in Figure 3.9, using Eq. 3.3.

$$D = \frac{l^2}{6\theta} \tag{3.3}$$

where, D (cm^2/s) is the diffusivity and θ (s) is the permeation time-lag.[115]

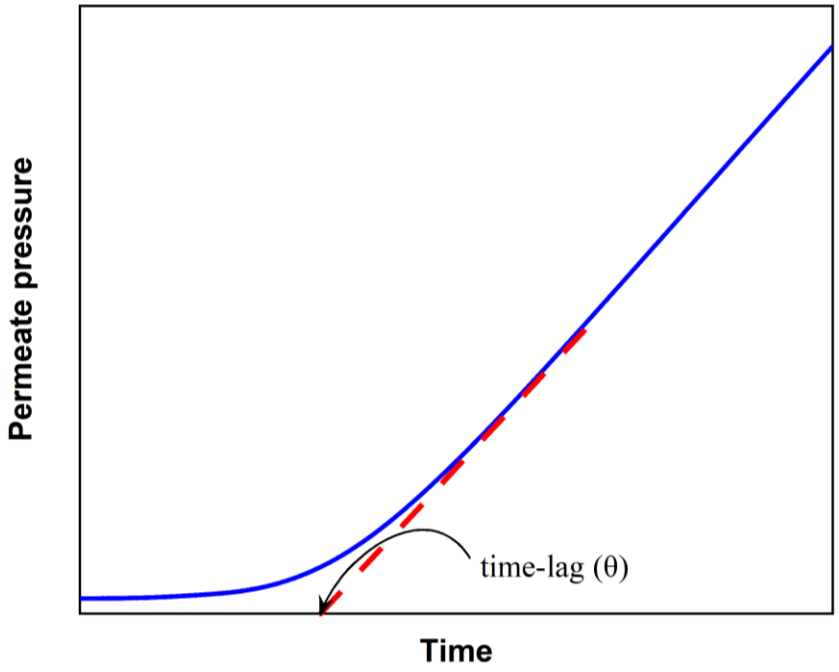

Figure 3.9: Typical permeation plot showing time-lag (θ).

Single-gas permeation in polymer precursor hollow fiber membranes was carried out using a constant pressure permeation system under ambient conditions.[45] A schematic of the constant pressure permeation system is shown in Figure 3.10. The feed gas was pressurized on the shell side of the hollow fiber module and the permeation flow rate was measured using a soap-film bubble flowmeter from the bore side.

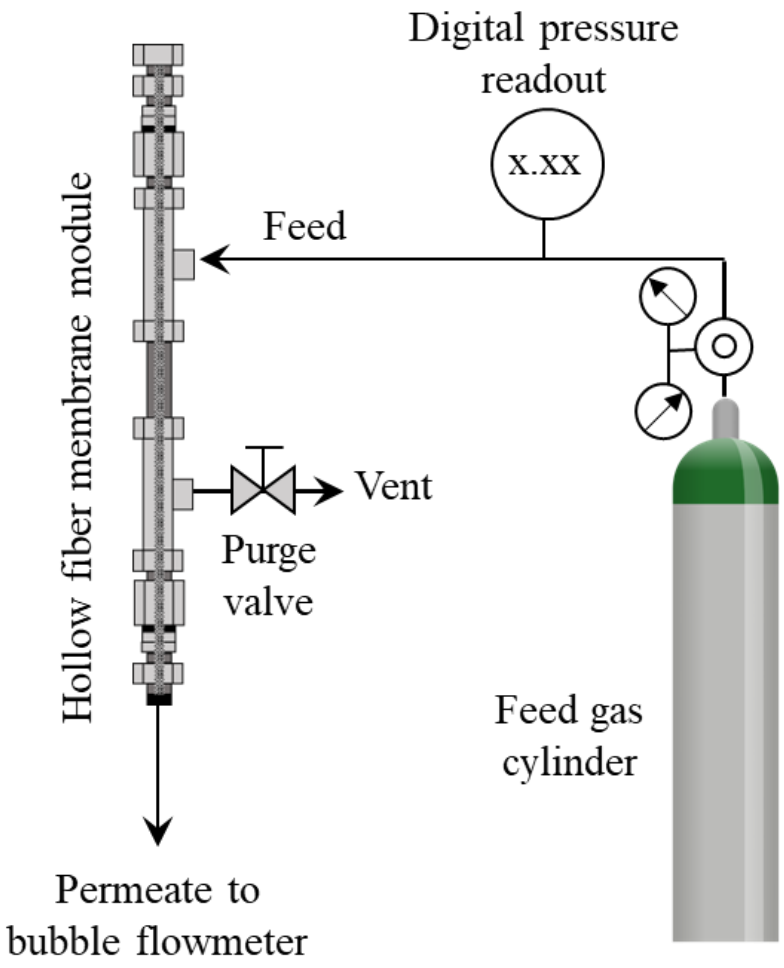

Figure 3.10: Schematic diagram of constant pressure permeation system.

3.6.2 Mixed-gas permeation

Mixed-gas permeation was carried out in the CMS hollow fiber membranes using the constant volume-variable pressure permeation system with an equimolar mixture of H_2 and CO_2 at 2 bar and 35°C as the feed. The stage cut, i.e., the ratio of permeate flow rate to feed flow rate was kept below 1% to avoid concentration polarization. The composition of the permeate stream was measured using an Agilent 8890 gas chromatograph (Agilent Technologies, Santa Clara, CA). Gas

chromatography (GC) injections were taken as the downstream pressure reached 10 torr and continuously taken until a stable permeate composition was achieved. The mixed-gas permeability (*P*, Barrer) and separation factor (*S.F.*) was evaluated as follows.

$$P_A = \frac{273.15 \times 10^{10} \times y_A Vl}{760 \times AT \left(P_0 x_A \times \frac{76}{14.7}\right)} \left(\frac{dP}{dt}\right) \tag{3.4}$$

$$P_B = \frac{273.15 \times 10^{10} \times y_B Vl}{760 \times AT \left(P_0 x_B \times \frac{76}{14.7}\right)} \left(\frac{dP}{dt}\right) \tag{3.5}$$

$$S.F. = \frac{y_A / y_B}{x_A / x_B} \tag{3.6}$$

where, x_A (mol/mol) and x_B (mol/mol) are the mole fractions of components A and B in the feed gas mixture, respectively, while y_A (mol/mol) and y_B (mol/mol) are the mole fractions of components A and B in the permeate stream, respectively.

3.6.3 High-temperature mixed-gas permeation

Mixed-gas permeation in CMS hollow fiber membranes were carried out at elevated temperatures using the constant volume-variable pressure permeation system, using a similar procedure described in section 3.6.2 with certain modifications. A feed mixture containing 10 mol% H_2 and 90 mol% CO_2 was used for these measurements. The active area of the membrane was heated by placing the hollow fiber membrane module outside the permeation system in a temperature controlled single-zone tube

furnace (MTI Corporation, Richmond, CA). A schematic for the high temperature mixed-gas permeation experiment is shown in Figure 3.11.

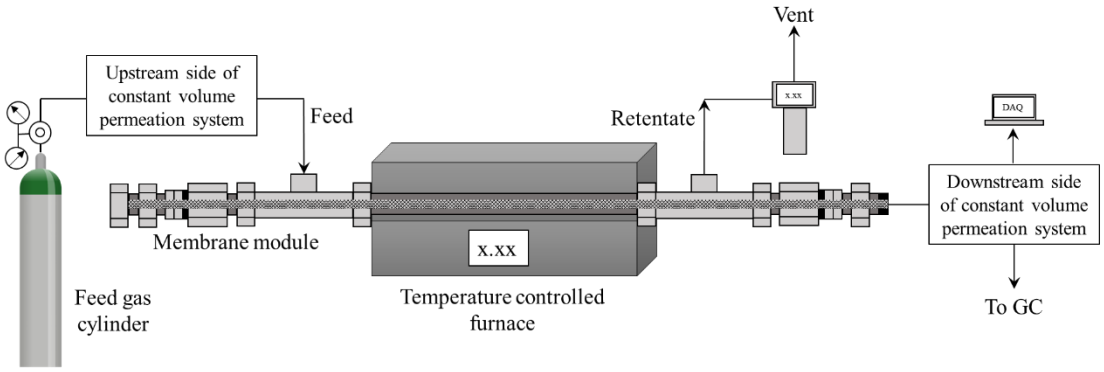

Figure 3.11: Schematic diagram of high temperature permeation system.

3.7 Gas sorption

Sorption isotherms of H_2 and CO_2 were measured at 35°C using an ASAP 2020Plus physisorption analyzer (Micromeritics, Norcross, GA) at pressure up to 1 bar. CMS films were degassed at 120 °C for 12 hours prior to sorption isotherm collection. The H_2 sorption isotherms were fitted using Henry's Law. The CO_2 sorption isotherms were fitted using the dual-mode sorption model.

3.8 Characterization techniques

3.8.1 Inherent viscosity

The inherent viscosity (η_{inh}, dL/g) of the polyaramid powder was measured using a Cannon-Fenske capillary viscometer (Cannon Instrument Company®, State College, PA) using a 5mg/mL solution of polyaramid in NMP. Inherent viscosity is expressed as

$$\eta_{inh} = \frac{\ln(\eta_{rel})}{c} \tag{3.7}$$

where η_{rel} is the relative viscosity defined as the ratio of viscosities of the polymer solution and the solvent, and c (g/dL) is the concentration of the polymer solution used for the measurement.

3.8.2 Thermogravimetric analysis (TGA)

The thermal decomposition temperature and carbon residual weight percentage of the polymer precursors were measured using a Shimadzu TGA50 thermogravimetric analyzer (Shimadzu, Columbia, MD) with a heating rate of 5°C/min up to 950°C under continuous N_2 purge (50 cm^3/min). The sample chamber was continuously purged with N_2 for at least 12 hours before starting the heating protocol.

3.8.3 Differential scanning calorimetry (DSC)

The glass transition temperature (T_g, °C) of the polyaramid was measured using a TA Instruments DSC 2500 differential scanning calorimeter (TA Instruments, New Castle, DE) from -50 to 360°C with a heating and cooling rate of 10 °C/min in N_2 atmosphere. The sample was first heated to 360°C to eliminate effects of thermal history of the materials, followed by a cooling cycle to -50°C and then another heating cycle to 360°C. T_g was taken as the mid-point of the change in heat flux in the heating/cooling cycle.

3.8.4 Fourier Transform Infrared Spectroscopy (FTIR)

Fourier transform infrared spectroscopy (FTIR) for the polymer precursors and the CMS membranes was performed using a ThermoNicolet Nexus 670 FTIR

spectrometer (Thermo Fisher Scientific, Waltham, MA). Polymer powders were used for the measurement. CMS films were crushed into powder form using a pestle and mortar and used for the measurement. The FTIR spectra were collected in the wavenumber range of 4000-650 cm^{-1}.

3.8.5 Density and Fractional free volume (FFV)

Densities of precursor dense films and CMS dense films were measured using an analytical balance, which was equipped with a density kit (OHAUS, Parsippany, NJ) using isopropyl alcohol as the buoyant liquid. Density of isopropyl alcohol was 786 g/cm^3 under ambient conditions.

FFV of a polymer is defined as

$$FFV = \frac{V - V_0}{V} \tag{3.8}$$

where V (cm^3/mol) is the specific volume of the polymer (volume per repeat unit).

$$V = \frac{M}{\rho} \tag{3.9}$$

here, M (g/mol) is the molecular weight of the repeat unit, ρ (g/cm^3) is the measured density of the polymer and V_0 (cm^3/mol) is the occupied volume of the polymer chains. Bondi's group contribution theory is commonly incorporated to obtain an estimate of V_0 using

$$V_0 = 1.3 \sum_{K=1}^{K} (V_w)_K \tag{3.10}$$

where V_w (cm^3/mol) indicates the van der Waals volume for each group in the repeat unit and K indicates the total number of groups in the repeat unit. In this research, the

measured density and the V_w estimated by Park and Paul's method[117], were used to evaluate the FFV.

3.8.6 Scanning Electron Microscopy (SEM)

Scanning electron microscopy (SEM) was performed using a Tescan XEIA3 FEG scanning electron microscope (Tescan, Warrendale, PA). SEM was used to observe the morphology of the polymer precursor and CMS hollow fiber membranes. Polymer precursor fibers were soft in nature; hence sample preparation involved soaking in hexane followed by shear fracturing in liquid nitrogen to preserve the morphology in the cross-section. CMS fibers were comparatively harder and more brittle; hence were directly shear fractured in liquid nitrogen to preserve the cross-section morphology in the SEM samples. The samples were coated with ~3nm AuPd conductive coating before imaging.

3.8.7 Wide angle X-ray diffraction (WAXD)

Wide angle X-ray diffraction (WAXD) patterns for the polymer precursor powders and CMS dense films were recorded using a Bruker D8 Advance Lynx powder diffractometer (LynxEye PSD detector, sealed tube, Cu Kα radiation with Ni β-filter). The Cu Kα radiation had a wavelength of 1.54 Å. The measurement angle (2θ, °) was in the range 5-70°. Bragg's law was used for evaluating the average d-spacing in the samples.

$$\lambda = 2dsin\theta \tag{3.11}$$

where, λ (Å) is the wavelength of incident radiation, θ (°) represents half of the measurement angle, and d (Å) represents the average d-spacing.

3.8.8 Raman spectroscopy

Raman spectra for the CMS dense films were measured using H-J-Y LabRam ARAMIS Confocal Raman Microscope equipped with a 532 nm laser. The 10X objective lens was used for the microscope imaging of the region of interest in the sample. The instrument was calibrated using a Silicon calibration standard before running the samples. The peak fitting of the Raman spectra was carried out in OriginLab software.

3.8.9 X-ray Photoelectron Spectroscopy (XPS)

X-ray photoelectron spectroscopy (XPS) for the CMS dense films was performed using the Kratos AXIS Supra + spectrometer. Determination of elemental composition and peak fitting of the C1s, N1s and O1s spectral scans were done in CasaXPS software.

3.8.10 Porosimetry

Carbon dioxide sorption (0°C) was performed by an ASAP 2020Plus physisorption analyzer (Micromeritics, Norcross, GA). CMS dense films were degassed at 120 °C for 12 hours prior to CO_2 sorption isotherm collection. A density functional theory (DFT) model (CO_2, 0 °C, carbon slit pores) was used to obtain pore size distribution and cumulative pore volume.

Hydrogen sorption (77K) was also performed by an ASAP 2020Plus physisorption analyzer (Micromeritics, Norcross, GA). CMS dense films were degassed at 120 °C for 12 hours prior to H_2 sorption isotherm collection. A non-local

density functional theory (NLDFT) model (HS-2D-NLDFT, carbon, H_2, 77K) was used to obtain pore size distribution and cumulative pore volume.

Chapter 4: Investigating the formation and separation performance of polyaramid-derived CMS membranes

The research described in this chapter is published in: Iyer, G. M.; Zhang, C., Precise Hydrogen Sieving by Carbon Molecular Sieve Membranes Derived from Solution-Processable Aromatic Polyamides. *ACS Materials Letters* **2023,** *5* (1), 243-248.

4.1 Overview

This chapter discusses the formation, characterization, and gas separation performance of polyaramid-derived CMS membranes. In section 4.2, we first discuss the synthesis and characterization of the in-house MPD-TPC/IPC (MTI) polyaramid followed by the intrinsic gas permeation characteristics of the polyaramid precursor membrane. Section 4.3 will present formation of polyaramid precursor hollow fiber membranes and formation of polyaramid-derived CMS hollow fiber membranes. It will also discuss single-gas and mixed-gas transport characteristics in the polyaramid-derived CMS membranes. This section further demonstrates the effect of final pyrolysis temperature on the intrinsic gas permeation properties of the polyaramid-derived CMS membranes. Section 4.4 highlights the contribution of diffusion and sorption to gas transport in polyaramid-derived CMS membranes based on the sorption-diffusion transport mechanism. Finally, section 4.5 explains the gas separation performance of polyaramid-derived CMS membranes using pore structure characterizations.

4.2 Formation of polyaramid precursor membranes and polyaramid-derived CMS membranes

4.2.1 Synthesis of polyaramid precursor

Polyaramids can be inexpensively and rapidly synthesized by in situ interfacial polymerization on a substrate or stirred interfacial polymerization in solution at room temperature.[56, 118] Interfacial polymerization involves a condensation reaction between multifunctional amines dissolved in the aqueous phase and multifunctional acid chlorides dissolved in the organic phase to form a polymer at the interface of the immiscible phases. Vigorous stirring and incorporation of additives during the polymerization reaction are known to improve the polymer yield.[56]

The chemistry of the polyaramid backbone can be tuned using an extensive library of multifunctional amine and acid chloride monomers.[119] Notably, defect-free ultra-thin aramid films made by in situ interfacial polymerization of m-phenylenediamine (MPD) and trimesoyl chloride (TMC) can provide thin-film composite reverse osmosis membranes with attractive water flux and salt rejection.[118, 120] Crosslinked aramids are preferred over uncrosslinked aramid due to their superior monovalent ion rejection; however, they are not solution-processable into films or hollow fibers for CMS membrane formation.[64, 121] Moreover, aramid films formed by in situ interfacial polymerization are known to be asymmetric[122], which prevents unambiguous determination of membrane thickness and intrinsic transport properties of the CMS membranes formed thereof. Last but not least, a very small amount of films can be made by in situ interfacial polymerization, which makes material characterizations challenging.

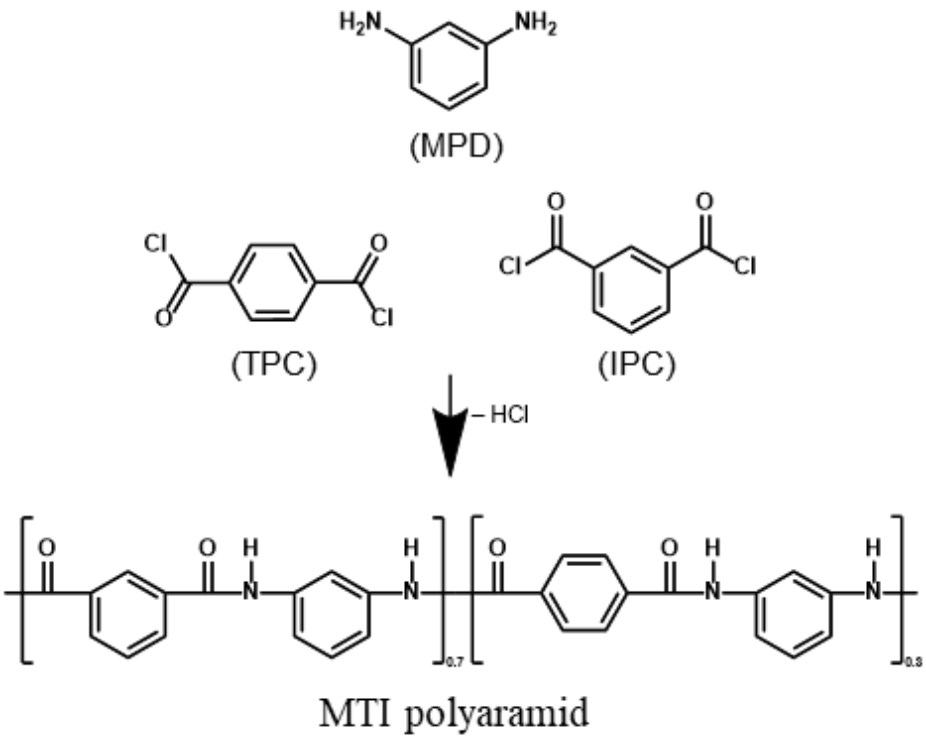

Figure 4.1: Polymerization reaction scheme for synthesis of MTI polyaramid.

To circumvent these challenges associated with crosslinked aramids, we synthesized an uncrosslinked aramid MPD-TPC/IPC (MTI) by stirred interfacial polymerization (Figure 4.1).[113, 123] m-phenylene diamine (MPD) was used as the aqueous phase monomer and a mixture of terephthaloyl chloride (TPC) and isophthaloyl chloride (IPC) was used as the organic phase monomers. Incorporating a mixture of structural isomers – TPC and IPC (3:7), as the organic phase monomers enhanced the polyaramid backbone asymmetry by causing increased frustration in polymer chain packing[60], thereby avoiding formation of semi-crystalline polymer and providing an amorphous polymer which can be dissolved in strong polar aprotic solvents. Table 4.1 shows the solubility of MTI polyaramid in different organic solvents.

Table 4.1: Solubility of the MTI polyaramid (2.5 wt%) in organic solvents at ambient condition. "++" indicates fully soluble and "-" indicates insoluble.

Solvent	Solubility
NMP	++
DMAc	++
DMSO	++
DMF	++
THF	-
Chloroform	-
DCM	-
DCE	-
Methanol	-
Ethanol	-
Isopropanol	-
Hexane	-
Benzene	-
Isopar™ G	-

The presence of basic additives in the reaction mixture affects the concentration of oligomeric units during synthesis. Higher concentration of oligomeric units can adversely affect the molecular weight of the polymer product. The hydrogen chloride (HCl) by-product of the condensation reaction between MPD and TPC/IPC is known to block the amino groups in the monomer and oligomers preventing formation of a high molecular weight polymer. To prevent this, 2 moles of sodium carbonate (Na_2CO_3) per mole of MPD monomer is added to the aqueous phase in the reaction mixture, which acts as a hydrogen chloride acceptor and contributes to improving the polymer yield.[113] A weak base like Na_2CO_3 is preferred over a strong base such as NaOH to avoid hydrolysis of the polymer chains. Vigorous stirring was employed to rapidly replenish the interface which also improved the polymer yield.[56] Hence, a

high molecular weight solution processable polyaramid was obtained with ~ 90% yield. Solution processability enabled formation of polyaramid dense films and hollow fibers from solution, which were used as precursors for fabrication of CMS membranes.

4.2.2 Characterization of polyaramid precursor

The MTI polyaramid precursor was characterized by: Capillary viscometry, Fourier transform infrared spectroscopy (FTIR), Differential scanning calorimetry (DSC), Thermogravimetric analysis (TGA) and Wide-angle X-ray diffraction (WAXD).

Insolubility of the MTI aramid in THF made it challenging to quantify its molecular weight by gel permeation chromatography. Inherent viscosity (η_{inh}) of a polymer can be used as a measure of the molecular weight of the polymer. η_{inh} was measured using capillary viscometry, with a dilute polyaramid solution (5 mg/mL in NMP). The polyaramid showed inherent viscosity of 1.05 dL/g, which was higher than the inherent viscosity (0.62 – 0.68 dL/g) reported for the commercial Matrimid® polyimide[124], indicating high molecular weight of the synthesized MTI polyaramid. High molecular weight of the polyaramid precursor ensures good polymer solution viscosity and spinnability, which is important for successful fabrication of precursor dense film and hollow fiber membranes. Moreover, the high molecular weight of the polyaramid precursor also ensures good structural integrity of the polyaramid-derived CMS membranes.

The successful formation of the polyaramid backbone was evidenced by FTIR spectroscopy (Figure 4.2). The presence of the amide (-CO-NH-) linkage and the absence of the acid chloride (-COCl) group confirms the formation of the polyaramid

structure and the successful completion of the polymerization reaction. Characteristic IR peaks at 1650 cm^{-1} and 1531 cm^{-1} correspond to the C=O stretching vibration of the amide group and the in-plane N-H bending and C-N stretching vibrations of the amide group, respectively. In addition, a characteristic stretching peak at 3300 cm^{-1} is associated to N-H (and O-H) vibrations suggesting NH---N and NH---O=C hydrogen bonds. Characteristic peaks at 1604 cm^{-1} and 1483 cm^{-1} correspond to aromatic ring breathing in the polymer chain. Moreover, the absence of acid chloride band at 1770 cm^{-1} confirms the absence of -COCl group.[113] The presence of the amide (-CO-NH-) linkage and the absence of the acid chloride (-COCl) group confirms the formation of the polyaramid structure and the successful completion of the polymerization reaction.

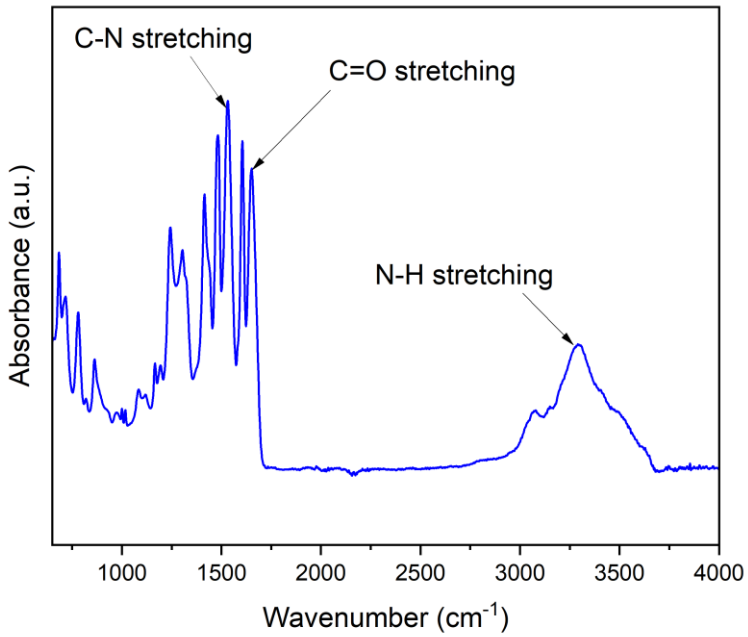

Figure 4.2: FTIR spectrum of the MTI polyaramid precursor.

TGA was carried out under continuous N_2 purge at flow rate of 50 cc/min. TGA result (Figure 4.3) shows that there was negligible weight loss from room temperature

up to 400°C, indicating negligible residual water vapor and/or residual solvent. An abrupt weight loss was observed above 400°C, indicating the onset of thermal decomposition of the polyaramid backbone. Hence, the thermal decomposition temperature (T_d) was considered as the onset temperature of thermal decomposition, which is 400°C for the polyaramid. The polyaramid had high residual carbon weight of ~50% at 950°C, suggesting the MTI aramid was a promising precursor material for CMS membrane formation.

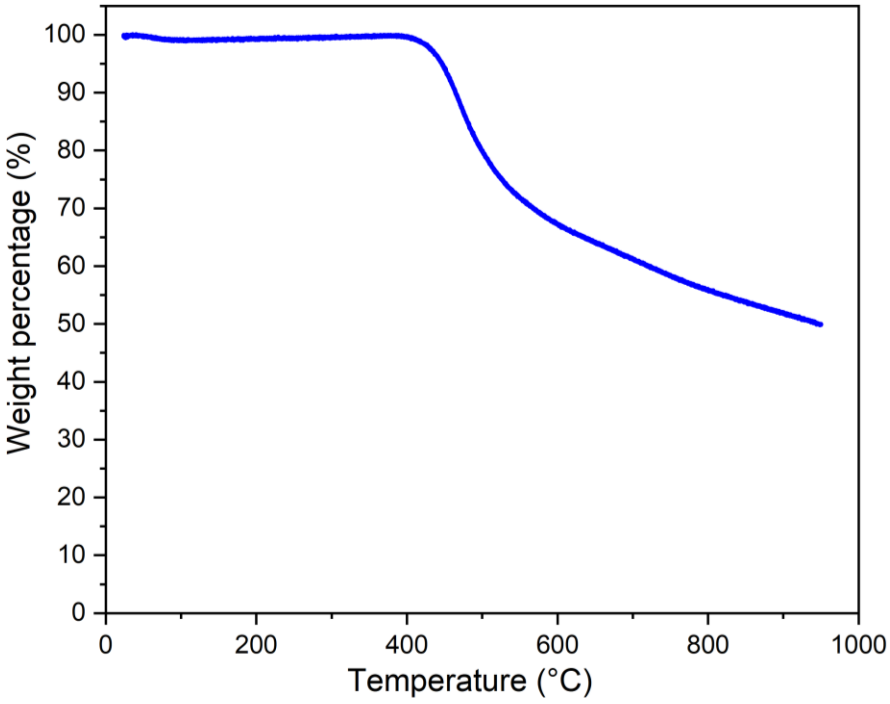

Figure 4.3: TGA weight loss profile for the MTI polyaramid under continuous N_2 purge.

DSC was used to measure the glass transition temperature (T_g) of the polyaramid (Figure 4.4). T_g of a polymer is related to the polymer chain rigidity. Higher T_g generally indicates stronger backbone rigidity. The polyaramid precursor exhibited

a high T_g of 275°C indicating a rigid polymer backbone.[90] Absence of endothermic/exothermic peaks in the DSC thermogram further indicated the highly amorphous nature of the polyaramid.

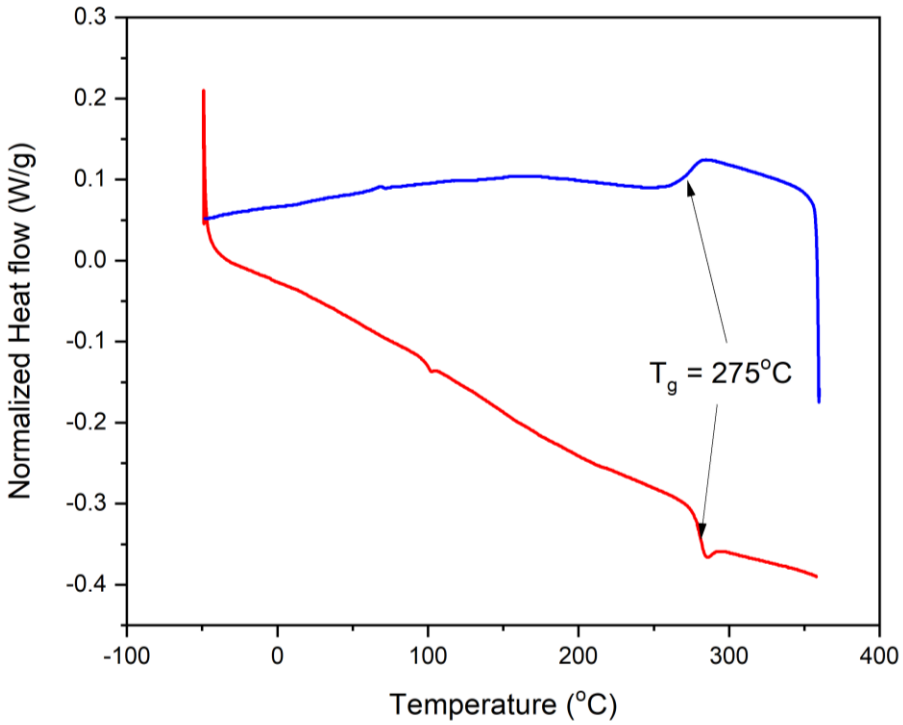

Figure 4.4: DSC thermogram for the MTI polyaramid indicating glass transition temperature (T_g). T_g is indicated as the temperature corresponding to the mid-point of the step change in slope of the thermogram.

A smaller difference between T_g and T_d of the polymer precursor is important to avoid undesirable substructure collapse during pyrolysis of polymer precursor and thereby produce CMS membranes with attractive gas separation performance.[90] $\Delta = T_d - T_g = 125$°C for the polyaramid precursor is larger than most polyimide precursors, indicating that the polyaramid precursor is less favorable for CMS hollow fiber membrane formation. However, this was less concerning for the scope of this research which involves studying the intrinsic gas separation performance of the polyaramid-

derived CMS membranes using dense-wall CMS hollow fibers, as mentioned in section 3.6 of Chapter 3. Recommendations for future work to circumvent this challenge are covered in Chapter 7. The T_g, T_d, residual carbon weight % and $\Delta = T_d - T_g$ are indicated in Table 4.2.

Table 4.2: Thermal decomposition temperature (T_d), glass transition temperature (T_g), residual carbon percentage, and the thermal decomposition-glass transition temperature difference ($\Delta = T_d - T_g$) for the MTI polyaramid precursor.

Parameter	Value
T_d	400°C
T_g	275°C
Residual carbon weight %	50.045 %
$\Delta = T_d - T_g$	125°C

WAXD was used to study the average d-spacing in the polyaramid precursor (Figure 4.5). The average d-spacing reflects the average interchain spacing between the polymer segments.[90] The average d-spacing is evaluated using Bragg's law as mentioned in section 3.8.7. The spectrum shows a broad amorphous peak at $2\theta \sim 23°$ with the average d-spacing indicated as 3.86Å. The average d-spacing for the polyaramid precursor is lower than most polyimide precursors due to the presence of more densely packed polymeric chains owing to the strong intermolecular hydrogen bonding interactions.

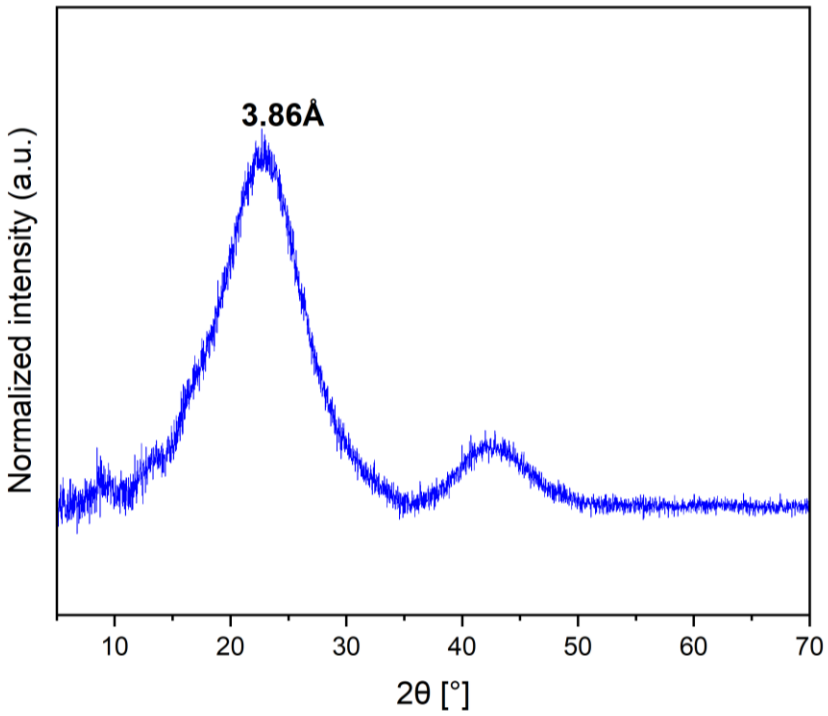

Figure 4.5: WAXD spectrum for the MTI polyaramid precursor.

Fractional free volume (FFV) for polymeric precursors is a commonly used quantity for developing structure-transport property relationship in polymeric membranes. The fractional free volume (FFV) of the MTI polyaramid was obtained by Eq. 3.7 using the measured polymer density (1.37 g/cm^3) for the polyaramid dense film and the V_w estimated by Park and Paul's method[117]. The FFV (0.057) is lower than most polymer precursors studied for CMS membrane formation, as shown in Table 4.3. This result agrees with the small average d-spacing of the polyaramid obtained from WAXD, which is evidently due to closely packed polymeric chains owing to the strong intermolecular hydrogen bonding interactions.

Table 4.3: Average d-spacing, density, and FFV of MTI polyaramid precursor.

Polymer	FFV
MTI	0.057
Matrimid®	0.110 [115]
6FDA-DAM	0.190 [115]
PIM-1	0.260 [125]

4.2.3 Fabrication of polyaramid precursor hollow fiber membranes and polyaramid-derived CMS hollow fiber membranes

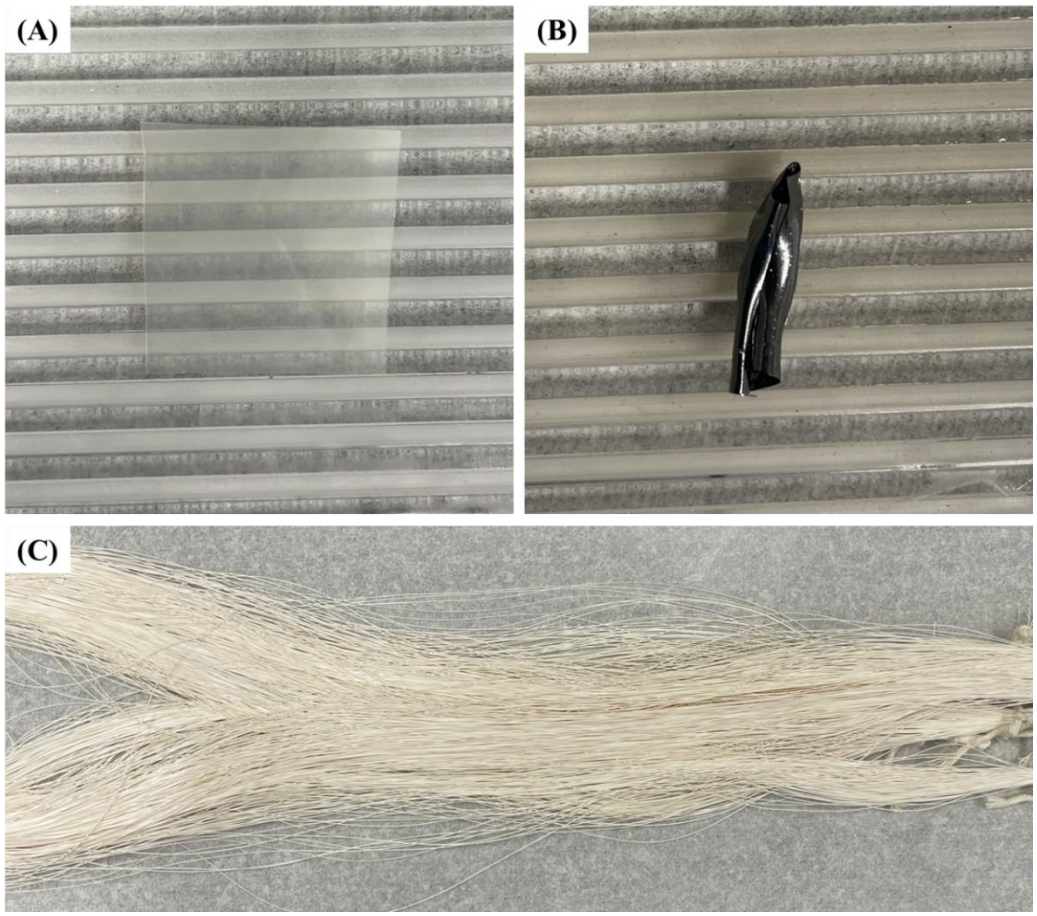

Figure 4.6: Photos showing (A) MTI aramid dense film, (B) CMS dense film made by pyrolysis of the MTI aramid dense film (C) Polyaramid precursor hollow fiber bundle made by dry-jet/wet-quench spinning. The CMS dense film was significantly curled.

The MTI polyaramid dense films were used as precursors to fabricate CMS dense films, which showed significant curling (Figure 4.6) preventing gas permeation measurements. The solution processability of the polyaramid allowed the fabrication of hollow fibers by dry-jet/wet-quench spinning. Hence, Monolithic MTI polyaramid precursor hollow fiber membranes were fabricated using the dry-jet/wet-quench spinning process. The polymer dope composition and spinning conditions are mentioned in Table 4.4. Figure 4.6C shows a picture of the polyaramid precursor hollow fiber bundle. The polyaramid precursor hollow fiber membranes showed H_2 permeance of 1394 GPU and H_2/CO_2 ideal selectivity of 3.92 under single-gas H_2/CO_2 permeation at room temperature. The H_2/CO_2 ideal selectivity was lower than Knudsen selectivity (4.69) and also lower than H_2/CO_2 ideal selectivity (~9) of the MTI polyaramid dense film, indicating presence of defects in the precursor hollow fiber.

Table 4.4: Polymer dope composition and hollow fiber spinning conditions for fabrication of MTI polyaramid precursor hollow fiber membranes.

Spinning Conditions	Unit	Value
Dope composition	wt% MTI	27.0
	wt% NMP	72.0
	wt% THF	1.0
Spinning temperature	°C	90
Quench bath temperature	°C	50
Dope/bore fluid flow rate	cc/h	150/50
Bore fluid composition	NMP/H_2O	72/28
Air gap height	cm	5
Fiber take-up rate	m/min	30

The polyaramid hollow fibers were used as precursors to provide four polyaramid-derived CMS hollow fiber membranes (MTI-550, MTI-675, MTI-800, and MTI-925) by pyrolysis at 550°C, 675°C, 800°C, and 925°C, respectively. Figure 4.7A

shows that both the polyaramid hollow fibers and polyaramid-derived CMS hollow fibers had excellent flexibility. CMS hollow fiber membranes are conventionally fabricated from precursor hollow fibers comprising highly rigid polymers with high glass transition temperature (T_g) above 320°C (e.g., polyimides, polybenzimidazoles). Pyrolysis of precursor hollow fibers comprising low-T_g polymers (e.g., PVDF) can lead to structural deformation in CMS hollow fiber membranes.[96] Although the MTI polyaramid had lower T_g (275°C) than polyimides and polybenzimidazoles, CMS hollow fiber membranes were successfully formed without any structural deformation.

Figure 4.7B shows the SEM images of the polyaramid precursor hollow fiber, which has an outer diameter of ~330 μm and shows an asymmetric porous structure with presence of finger-like pores called "macrovoids". The pores in the polyaramid precursor hollow fibers collapsed during pyrolysis (Figure 4.7(B-D)), thereby giving dense-wall CMS hollow fiber membranes with outer diameter ~140 μm. The porous substructure collapse occurs due to an increase in chain mobility of unoriented polymer chains thereby increasing chain packing density as the temperature crosses T_g during pyrolysis. Polymers with lower T_g and thereby lower polymer chain rigidity exhibit a greater degree of pyrolysis-induced pore collapse.[126] The thickness (~40 μm) of dense wall (separation layer) can be unambiguously determined to allow gas permeability measurements.[43]

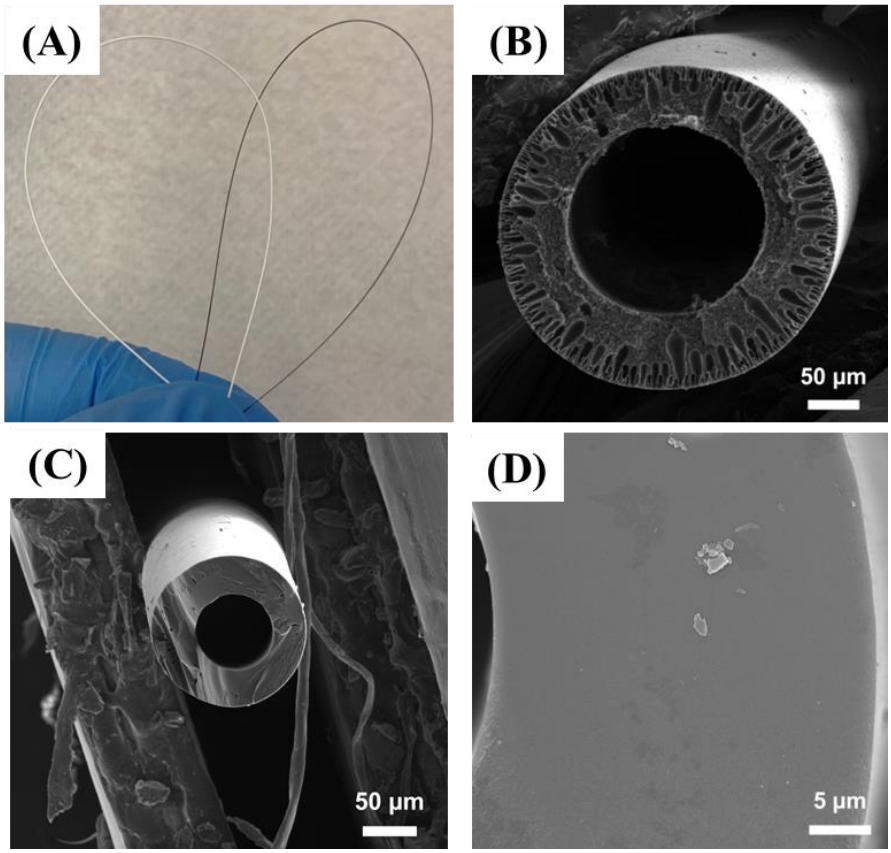

Figure 4.7: (A) Photo showing the excellent flexibility of the polyaramid hollow fiber (white) and polyaramid-derived CMS hollow fiber (black). SEM images of (B) polyaramid hollow fiber, (C) polyaramid-derived CMS hollow fiber, and (D) dense wall of polyaramid.

4.3 Gas permeation in polyaramid-derived CMS membrane

4.3.1 Single-gas permeation in polyaramid precursor membrane

Single-gas He, H_2, and CO_2 permeation measurements were carried out in the MTI polyaramid precursor dense film membrane using the constant-volume method at 35°C and 1 bar. The MTI polyaramid showed H_2/CO_2 ideal selectivity ~9, which was lower than the H_2/CO_2 ideal selectivity of MPD-TMC polyaramid (~19) measured at a similar temperature (22°C).[7] The higher selectivity in the MPD-TMC polyaramid

was possibly due to crosslinking that reduced polymer chain mobility.[15] The MTI polyaramid also had lower He/CO_2 ideal selectivity than the MPD-TMC polyaramid.

Both the intrinsic H_2/CO_2 and He/CO_2 separation performances of the MTI polyaramid precursor were unattractive and below the Robeson 2008 upper bounds.[28] Notably, single-gas H_2 permeability (1.7 Barrer) in the lower FFV MTI polyaramid was much lower compared to the higher FFV polymers such as fluorinated polyimides, and PIMs.[52, 127] This was possibly due to the strong hydrogen bonding interactions between the polymer chains causing the chains to be more tightly packed in the low FFV polyaramid compared to the higher FFV polymers.

4.3.2 Single-gas permeation in polyaramid-derived CMS membrane

Single-gas permeation of helium (He, d_k [kinetic diameter] = 2.6 Å), hydrogen (H_2, d_k = 2.89 Å), carbon dioxide (CO_2, d_k = 3.3 Å), nitrogen (N_2, d_k = 3.64 Å), and methane (CH_4, d_k = 3.8 Å) was measured in the dense-wall polyaramid-derived CMS hollow fiber membranes at 35 °C with feed at 10 bar. Two membrane modules at each pyrolysis temperature were prepared and tested to observe consistency in the results (Table 4.5).

Table 4.5: Permeabilities in polyaramid-derived CMS membranes measured using single-gas (10 bar) permeation at 35°C. Two hollow fiber membrane modules were tested for each polyaramid-derived CMS membrane. Each hollow fiber module consists of at least two CMS hollow fiber membranes. "-" indicates permeability was too low and cannot be reliably measured.

Membrane	Module #	P(He), Barrer	P(H_2), Barrer	P(CO_2), Barrer	P(N_2), Barrer	P(CH_4), Barrer
MTI-550	M1	303.4	747.2	376.3	17.7	11.9
	M2	265.0	627.5	300.5	11.9	6.6
MTI-675	M1	269.4	629.7	103.3	2.6	0.52
	M2	244.2	628.6	117.9	3.3	0.70
MTI-800	M1	44.1	86.2	4.0	0.058	-
	M2	35.6	63.9	2.9	0.034	-
MTI-925	M1	7.2	8.3	0.020	-	-
	M2	8.2	9.8	0.031	-	-

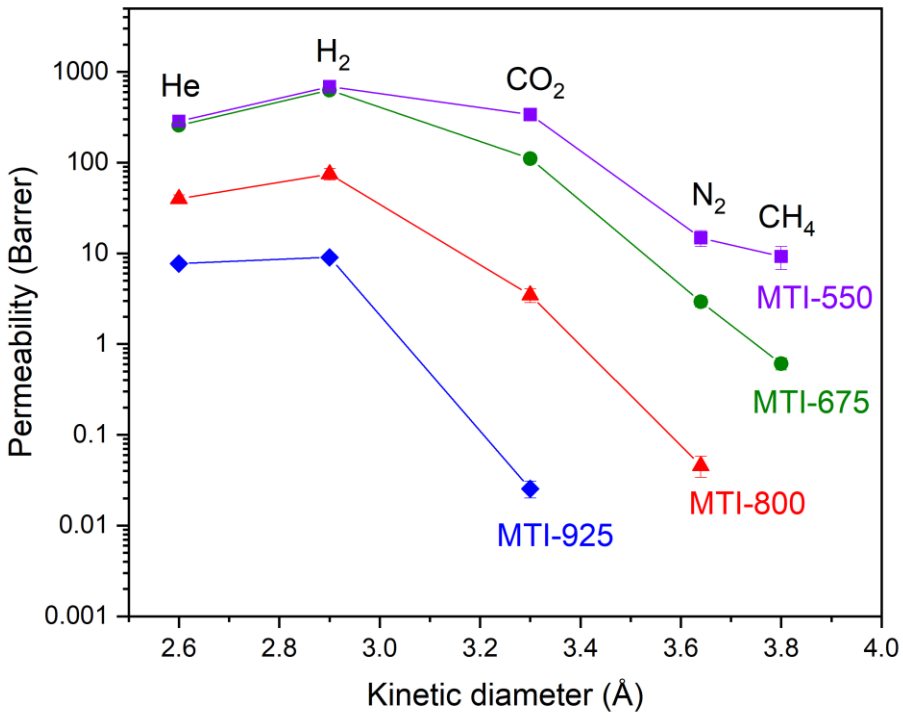

Figure 4.8: Single-gas permeability in polyaramid-derived CMS membranes derived at different pyrolysis temperatures (10 bar, 35°C).

The effect of pyrolysis temperature on single-gas permeability is shown in Figure 4.8. Gas permeability reduced as the pyrolysis temperature increased. The decrease in permeabilities of larger gases (CO_2, N_2, and CH_4) was more sensitive to pyrolysis temperature than the permeabilities of the smaller gases (He and H_2). Notably, permeability of gases with larger kinetic diameter could not be measured at in CMS membranes pyrolyzed at 800 and 900 ℃ as the permeation flux was lower than the instrument detection limit. The H_2/CO_2, H_2/N_2, and H_2/CH_4 ideal selectivities were substantially enhanced with increase in pyrolysis temperature (Figure 4.9). This is possibly due to refining of the CMS ultramicropores at higher pyrolysis temperatures.[48] Moreover, He/H_2 ideal selectivity was < 1 for all pyrolysis temperatures and increased with increase in pyrolysis temperature. He being a smaller molecule than H_2 provides He/H_2 diffusion selectivity > 1; but as H_2 is significantly more condensable than He, He/H_2 sorption selectivity is << 1, leading to He/H_2 ideal selectivity < 1. The He/H_2 selectivity increases with increase in pyrolysis temperature as the He/H_2 diffusion selectivity increases more significantly compared to the He/H_2 sorption selectivity as the CMS pore structure becomes more compact at higher pyrolysis temperatures.[50]

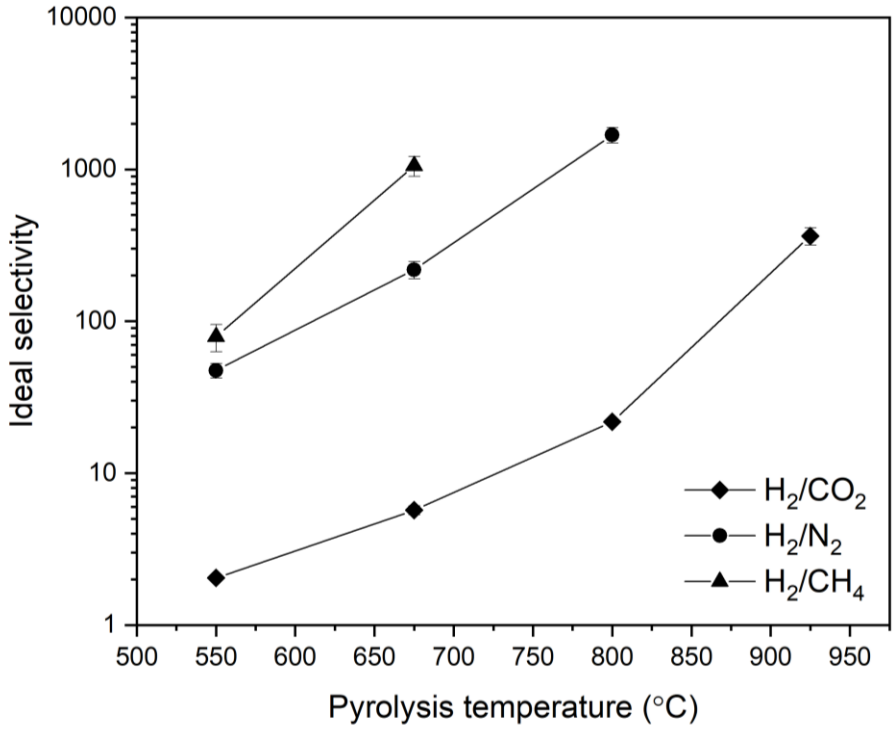

Figure 4.9: Ideal selectivity in polyaramid-derived CMS membranes derived at different pyrolysis temperatures (10 bar, 35°C).

The polyaramid-derived CMS membranes showed particularly competitive H_2/CO_2 separation performance (Figure 4.10). Following pyrolysis at 550℃, the polyaramid-derived CMS membrane (MTI-550) showed more than 400 times higher H_2 permeability than the MTI polyaramid precursor, which can be attributed to formation of CMS micropores. As the pyrolysis temperature further increased, the H_2 permeability dropped with enhanced H_2/CO_2 ideal selectivity. Notably, the CMS membrane pyrolyzed at 925℃ (MTI-925) had H_2/CO_2 separation performance well above the 2008 Robeson upper bound[28] with H_2 permeability of 9.1 Barrer and H_2/CO_2 ideal selectivity of 366, which were ~5 times and ~76 times higher than the MTI polyaramid precursor, respectively.

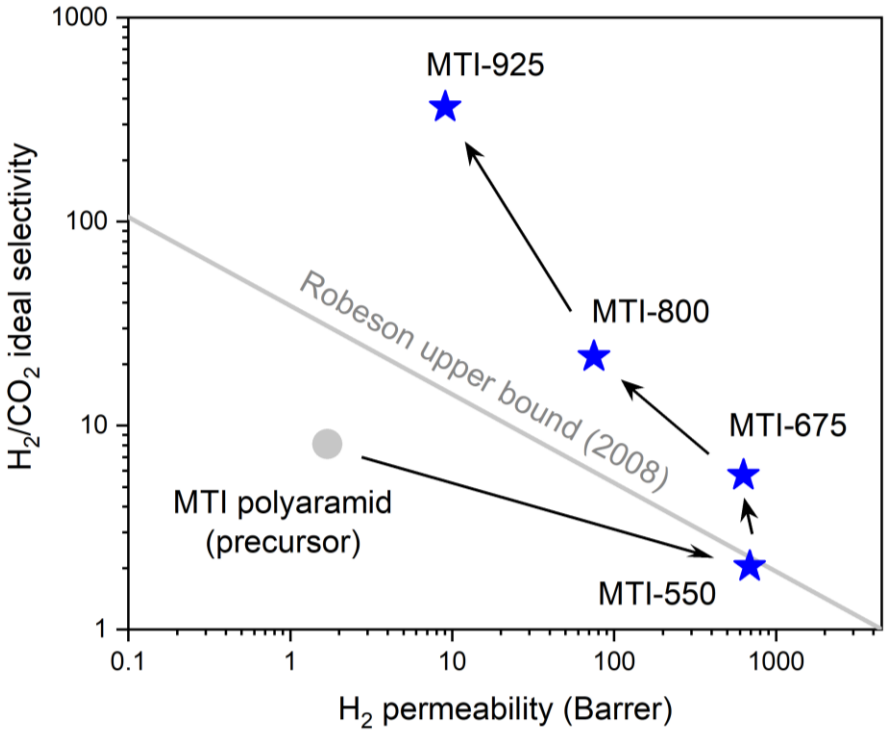

Figure 4.10: Single-gas H_2/CO_2 separation performance of the MTI polyaramid precursor and polyaramid-derived CMS membranes. Permeation test on the precursor membrane was performed at 1 bar and 35°C. Permeation tests on the CMS membranes were performed at 10 bar and 35°C.

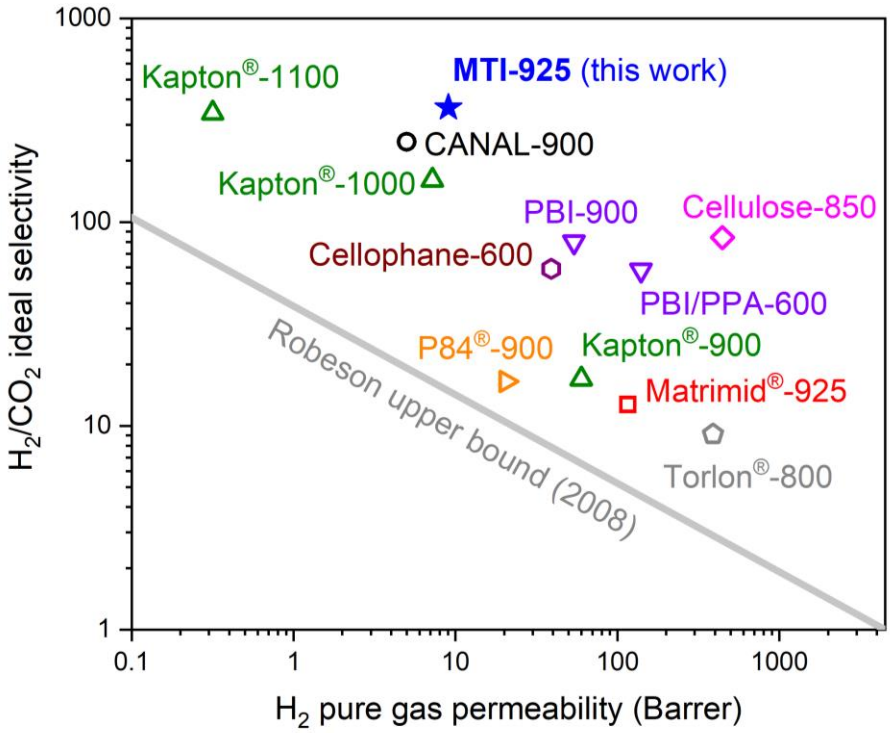

Figure 4.11: Comparing the H_2/CO_2 separation performance of polyaramid-derived CMS membrane (MTI-925) with other CMS membranes reported in literature. The labels are indicated as "polymer precursor-pyrolysis temperature".

The H_2/CO_2 single-gas separation performance of MTI-925 is compared with other CMS membranes reported in literature (Figure 4.11). As shown in the figure, MTI-925 had the highest H_2/CO_2 ideal selectivity among all known CMS membranes, which include those derived from polyimides (Kapton®, Matrimid®)[43, 49], polyamide-imides (Torlon®)[52], PBIs[10, 11], PIMs[50] and cellulose[41, 53] as shown in Table 4.6. Additionally, MTI-925 had competitive H_2 permeability among CMS membranes with H_2/CO_2 ideal selectivity above 100. Kapton®-derived CMS membranes[49] showed comparable H_2/CO_2 ideal selectivity; however, were pyrolyzed at higher temperature (1100°C) and had much lower H_2 permeability (~0.32 Barrer).

Table 4.6: H_2/CO_2 single-gas separation performance of CMS membranes reported in literature.

Precursor	$T_{pyrolysis}$ (°C)	P (H_2) (Barrer)	α (H_2/CO_2)	$T_{permeation}$ (°C)	P_{feed} (bar)	Membrane geometry
Cellulose[41]	850	445	83.9	130	2	Hollow fiber
Cellophane[53]	600	39	59	30	2	Film
PBI[10]	900	54	80	100	7.4	Film
PBI/PPA[11]	600	140	58	150	6.5	Film
Matrimid®[43]	900	230	8.5	35	7	Hollow fiber
P84® [128]	900	20.5	16.5	100	1	Hollow fiber
Torlon® [52]	800	390	9.1	35	10	Film
Kapton® [49]	900	60	17	50	2	Film
Kapton® [49]	1000	7.2	161	50	2	Film
Kapton® [49]	1100	0.32	343	50	2	Film
CANAL[50]	850	10.8	162	35	10	Film
CANAL[50]	900	5.0	248	35	10	Film
MTI(this work)	925	9.1	366	35	10	Hollow fiber

4.3.3 Mixed-gas permeation in polyaramid-derived CMS membrane

Mixed-gas permeation was carried out in MTI-925 using an equimolar H_2/CO_2 mixture (2 bar) at 35 °C. Mixed-gas permeation was not carried out for MTI-800, MTI-675, and MTI-550 due to less attractive H_2/CO_2 selectivities. Figure 4.12 shows the mixed-gas permeation results with the variation of mixed-gas permeability and separation factor through the time-lag, transient and steady-state phases of permeation. The measurement was continuously carried out for ~10 days after the steady-state phase was reached. Once steady-state permeation was reached, the polyaramid-derived CMS membrane showed stable H_2 permeability of 3.5 Barrer and H_2/CO_2 separation factor of 156. The separation factor was lower than the H_2/CO_2 ideal selectivity measured under single-gas permeation. The lower H_2/CO_2 separation factor was

possibly due to competitive CO_2 sorption effect under mixture permeation, which was widely observed in CMS membranes reported in literature.[41] This fact notwithstanding, MTI-925 still gave one of the highest H_2/CO_2 separation factors among all known CMS membranes as shown in Figure 4.13 and Table 4.7.

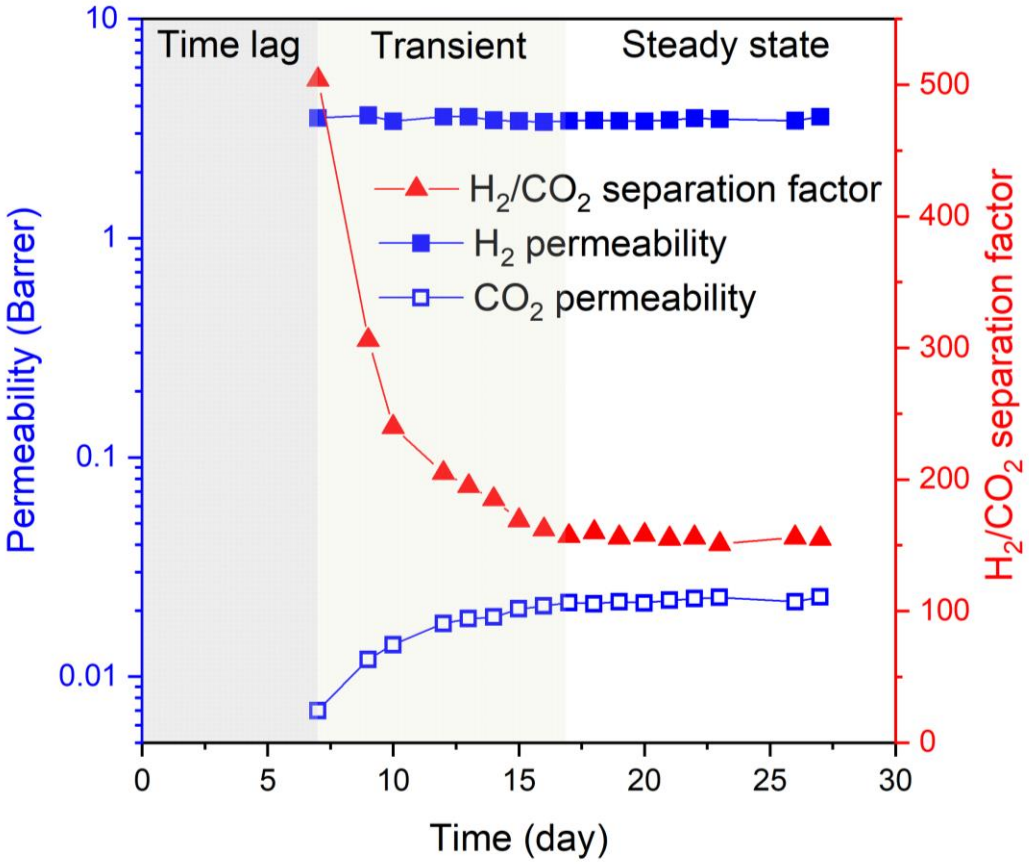

Figure 4.12: Mixed-gas H_2/CO_2 permeation in MTI-925 using an equimolar H_2/CO_2 mixture at 2 bar and 35°C.

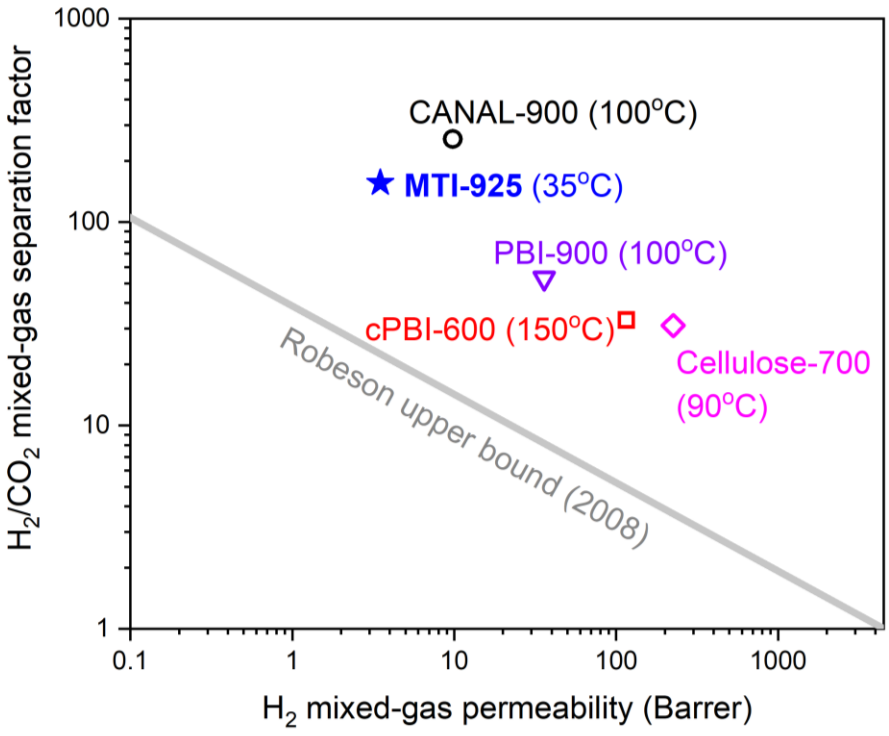

Figure 4.13: Comparing the H_2/CO_2 mixed-gas separation performance of aramid-derived CMS membrane with CMS membranes reported in literature.

4.4 Gas sorption and diffusion in polyaramid-derived CMS membrane

H_2 and CO_2 sorption (Figure 4.14) was studied in the polyaramid-derived CMS dense films at 35°C using a physisorption analyzer to deconvolute the contributions from sorption selectivity and diffusion selectivity. The CO_2 and H_2 sorption isotherms were fit with the dual-mode sorption model[74] and Henry's law, respectively. Indeed, H_2 sorption in porous carbon appeared linear at room temperature at pressure up to 30 bar.[129] Table 4.7 shows the sorption parameters evaluated by fitting Henry's law to the H_2 sorption isotherm and the dual-mode sorption model to the CO_2 sorption isotherm. The obtained sorption constants allow the evaluation of H_2/CO_2 diffusion selectivities according to the sorption-diffusion theory using measured H_2/CO_2 ideal

selectivities (Figure 4.15). Slow permeation in MTI-800 and MTI-925 allowed determination of H_2/CO_2 diffusion selectivities using the time-lag method (Figure 4.16), which were in excellent agreement with those determined by the sorption-diffusion theory. [130]

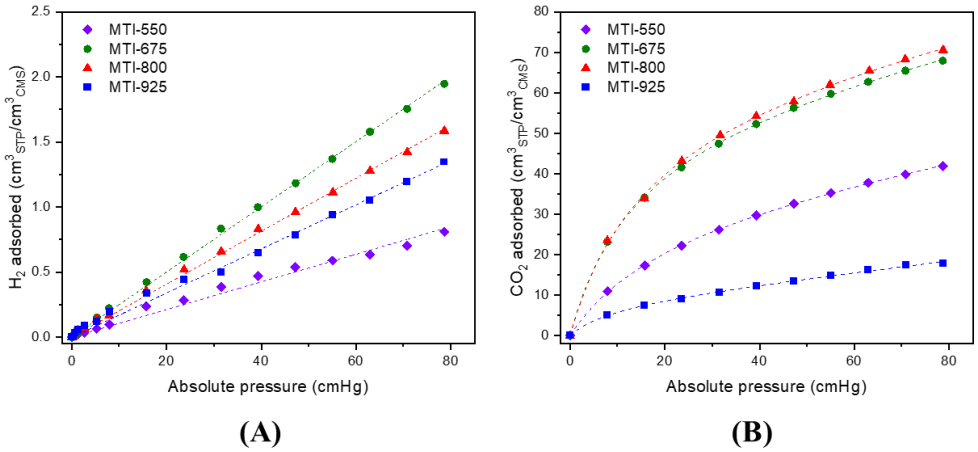

(A) **(B)**

Figure 4.14: (A) H_2 and (B) CO_2 sorption isotherms (35°C) for polyaramid-derived CMS membranes derived at different pyrolysis temperatures.

Table 4.7: Sorption parameters of the polyaramid-derived CMS membranes obtained from fitting the experimental sorption isotherms with Henry's Law (H_2) and the dual-mode sorption model (CO_2).

CMS membrane	H_2	CO_2		
	k_d, $cm^3(STP)/cm^3(CMS)$ cmHg	k_d, $cm^3(STP)/cm^3(CMS)$ cmHg	C_H', $cm^3(STP)/cm^3(CMS)$	b, $cmHg^{-1}$
MTI-550	0.0106	0.202	33.16	0.048
MTI-675	0.0251	0.246	57.60	0.072
MTI-800	0.0204	0.239	62.69	0.063
MTI-925	0.0170	0.135	8.543	0.105

As the pyrolysis temperature increased, the H_2/CO_2 diffusion selectivity dramatically increased from 46 (MTI-550) to 3052 (MTI-925), which was possibly due

to tightening of CMS ultramicropores.[48] The highly condensable CO_2 sorbs more strongly than H_2 giving H_2/CO_2 sorption selectivities well below 1. Interestingly, MTI-925 had much lower CO_2 sorption capacity than those pyrolyzed at lower temperatures. The reduced CO_2 sorption capacity caused the H_2/CO_2 sorption selectivity to rise by 170% from 0.043 (MTI-550) to 0.116 (MTI-925), which contributed to the ultra-high H_2/CO_2 ideal selectivity in MTI-925. The reduction in CO_2 sorption capacity and hence synergistically increased H_2/CO_2 sorption selectivity can presumably be attributed to the formation of "H_2-selective micropores" only allowing the smaller H_2 molecules to sorb but excluding the larger CO_2 molecules.[43] These H_2-selective micropores were formed possibly by ultramicropore tightening as the CMS structure became more ordered and graphitic at higher pyrolysis temperatures.

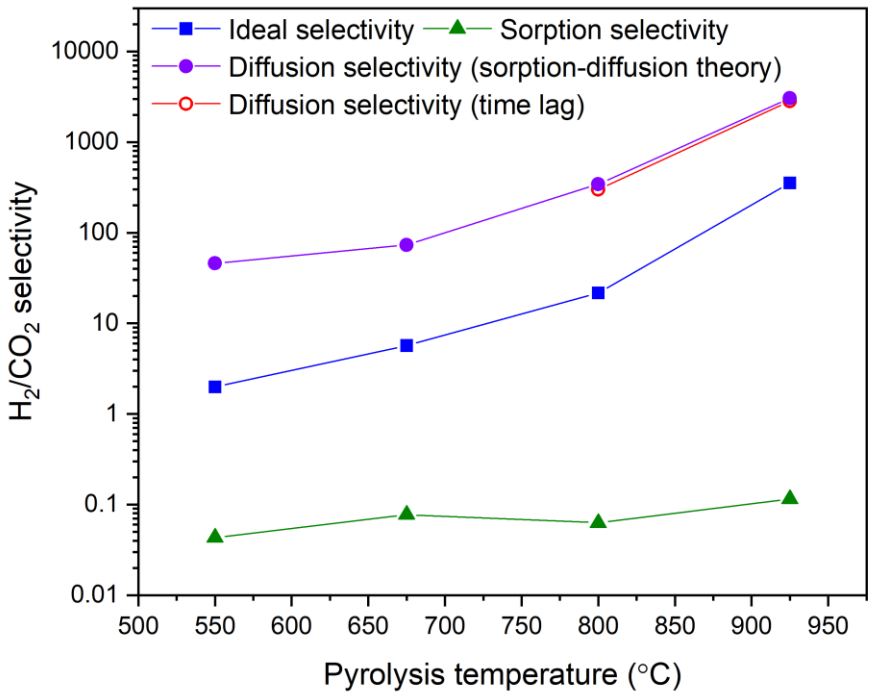

Figure 4.15: Effect of pyrolysis temperature on H_2/CO_2 ideal selectivity, diffusion selectivity, and sorption selectivity in polyaramid-derived CMS membranes.

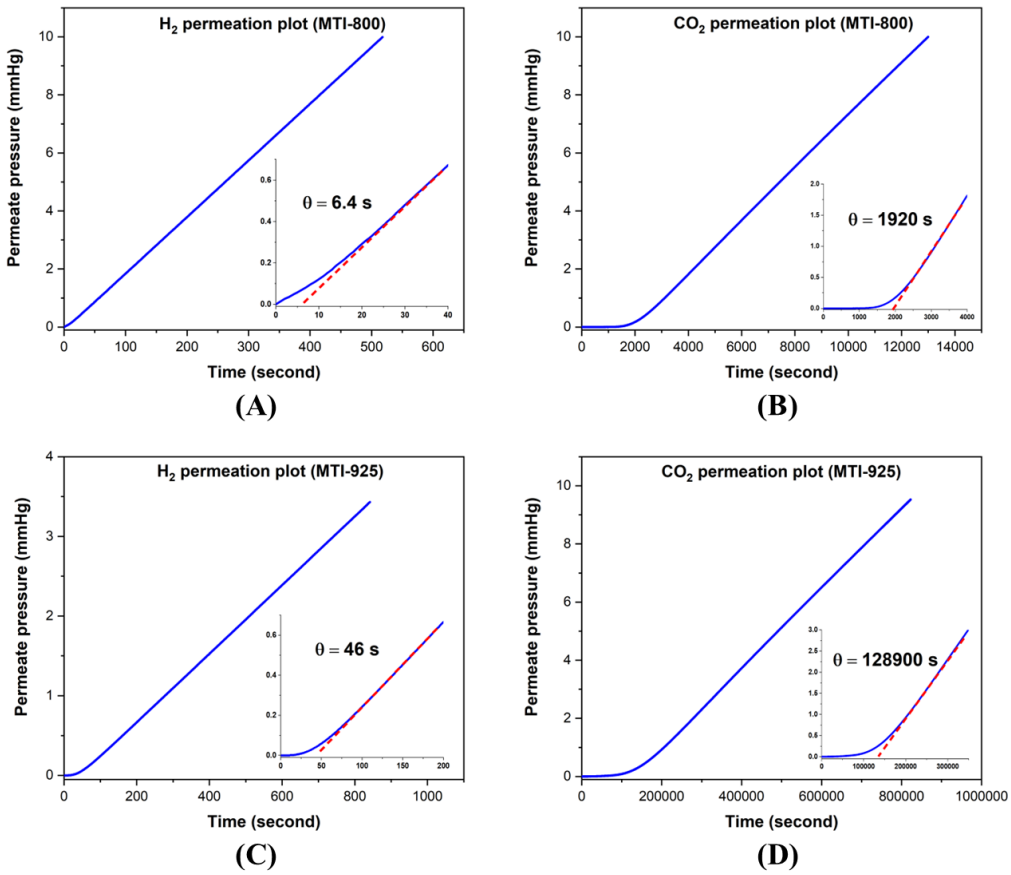

Figure 4.16: H_2 and CO_2 permeation plots in MTI-800 and MTI-925. The insets illustrate the determination of permeation time lags (θ).

4.5 Characterization of polyaramid-derived CMS membranes

Characterization of the polyaramid-derived CMS membranes allowed us to understand the permeation results shown in section 4.3 and 4.4. The polyaramid-derived CMS dense films were characterized using FTIR, WAXD, Raman spectroscopy, and CO_2 porosimetry.

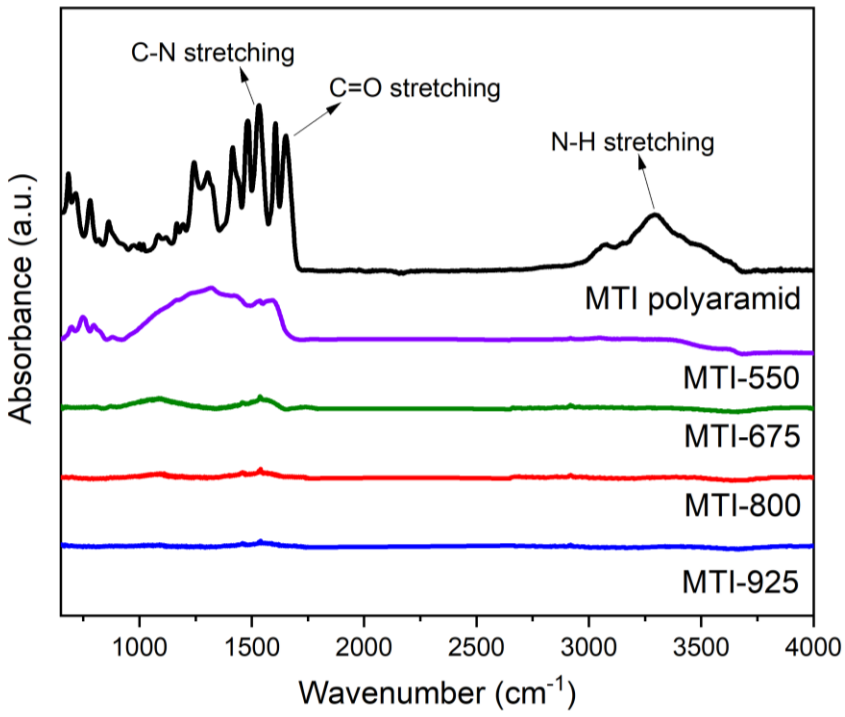

Figure 4.17: FTIR spectra of the MTI polyaramid precursor and polyaramid-derived CMS membranes.

FTIR spectra of the polyaramid-derived CMS membranes made at different pyrolysis temperatures are shown in Figure 4.17. Several low intensity peaks were seen in the FT-IR spectra (800-1600cm^{-1}) of MTI-550, suggesting the polymer decomposition was incomplete at 550℃. The peaks became weaker in MTI-675 and MTI-800 and disappeared in MTI-925, which indicated complete aramid decomposition.

The WAXD spectra of the polyaramid-derived CMS membranes at different pyrolysis temperatures are shown in Figure 4.18A. The average d-spacing calculated from the main diffraction peak position reduced as the pyrolysis temperature of polyaramid-derived CMS membrane increased from 550 to 800℃, suggesting

tightening of the CMS membrane pore structure. Although MTI-925 showed identical average d-spacing with MTI-800, MTI-925 had a stronger secondary diffraction peak at 2θ ~44° corresponding to the (100) lattice plane of graphite[92] which indicates a more ordered graphitic structure. Therefore, the results of WAXD corroborate with permeation results that the CMS ultramicropore structure was tightened at higher pyrolysis temperature. Formation of a more ordered and compact carbon structure was further evidenced by higher density of CMS membranes made at higher pyrolysis temperature, as shown in Figure 4.18B.

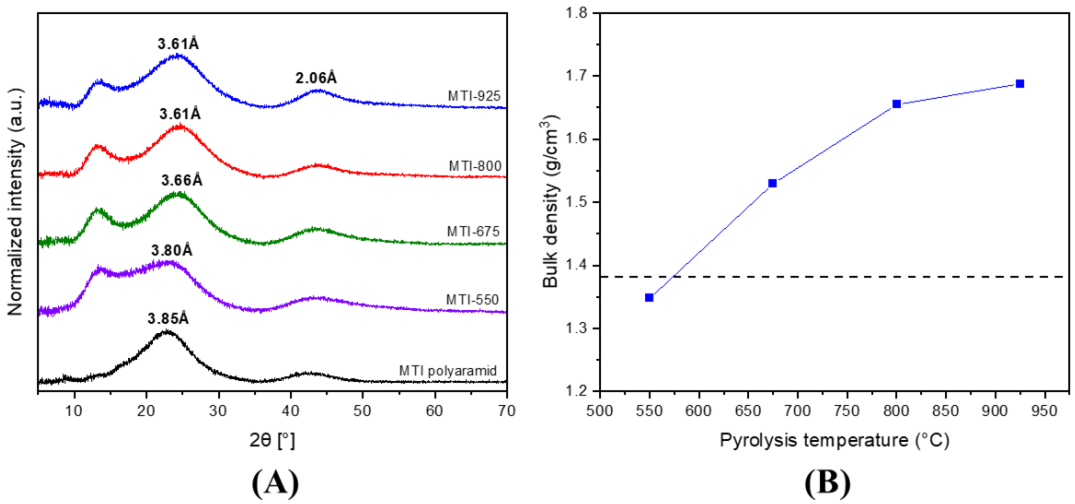

Figure 4.18: (A) WAXD patterns of the MTI polyaramid and polyaramid-derived CMS membranes; (B) Effect of pyrolysis temperature on the bulk density of polyaramid-derived CMS membranes (The line was drawn to guide the eye). The dashed line represents the bulk density of the MTI polyaramid precursor.

Raman spectra of the polyaramid-derived CMS membranes at different pyrolysis temperatures are shown in Figure 4.19. The spectra showed a D band (~1355 cm^{-1}) and a G band (~1575 cm^{-1}) characteristic of carbon materials. The spectra were deconvoluted into five bands, i.e., D1, D2, D3, D4, and G using a Gaussian

function.[98] The D1 and G band intensity ratio (I_{D1}/I_G) represents the relative concentration of sp^3- to sp^2-hybridized carbons.[98] MTI-675 showed higher I_{D1}/I_G ratio than MTI-550, suggesting MTI-675 is richer in sp^3-hybridized carbon. This is consistent with FTIR results that the polymer precursor decomposition was incomplete at 550°C. As the pyrolysis temperature increased to 925°C, the I_{D1}/I_G ratio reduced, suggesting higher concentrations of sp^2-hybridized carbon and hence a more ordered graphitic structure agreeing with the WAXD and density measurement results.

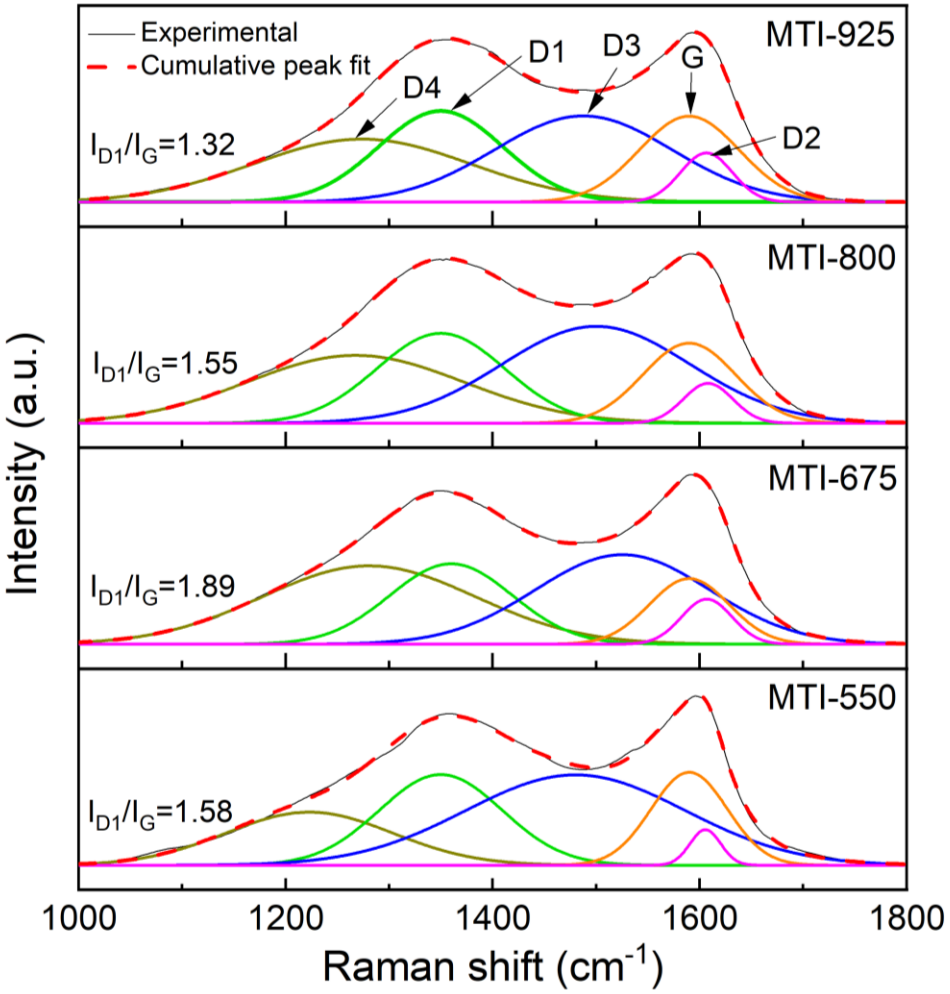

Figure 4.19: Raman spectra of polyaramid-derived CMS membranes.

The pore size distribution (Figure 4.20A) and cumulative pore volume (Figure 4.20B) in polyaramid-derived CMS membranes at different pyrolysis temperatures were obtained using the density functional theory (DFT) based on CO_2 physisorption isotherms measured at 0°C. A strong peak appeared in MTI-800 at ~4 Å suggesting tightening of ultramicropores. Interestingly, the measured pore volume was significantly reduced in MTI-925 with almost no ultramicropores smaller than 4.5 Å. While this appeared to be inconsistent with permeation results, it can be explained by the aforementioned H_2-selective micropores. As they cannot be accessed by CO_2 molecules due to exclusion, these H_2-selective micropores are not measurable by CO_2 physisorption. While CO_2 physisorption is broadly used to study carbon pore structure[131], these findings indicate this approach may not be suitable for CMS membranes with ultra-high H_2/CO_2 selectivities.

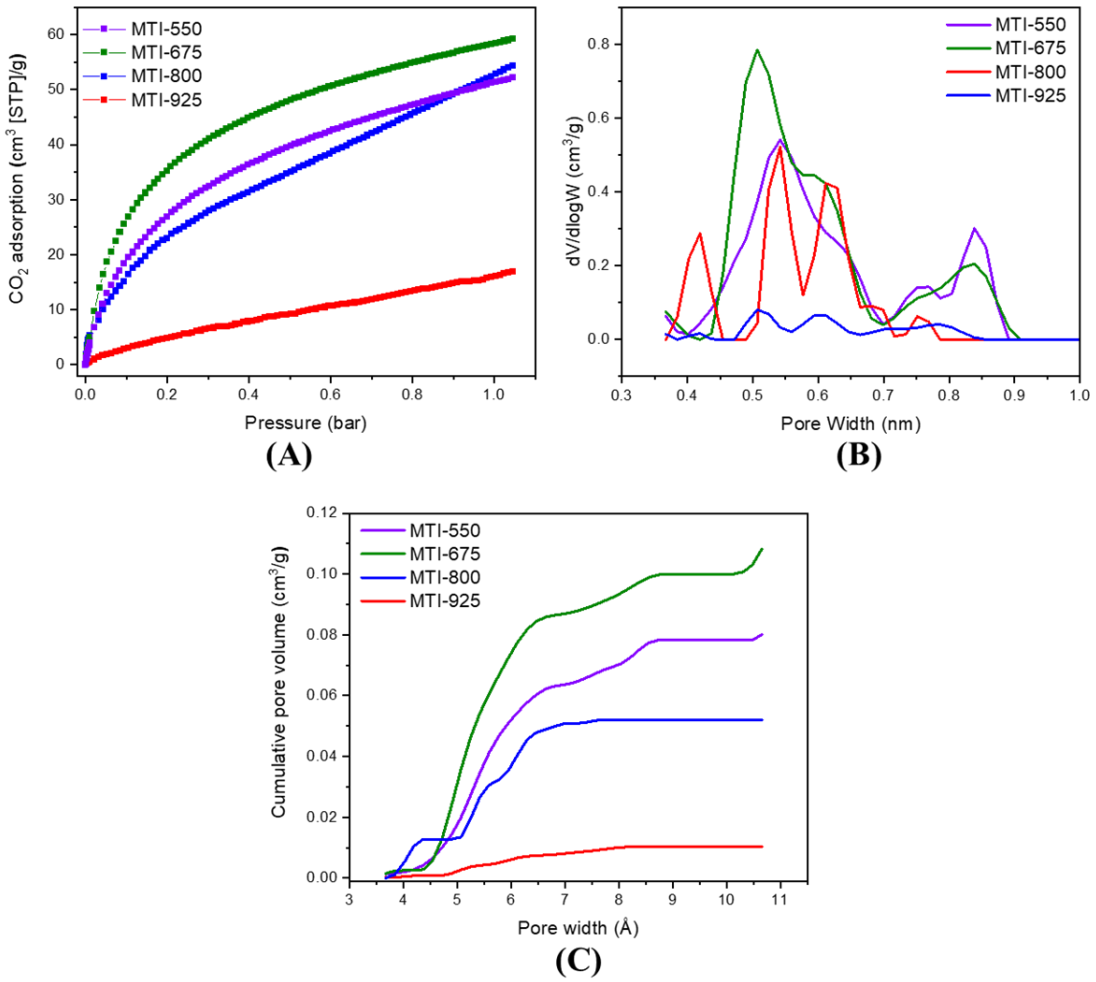

Figure 4.20: (A) CO_2 sorption isotherms (0°C), (B) Pore size distribution and (C) cumulative pore volume (CO_2 physisorption, 0°C) of polyaramid-derived CMS membranes derived at different pyrolysis temperatures.

Chapter 5: High-temperature H_2/CO_2 separation in polyaramid-derived CMS membranes

5.1 Overview

Although the polyaramid-derived CMS membrane described in Chapter 4 showed outstanding H_2/CO_2 ideal selectivity under single-gas permeation, the H_2/CO_2 separation factor dropped by more than 50% under mixture permeation. Membranes with ultra-high H_2/CO_2 separation factors are required to produce high purity H_2 product from the steam methane reforming process. Additionally, membranes must maintain attractive H_2/CO_2 separation performance at realistic syngas operating temperatures of 200-300°C under mixed-gas feed from the water-gas shift reactor.[15] Results in Chapter 4 suggest that higher H_2/CO_2 selectivity can be obtained at higher pyrolysis temperature. In this chapter, polyaramid-derived CMS hollow fiber membranes were fabricated using a pyrolysis temperature of 1050°C (MTI-1050) to further push the limit of H_2/CO_2 selectivity. Section 5.2 describes the effect of permeation temperature (200-300°C) on the separation performance of the MTI-1050 CMS membrane, which showed exceptionally high and stable H_2/CO_2 separation factor. The pore structure of the MTI-1050 was characterized and compared with the MTI-925 CMS membrane in section 5.3. Finally, a one-dimensional hollow fiber membrane separator model is used in section 5.4 to demonstrate the attractiveness of the MTI-1050 CMS membrane for enrichment of high-purity H_2.

5.2 High-temperature H_2/CO_2 mixed-gas permeation in polyaramid-derived CMS membrane

5.2.1 Fabrication of polyaramid precursor hollow fiber membranes and polyaramid-derived CMS hollow fiber membranes

Polyaramid-derived CMS hollow fiber membranes (outer diameter ~ 713 μm) were made by pyrolysis of polyaramid precursor hollow fiber membranes at 1050°C (MTI-1050). Polyaramid precursor hollow fibers were fabricated using dry-jet/wet-quench spinning with the polymer dope composition and spinning conditions given in Table 5.1. SEM images of the polyaramid precursor fiber and polyaramid-derived CMS fiber are shown in Figure 5.1. Pyrolysis induced pore densification caused the porous structure in the precursor hollow fiber to collapse under heat treatment during pyrolysis to provide CMS fibers with dense walls containing few macrovoids.[126] The CMS fibers were ~50 cm in length, having an outer diameter of ~323 μm with a dense wall thickness of ~ 43 μm. The volume fraction of macrovoids was estimated using GNU Image Manipulation Program (GIMP) with multiple cross-section SEM images of the CMS fiber (Figure 5.1C) to calculate the effective dense wall thickness (i.e., separation layer thickness). The CMS fibers had a macrovoids volume fraction of 4.9% and effective dense wall thickness of ~ 41 μm, which was used for membrane permeability calculations.

Table 5.1: Polymer dope composition and spinning conditions used to fabricate MTI polyaramid precursor hollow fiber membranes.

Spinning Conditions	Unit	Value
Dope composition	wt% MTI	27.0
	wt% NMP	72.0
	wt% THF	1.0
Spinning temperature	°C	90
Quench bath temperature	°C	50
Dope/bore fluid flow rate	cc/h	150/150
Bore fluid composition	NMP/H_2O	72/28
Air gap height	cm	3
Fiber take-up rate	m/min	10

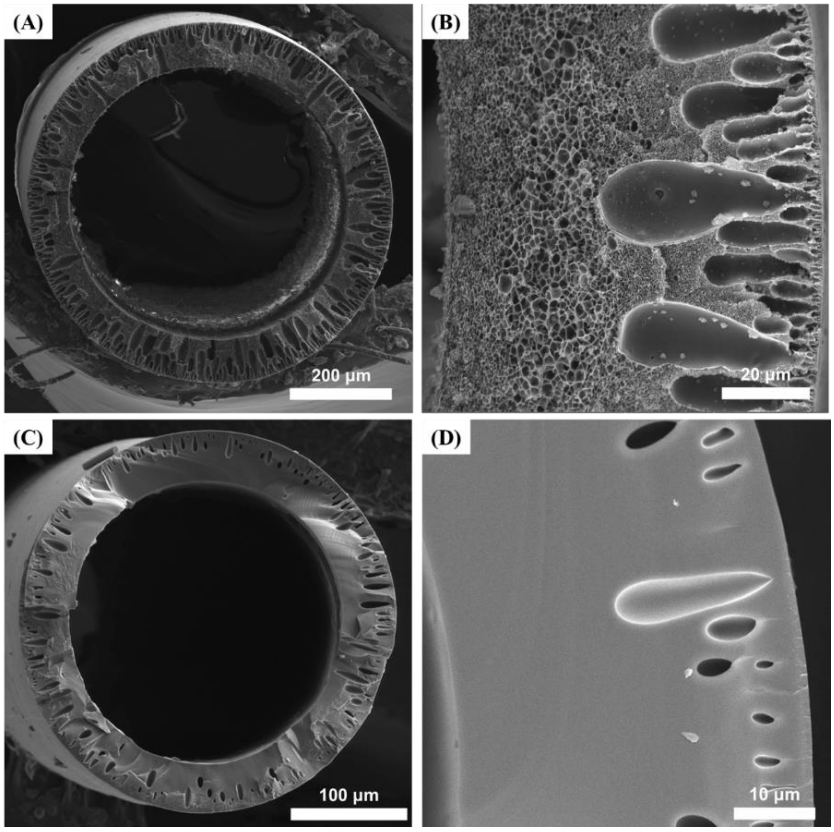

Figure 5.1: SEM images of polyaramid precursor hollow fiber membranes and polyaramid-derived CMS hollow fiber membranes at 1050°C (i.e., MTI-1050). (B) Precursor hollow fiber overview; (C) Precursor hollow fiber wall; (D) CMS hollow overview; (E) CMS hollow fiber wall.

5.2.2 Effect of permeation temperature on H_2/CO_2 separation performance

Mixed-gas H_2/CO_2 permeation measurements were performed using the constant-volume permeation method with a 10 mol% H_2/90 mol% CO_2 feed mixture at 2 bar. Permeation experiments were performed at temperatures of 200°C, 225°C, 250°C and 300°C to study the effect of permeation temperature on the membrane separation performance (Figure 5.2).

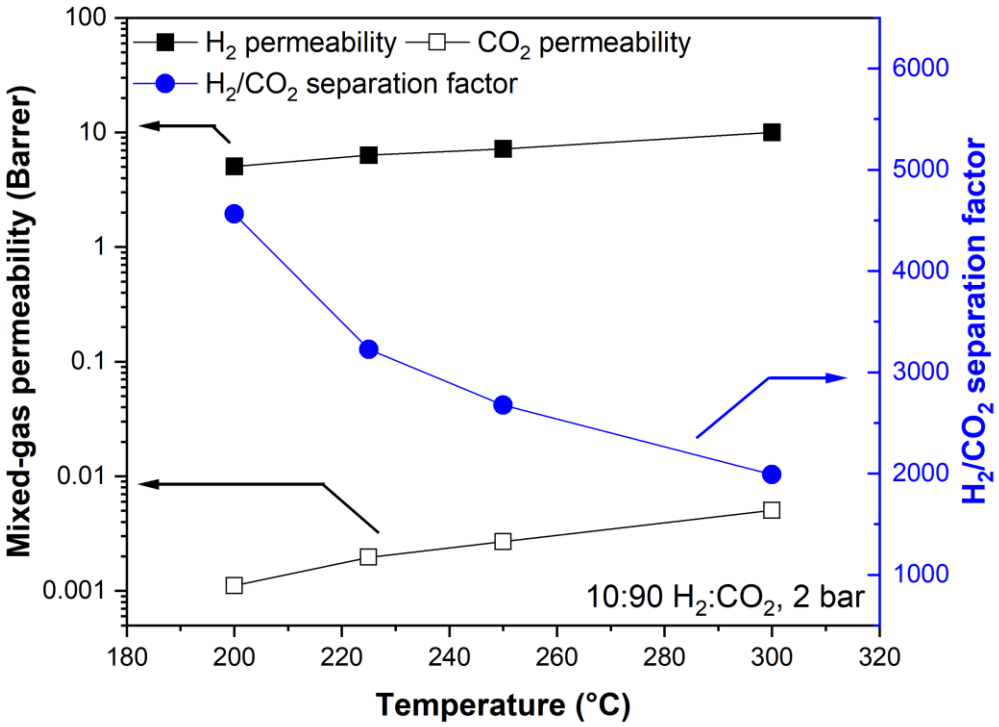

Figure 5.2: Mixed-gas H_2 and CO_2 permeabilities and H_2/CO_2 separation factors in the MTI-1050 CMS membrane. The permeation tests were conducted using 10% H_2/90% CO_2 mixture feed at 2 bar.

At 200°C, the MTI-1050 CMS membrane showed H_2 permeability of 5.1 Barrer and exceptionally attractive H_2/CO_2 separation factor of 4565. As the permeation temperature increased, both H_2 and CO_2 permeabilities increased with a drop in H_2/CO_2

separation factor. At 300°C, the H_2 permeability increased by a factor of 2 from 5.1 Barrer to 10 Barrer, while the H_2/CO_2 separation factor decreased by a factor of 2.3 from 4565 to 1988. Figure 5.3 shows that the Arrhenius plots of H_2 and CO_2 permeabilities both had good linearity. Permeation activation energy (E_P, kJ/mol) of H_2 and CO_2 were evaluated from the slope of the Arrhenius plots based on the Arrhenius equation (Eq 2.11). The E_P of H_2 (15.1 kJ/mol) was smaller than the E_P of CO_2 (33.4 kJ/mol), which explains the drop in H_2/CO_2 separation factor with increasing permeation temperature.

Interestingly, this observation is opposite to the trend seen in a number of CMS membranes.[7, 41, 51] For example, Lei et al. reported cellulose-derived CMS hollow fiber membranes at 700°C, which showed ~1.2 times improvement in H_2/CO_2 selectivity from 30.8 to 36.9, as the permeation temperature was increased from 25°C to 110°C. Generally, higher operating temperature activates the diffusion of H_2 and CO_2, while simultaneously limiting CO_2 sorption. Therefore, E_P for H_2 is larger compared to E_P for CO_2 due to large negative heat of sorption (ΔH_s, kJ/mol) value of the highly condensable CO_2 compared to H_2, which has a dominating effect over diffusion activation energy (E_D, kJ/mol) of CO_2.[7] Hence, H_2 experiences a larger increase in permeability compared to CO_2 due to reduced CO_2 sorption at higher temperature thereby mitigating the competitive sorption effects of CO_2 on the H_2/CO_2 separation factor at elevated temperatures. However, the higher E_P for CO_2 compared to E_P for H_2 in MTI-1050 could presumably be due to a largely positive E_D for CO_2 having a dominating effect over the ΔH_s for CO_2, due to the extremely refined CMS ultramicropores in MTI-1050, leading to larger increase in CO_2 permeability as

compared to H_2 at higher temperatures, hence decreasing the H_2/CO_2 separation factor at higher temperatures.

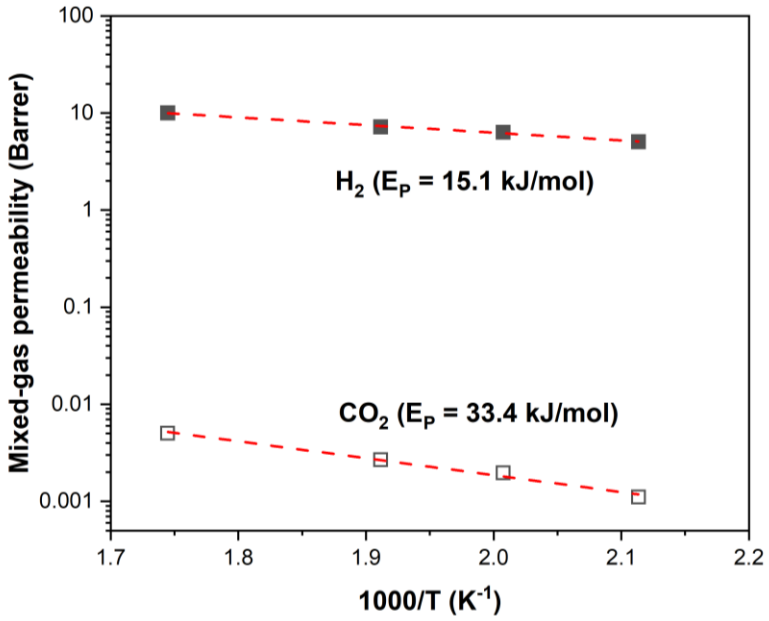

Figure 5.3: Arrhenius plots of H_2 and CO_2 permeabilities in the MTI-1050 CMS membrane. E_P is the permeation activation energy (kJ/mol).

Although the H_2/CO_2 separation factor of the MTI-1050 CMS membrane dropped at higher temperatures, it remained exceptionally attractive above 1900. To the best of our knowledge, the MTI-1050 CMS membrane shows the highest H_2/CO_2 separation factor far exceeding other CMS membranes reported in literature (Figure 5.4 and Table 4.7). The MTI-1050 had more than one order of magnitude higher H_2/CO_2 separation factor than the CMS membrane derived from CANAL ladder polymer at 900°C [50], which had the highest H_2/CO_2 separation factor (256) prior to this work. Notably, the exceptionally high H_2/CO_2 separation factor in the MTI-1050 CMS membrane was obtained without significant compromise in H_2 permeability. In

fact, the MTI-1050 CMS membrane shows competitive H_2 mixed gas permeability among other CMS membranes reported in literature.[10, 11, 41, 50, 132]

Table 5.2: Comparing the mixed-gas H_2/CO_2 separation performance of MTI-1050 with CMS membranes reported in literature.

Precursor	$T_{pyrolysis}$ (°C)	P (H_2) (Barrer)	α (H_2/CO_2)	$T_{permeation}$ (°C)	P_{feed} (bar)	Membrane geometry
PBI[10]	900	39	53	100	10	Film
PBI/PPA[11]	600	116	33	150	6.5	Film
Cellulose[41]	700	225	31	90	10	Hollow fiber
CANAL[50]	900	8.2	174	100	10	Film
CANAL[50]	900	9.8	256	100	2	Film
MTI[132]	925	3.5	156	35	2	Hollow fiber
MTI	1050	5.1	4565	200	2	Hollow fiber
MTI	1050	6.3	3226	225	2	Hollow fiber
MTI	1050	7.2	2677	250	2	Hollow fiber
MTI	1050	10.0	1988	300	2	Hollow fiber

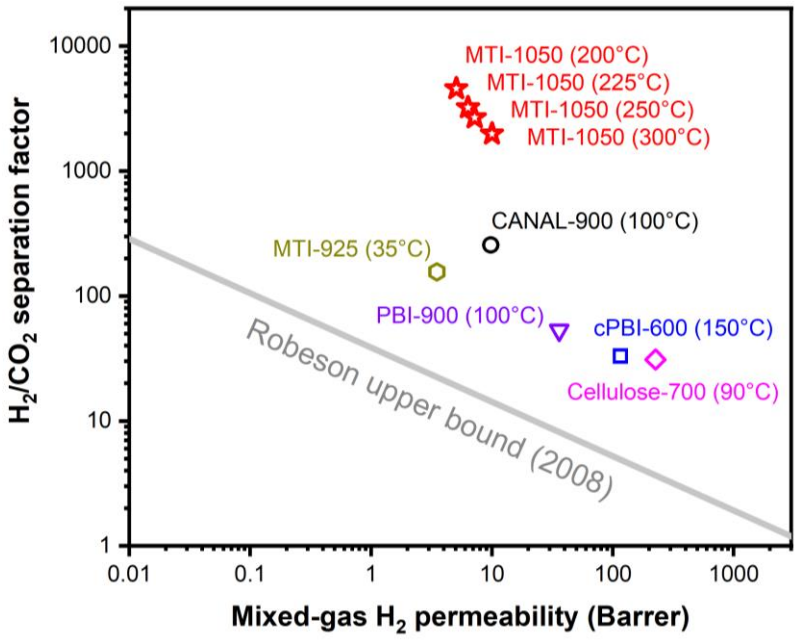

Figure 5.4: Comparing the mixed-gas H_2/CO_2 separation performance of MTI-1050 with CMS membranes reported in literature.

5.2.3 Long-term stability test

Commercial gas separation membranes are expected to last for 3-5 years. The long-term stability of membrane separation performance is therefore crucial to commercialization of new membrane materials. The long-term stability of H_2 permeability and H_2/CO_2 separation factors of the MTI-1050 CMS hollow fiber membrane was studied using the constant-volume permeation method with a 10 mol% H_2/90 mol% CO_2 feed mixture at 2 bar and 250°C (Figure 5.5). Following an initial transient phase of 5 days, the membrane showed highly stable H_2 permeability and H_2/CO_2 separation factors for 15 days. Aging-induced permeability loss in CMS membranes has been previously reported in literature, as the carbonaceous strands in the CMS rearrange to achieve a more thermodynamically stable state.[87] The MTI-1050 showed remarkable aging resistance without exhibiting any drop in mixed-gas permeabilities over time. The aging resistance was possibly due to the extremely large extent of CMS pore structure compaction and ultramicropore refinement in the MTI-1050, which reduced the possibility of further rearrangement of the CMS strands. Loss in gas permeability has been previously reported under high temperature operation because of coke deposition and consequent ultramicropore refining. For example, Liu and co-workers[116] showed reductions in H_2 and C_3H_8 permeances in a polyimide-derived CMS hollow fiber membranes with an increase in H_2/C_3H_8 separation factor following 25 hours under H_2/C_3H_8 mixture permeation at 600°C. Because the long-term stability test shown in Figure 5.5 was conducted under milder conditions without coke precursors, coke-induced ultramicropore refining possibly did not occur.

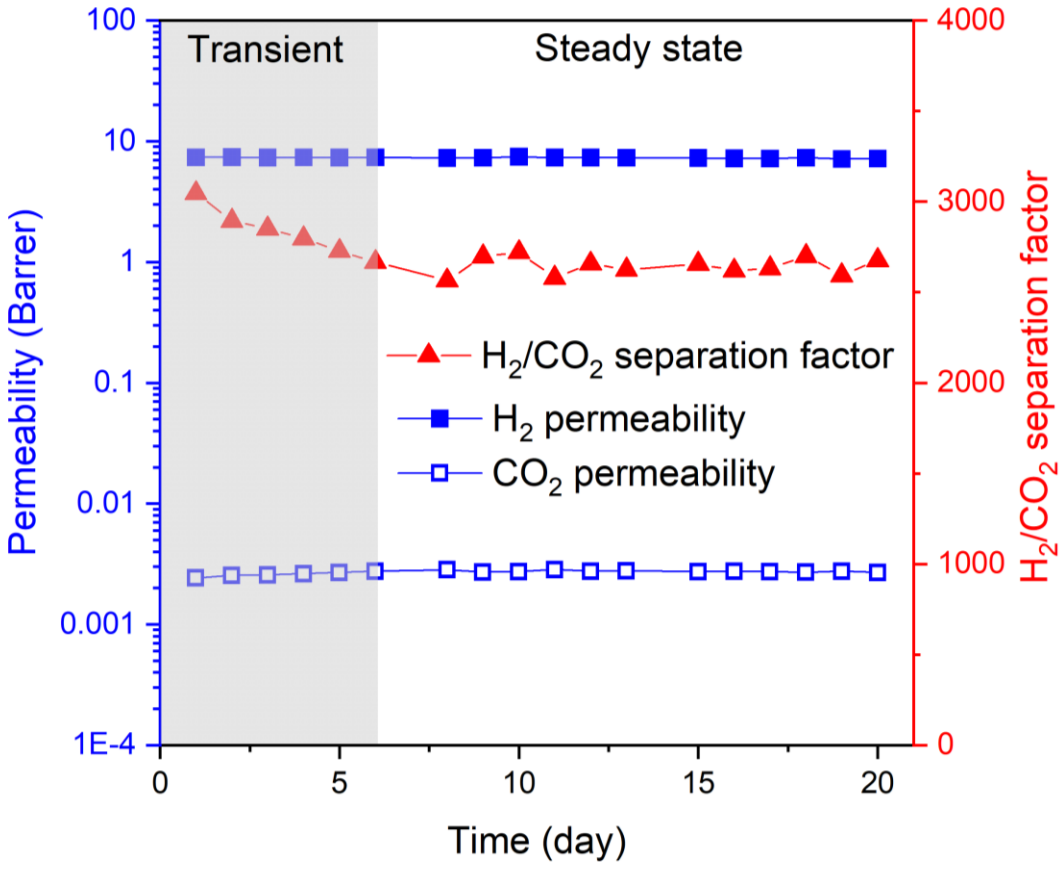

Figure 5.5: Long-term stability of H_2/CO_2 separation performance in the MTI-1050 CMS membrane at 250°C using 10% H_2/90% CO_2 feed mixture at 2 bar.

5.3 Pore structure characterization

In Chapter 4, we showed that CMS membranes made using higher pyrolysis temperatures exhibit highly refined ultramicropores due to increased CMS membrane pore structure compaction. Hence, polyaramid-derived CMS membrane at 1050°C (MTI-1050) could possibly have more refined ultramicropores compared to the polyaramid-derived CMS membrane at 925°C (MTI-925), which leads to the unprecedentedly high H_2/CO_2 mixed-gas separation factor > 1900 in the MTI-1050. Characterization of the CMS membrane pore structure will explain the ultra-high

H_2/CO_2 separation performance of the MTI-1050. The polyaramid-derived CMS dense films (MTI-1050) were characterized using H_2 porosimetry, XPS and Raman spectroscopy.

In chapter 4, the conventional CO_2 physisorption method for pore size distribution measurement was unable to characterize the highly refined ultramicropores which are < 4Å in the polyaramid-derived CMS membrane. Therefore, for a more robust pore size distribution analysis, we measured H_2 physisorption isotherms at 77K as a novel approach to obtain the pore size distribution in the CMS membrane. H_2 physisorption at 77K has been previously used to study pore size distribution in activated carbons.[133] To the best of our knowledge, this technique has not been used to characterize the pore size distribution in CMS membranes. Hence, physisorption of H_2 at 77K was used to compare the CMS membrane pore structure of MTI-1050 with MTI-925. The H_2 sorption isotherms at 77K were fitted with a 2D-NLDFT model (HS-2D-NLDFT, carbon, H_2, 77K) to obtain the pore size distribution curves and cumulative pore volume (Figure 5.6).[133] Both MTI-1050 and MTI-925 show bimodal pore size distribution with two peaks, a first peak at ~ 3Å and a second peak at ~ 7Å. While both MTI-1050 and MTI-925 showed similar pore size at the first peak, the MTI-1050 showed smaller pore size at the second peak. The smaller pore size at the second peak was possibly responsible for enhanced CO_2 exclusion and higher H_2/CO_2 separation factor in the MTI-1050 CMS membrane. Additionally, MTI-1050 had a significantly lower pore volume compared to MTI-925, further indicating a more compact pore structure of MTI-1050. To our best knowledge, this was the first time

that H_2 physisorption at 77K is used to characterize the pore structure of CMS membranes.

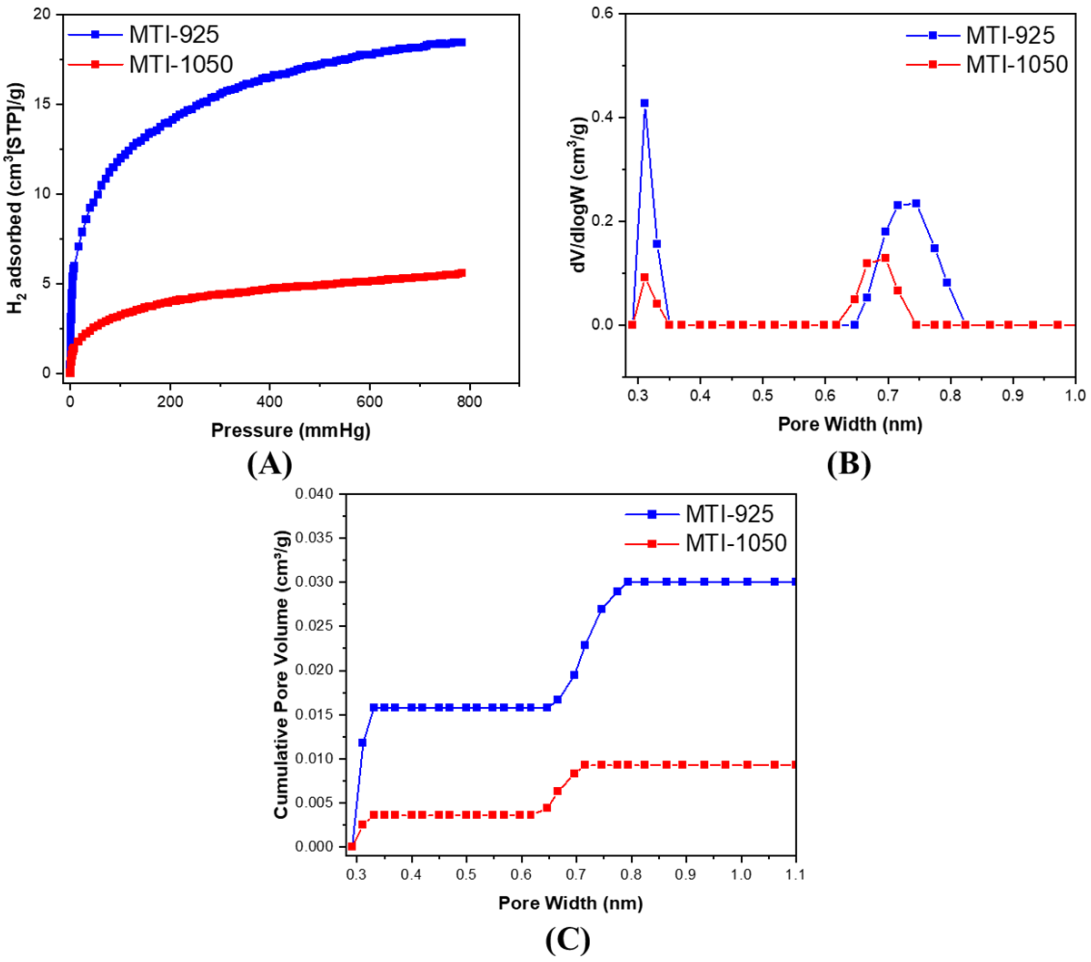

Figure 5.6: (A) H_2 sorption isotherms (77 K), (B) CMS pore size distribution and (C) Cumulative pore volume (cm^3/g) measured using H_2 physisorption at 77K.

To complement the pore size distribution, high resolution XPS C1s spectra (Figure 5.7) were compared for the MTI-1050 and MTI-925. Table 5.3 shows the elemental compositions of MTI-925 and MTI-1050. With increase in pyrolysis temperature, the concentration of N and O heteroatoms is reduced, as the CMS pore structure and more short-range ordered graphitic structures are formed. The presence

of oxygen functionalities is possibly due to oxygen chemisorption from the atmosphere. These observations are consistent with previous reports in literature.[50] The high resolution C1s spectra can be used to determine the ratio of sp^3/sp^2 carbon in the CMS membranes.[64] The sp^3/sp^2 carbon ratio is indicative of the level of disorder in the amorphous graphitic structure of the CMS membranes, i.e., smaller sp^3/sp^2 carbon ratio suggests a more ordered graphitic structure and hence smaller CMS membrane inter-plate spacing and ultramicropore size. The results show that MTI-1050 has a smaller sp^3/sp^2 carbon ratio and hence a more ordered graphitic structure as compared to MTI-925.

Table 5.3: Elemental composition of MTI-925 and MTI-1050 CMS membranes measured using XPS.

Element	Atomic %	
	MTI-925	**MTI-1050**
Carbon	95.37	97.55
Nitrogen	1.75	0.34
Oxygen	2.88	2.12

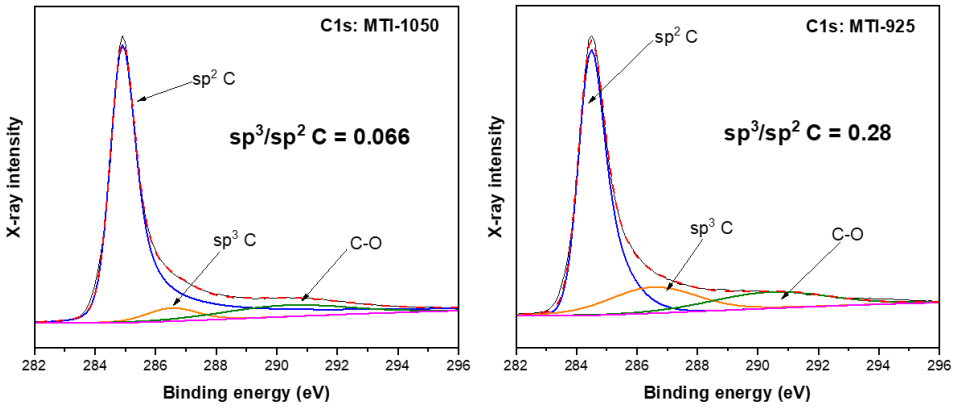

Figure 5.7: High resolution XPS C1s spectra for (A) MTI-1050 and (B) MTI-925 showing sp^3/sp^2 carbon ratio.

To complement the XPS analysis, we carried out Raman spectroscopy (Figure 5.8) to further compare the CMS membrane pore structure of MTI-1050 and MTI-925. Two characteristic bands commonly observed for amorphous carbonaceous materials – the D band (~1350 cm^{-1}) and G band (~1590 cm^{-1}) were seen in the Raman spectra of all three CMS membranes. The D band was related to the A_{1g}-symmetry vibrational mode of structural defects, indicating presence of disorder in the carbon structure. The G band was related to the E_{2g}-symmetry mode of the aromatic sp^2-carbon and linear chains corresponding to C=C in-plane stretching in graphitic carbon materials. With increasing degree of disorder and presence of oxygenated functionalities, secondary peaks appear in the D band. Therefore, each Raman spectrum was decoupled using 5 Gaussian peaks – D1, D2, D3, D4, G to fit the experimental data. The D1 peak (~1350 cm^{-1}) was associated with the basal plane defects in the graphitic structure.[98] The I_{D1}/I_G ratio can be used as a measure of the concentration of sp^2 carbon, i.e., lower I_{D1}/I_G ratio indicates higher concentration of sp^2 carbon and smaller ultramicropores. The lower I_{D1}/I_G ratio of MTI-1050 indicates a more ordered graphitic structure as compared to MTI-925, which is in good agreement with the XPS results.

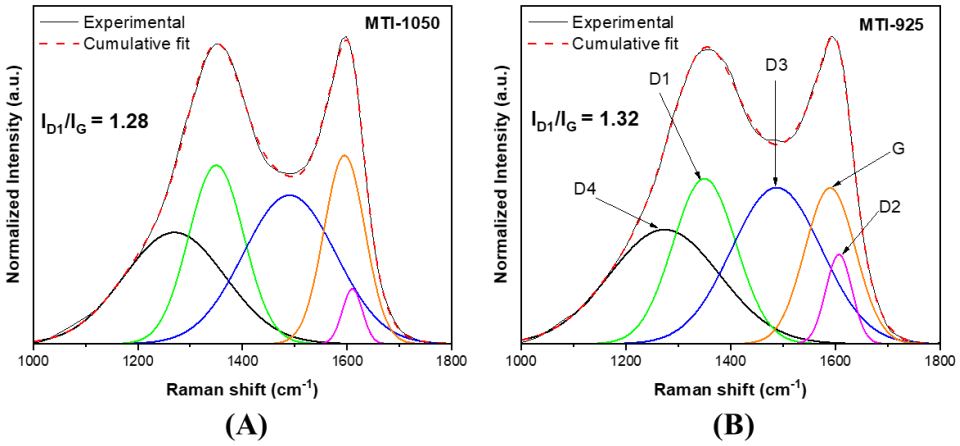

Figure 5.8: Raman spectra of (A) MTI-1050 and (B) MTI-925 showing I_{D1}/I_G ratios.

5.4 Modelling CMS hollow fiber membrane separators for H_2/CO_2 separation

A one-dimensional isothermal model was used to simulate a co-current membrane separator comprising MTI-1050 CMS hollow fiber membranes. The following assumptions were applied to the model.[134]

- The ideal gas equation of state is valid for the gas mixture at the feed and permeate conditions.
- There is negligible pressure drop on the shell side and the bore side of the hollow fiber membrane.
- Local Joule-Thomson effect due to gas permeation is ignored, the system is assumed to be at isothermal conditions.
- Gas flows in the feed and permeate side are assumed to be in plug flow; radial distribution is ignored.

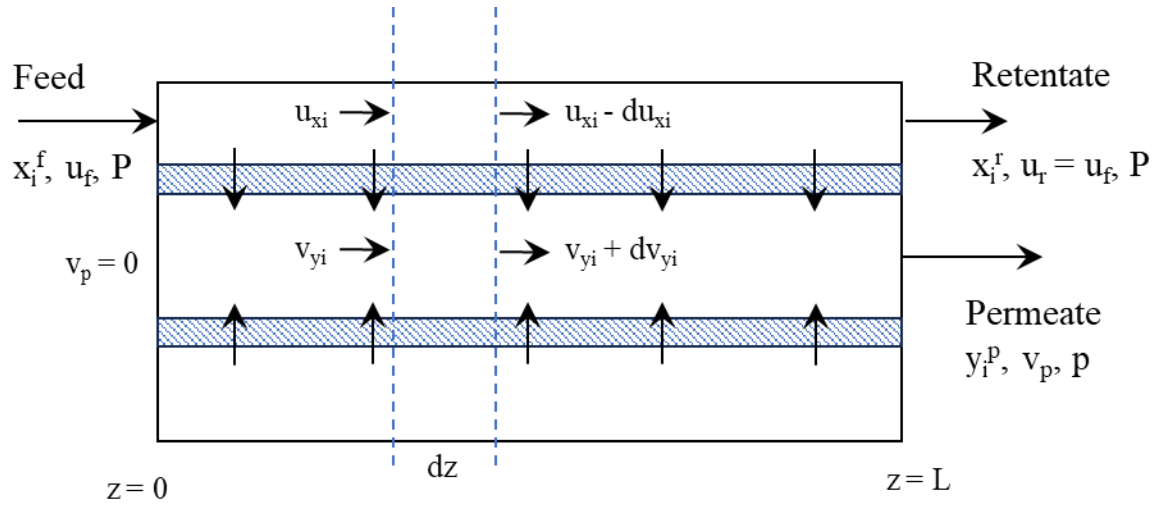

Figure 5.9: Schematic of material balance across a differential element *dz* in a co-current hollow fiber membrane separator model.

Permeation of a multicomponent gas mixture through a hollow fiber membrane module in co-current flow with shell-side feed is considered, with the permeate flowing in the positive *z*-direction. The component flow rates in the feed and the permeate through a differential membrane element *dz* at length *z* can be described using a system of ordinary differential equations obtained from material balance across the differential element *dz* as follows.[134] Figure 5.9 shows a schematic of a differential element in a co-current hollow fiber membrane separator.

Feed side material balance equation

$$\frac{d(u_{xi})}{dz} = -\pi D_0 N Q_i (P x_i - p y_i) \tag{5.1}$$

Permeate side material balance equation

$$\frac{d(v_{yi})}{dz} = \pi D_0 N Q_i (P x_i - p y_i) \tag{5.2}$$

$$u_f = \sum_{i=1}^{n_c} u_{xi} \tag{5.3}$$

$$v_p = \sum_{i=1}^{n_c} v_{yi} \tag{5.4}$$

$$\sum_{i=1}^{n_c} x_i = 1 \tag{5.5}$$

$$\sum_{i=1}^{n_c} y_i = 1 \tag{5.6}$$

where u_{xi} (mol/s) and v_{yi} (mol/s) are the molar flow rate of component *i* in the feed side and permeate side, u_f (mol/s) and v_p (mol/s) are the total molar flow rates in the feed side and permeate side, x_i (mol/mol) and y_i (mol/mol) are the mole fractions of component *i* in the feed side and permeate side, D_0 (μm) is the outer diameter of the hollow fiber, *N* is the number of fibers packed in the membrane module, Q_i (GPU) is the permeance of component *i* through the membrane, *P* (Pa) is the feed pressure, and *p* (Pa) is the permeate pressure. The initial condition for the feed side material balance equation is u_{xi} ($z = 0$) = u_{fi}, where u_{fi} is the feed flow rate of component *i*. The initial condition for the permeate side material balance equation is v_{yi} ($z = 0$) = 0. Simulating H_2/CO_2 separation with a binary mixture of H_2 and CO_2 as feed involves numerically solving a system of four ordinary differential equations. The model was programmed in Python as an initial value problem using the odeint function from scipy, which follows the Livermore Solver for Ordinary Differential Equations (LSODA) algorithm, developed by Lawrence Livermore National Laboratory to numerically solve system of ordinary differential equations.

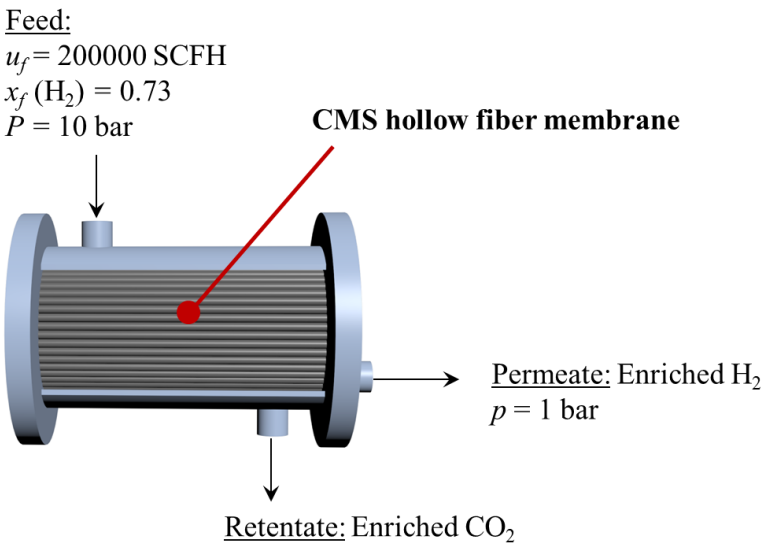

Figure 5.10: Schematic of a CMS hollow fiber membrane separator with specified feed and permeate conditions used for simulation.

A schematic of the CMS hollow fiber membrane separator is shown in Figure 5.10. The retentate stream is enriched in CO_2 and will be sequestered or sent to CO_2 conversion reactors. The permeate stream is enriched in H_2 and is the product stream of the separation. H_2 recovery (%) in the permeate stream and CO_2 recovery (%) in the retentate stream are defined as

$$H_2\ recovery\ (\%) = \frac{Molar\ flow\ rate\ of\ H_2\ in\ permeate}{Molar\ flow\ rate\ of\ H_2\ in\ feed} \times 100 \qquad (5.7)$$

$$CO_2\ recovery\ (\%) = \frac{Molar\ flow\ rate\ of\ CO_2\ in\ retentate}{Molar\ flow\ rate\ of\ CO_2\ in\ feed} \times 100 \qquad (5.8)$$

The % purity of H_2 in the product stream (permeate) was simulated for different recoveries of H_2 in the product stream. In addition to the MTI-1050 CMS membrane, the CANAL-900[50] and PBI/PPA-600[11] CMS membranes were also considered for the simulation. The feed (10 bar) is a binary H_2 (73 mol%)/CO_2 (27 mol%) mixture and

permeate is at 1 bar. Additional input parameters for the three membrane separators are given in Table 5.4. The permeance (GPU) was evaluated assuming 1 μm membrane thickness.

Table 5.4: Model input parameters.

Parameter	Membrane separator		
	MTI-1050	**CANAL-900**	**PBI/PPA-600**
H_2 permeance (GPU)	7.2	8.2	116
Separation factor	2677	174	33

The simulation results are shown in Figure 5.11, in which H_2 purity (%) in the product stream was calculated for H_2 recovery (%) ranging from 10% to 90%. Table 5.5 shows the simulation results for H_2 purity (%) in permeate, CO_2 purity (%) in retentate and CO_2 recovery (%) in the retentate for 90% H_2 recovery from the three membrane separators. The results clearly show that the MTI-1050 CMS membrane outperforms the CANAL-900 CMS membrane and PBI/PPA-600 CMS membrane for production of purer H_2. With 90% H_2 recovery, the MTI-1050 membrane separator can provide highly pure H_2 product of 99.95%. Owing to much lower H_2/CO_2 separation factors, the CANAL-900 and PBI/PPA-600 membrane separators can only produce 99.28% and 96.54% H_2 products. For blue H_2 production, efficient H_2 separation with simultaneous CO_2 capture is required from the downstream purification process. Using a membrane separator, production of an enriched H_2 product stream in the permeate needs to be accompanied by simultaneous production of an enriched CO_2 stream in the retentate. The simulation results show that with 90% H_2 recovery in the permeate, the MTI-1050 membrane separator produces an enriched CO_2 retentate stream with the highest CO_2 purity of 78.79% and the highest CO_2 recovery of 99.88% among the three

membrane separators, owing to its highest H_2/CO_2 separation factor. In comparison, the CANAL-900 and PBI/PPA-600 membrane separators can produce retentate streams with lower CO_2 purities of 78.55% and 77.12% respectively, along with lower CO_2 recoveries of 98.24% and 91.27% respectively.

Table 5.5: Summary of simulation results for CMS hollow fiber membrane separators. All simulations were performed for 90% H_2 recovery in permeate.

Parameter	Membrane separator		
	MTI-1050	**CANAL-900**	**PBI/PPA-600**
H_2 purity (%) in permeate	99.95	99.28	96.53
CO_2 purity (%) in retentate	78.79	78.55	77.12
CO_2 recovery (%) in retentate	99.88	98.24	91.27

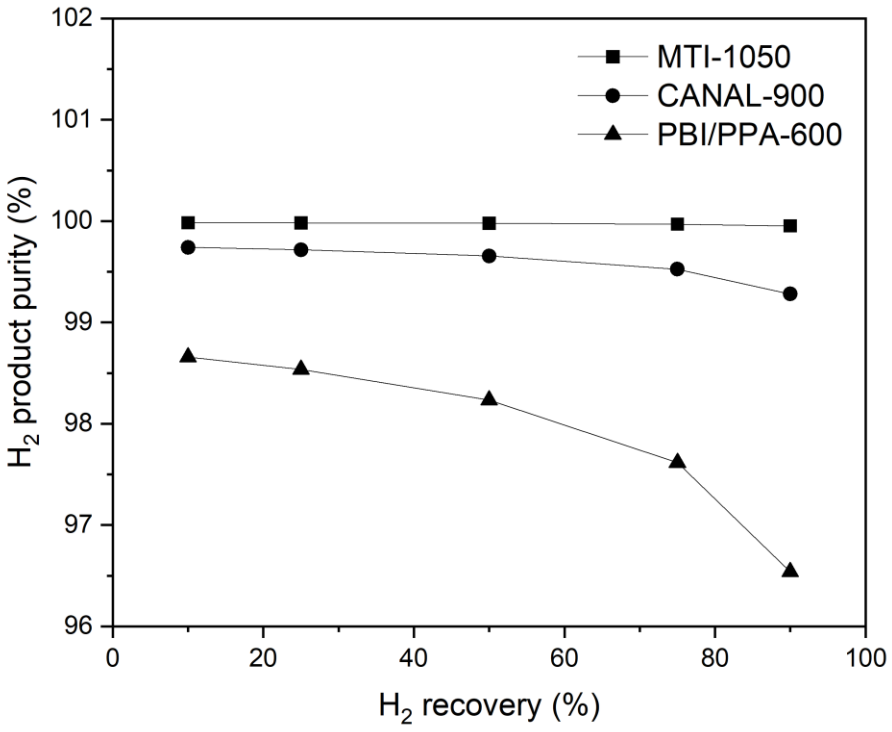

Figure 5.11: Simulation results showing H_2 product purity (%) under different H_2 recovery (%) of CMS hollow fiber membrane separators consisting of different CMS hollow fiber membranes.

Chapter 6: Understanding the role of precursor amide moiety in CMS membrane structure-transport property relationship

The research described in this chapter is published in: Iyer, G. M.; Ku, C.E.; Zhang, C., Polyamide-imide copolymer-derived carbon molecular sieve membranes for efficient hydrogen/carbon dioxide separation. *Carbon* **2024,** *216,* 118598.

6.1 Overview

Separation of H_2 from CO_2 can recover H_2 and capture CO_2 from steam methane reforming products. In chapter 4, we demonstrated ultra-high H_2/CO_2 ideal selectivity (up to 366) in a polyaramid-derived CMS membrane with H_2 permeability of 9 Barrer.[132] The remarkable H_2/CO_2 selectivity in the polyaramid-derived CMS membrane was attributed to the formation of refined "H_2-selective micropores" by ultramicropore tightening in the CMS membrane formed at a pyrolysis temperature of 925°C. However, systematically studying the structure-property relationship between the polymer precursor chemistry and the resulting CMS membrane's structure and transport properties is essential to develop a fundamental understanding of the formation of these "H_2-selective micropores" in the polyaramid-derived CMS membrane. This can provide a valuable benchmark for tuning the polymer precursor chemistry to achieve CMS membranes demonstrating highly attractive H_2/CO_2 separation performance and effectively guide the design of CMS membranes for efficient H_2/CO_2 separation and sustainable blue H_2 production.

Polyimides (PIs) represent the most widely studied class of CMS membrane precursors. Several studies in the past decade have shown that PI-derived CMS membranes demonstrate highly tunable pore structures providing attractive separation performance for several gas pairs such as CO_2/CH_4, H_2/CH_4 and C_2H_4/C_2H_6. However, PI-derived CMS membranes demonstrate unattractive H_2/CO_2 separation performance. Comparing the chemistries of the polyaramid and polyimide precursors, we believe that the presence of amide moieties in the polyaramid backbone which are absent in the polyimide backbone, plays a vital role in achieving the highly attractive H_2/CO_2 separation performance in the polyaramid-derived CMS membranes.

Additionally, copolymer membranes are often made to provide balanced and sometimes synergistic separation performance unattainable in homopolymer membranes.[135, 136] Polyamide-imides (PAIs) are copolymers consisting of both imide and amide backbones. PAIs can provide CMS membranes with properties affected by mixed imide and amide backbone chemistries of the copolymeric precursor, hence providing a valuable aid to study the structure-property relationship in polyaramid-derived CMS membranes. To our best knowledge, no CMS hollow fiber membranes have been derived from PAIs. Also, attractive gas separation performance has not been reported from PAI-derived CMS membranes.

In this chapter, we present a comprehensive study of the effect of amide moieties in the polymer precursor backbone on the pore structure and gas transport properties of the CMS membranes derived thereof. We fabricated PAI-derived CMS hollow fiber membranes and PI-derived CMS hollow fiber membranes by pyrolysis of defect-free Torlon® precursor hollow fiber membranes and defect-free Matrimid®

precursor hollow fiber membranes, respectively at 925°C. The PAI-derived CMS membrane showed balanced H_2 permeability and H_2/CO_2 selectivity between the CMS membranes made from the MTI polyaramid and the Matrimid® polyimide at identical pyrolysis conditions. Sorption, diffusion, and pore structure characteristics of the PI-derived CMS, PAI-derived CMS and PA-derived CMS hollow fiber membranes were compared to gain an understanding on how precursor backbone chemistry affects CMS membrane pore structure and transport properties. The results provide evidence for the contribution of precursor amide moiety in providing attractive H_2/CO_2 separation performance in the polyaramid-derived CMS membrane.

Section 6.2 highlights the differences in the properties of Matrimid® polyimide, Torlon® polyamide-imide, and MTI polyaramid arising due to differences in the polymer backbone chemistry, and the formation of CMS hollow fiber membranes from Matrimid® polyimide and Torlon® polyamide-imide used to compare with MTI polyaramid-derived CMS membranes in this study. Section 6.3 discusses the comparison of gas separation performance of CMS membranes derived from Matrimid® polyimide, Torlon® polyamide-imide, and MTI polyaramid precursors at identical pyrolysis conditions at 925°C. Section 6.4 provides a systematic comparison of gas sorption and diffusion properties of CMS membranes derived from the different polymer precursors. Section 6.5 shows the characterization studies performed on CMS membranes derived from the different polymer precursors. Finally, section 6.6 explains the effect of precursor amide moiety on the structure-property relationship in the CMS membranes, using the supporting evidence provided by the results in this chapter. The structure-transport property relationship in the polyaramid-derived CMS membranes is

emphasized to interpret the gas separation performance of the polyaramid-derived CMS membranes.

6.2 Fabrication of CMS membranes derived from polyaramid, polyamide-imide, and polyimide precursors

6.2.1 Characterization of polyaramid, polyamide-imide and polyimide precursors

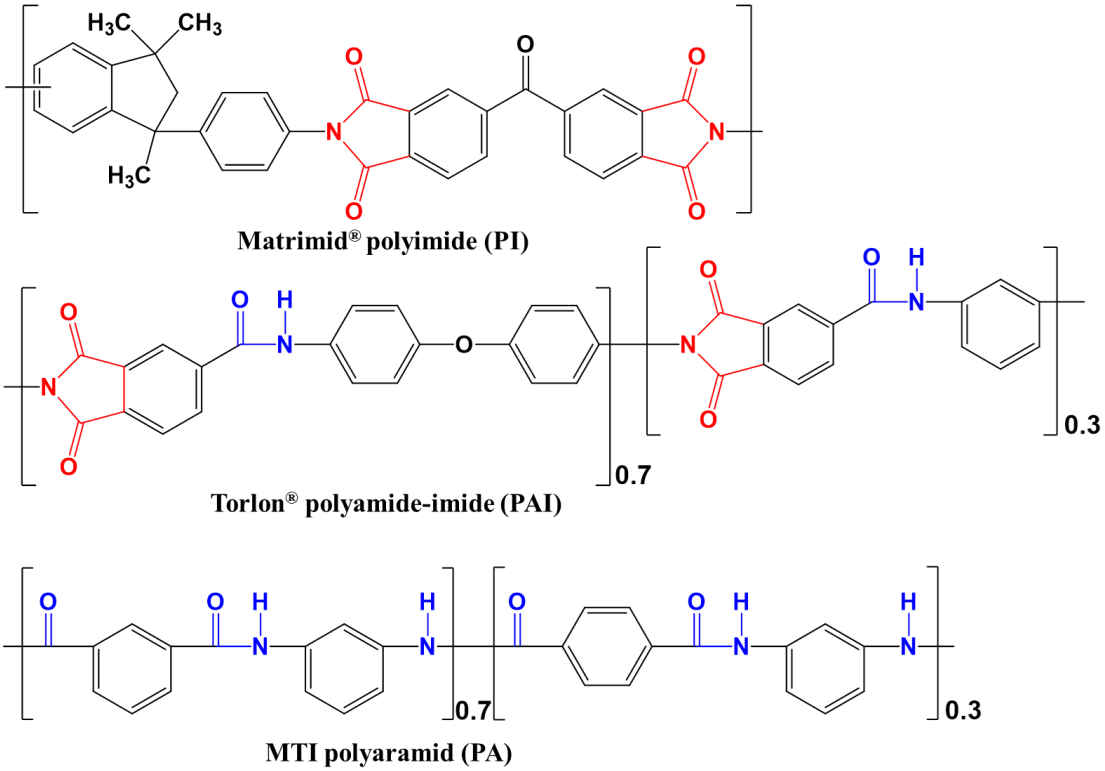

Figure 6.1: Chemical structure of polyimide, polyamide-imide and polyaramid precursors highlighting the imide and amide groups in the polymer backbone.

Torlon® polyamide-imide (PAI), MTI polyaramid (PA) and Matrimid® polyimide (PI) were used as the CMS membrane precursors (Figure 6.1). These polymers are all uncrosslinked linear polymers with rigid aromatic backbones and without bulky side groups. Figure 6.2 shows the FT-IR spectra of the Matrimid®

polyimide, Torlon® polyamide-imide, and MTI polyaramid. The characteristic IR stretching peak at ~3300 cm^{-1} corresponding to hydrogen-bonded N-H stretching vibration is the strongest in PA, relatively weaker in the PAI, and absent in the PI.[113] Additionally, absence of the characteristic peak at ~3446 cm^{-1} (free N-H stretching vibrations) indicates that all N-H groups are hydrogen-bonded in the polyaramid and polyamide-imide precursors.[137]

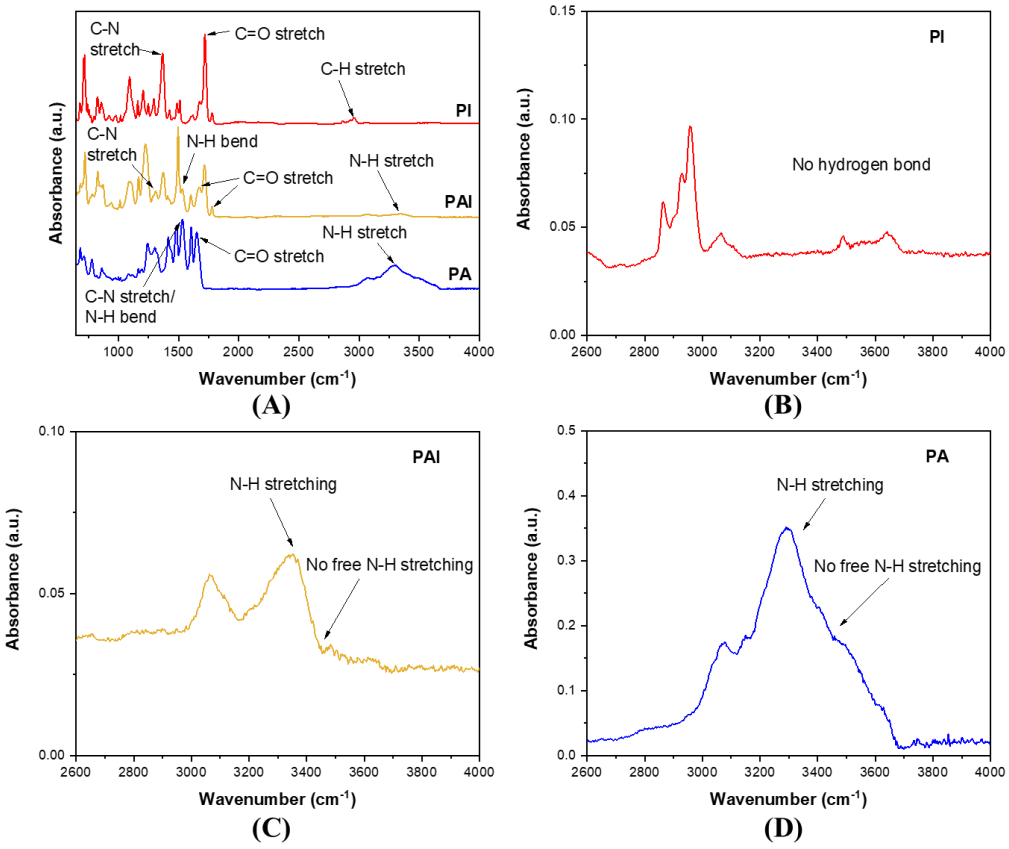

Figure 6.2: (A) FTIR spectra of polymer precursors indicating characteristic peaks; High-resolution FTIR spectrum for (B) the polyimide showing absence of N-H stretching vibration; (C) the polyamide-imide showing weak N-H stretching vibrations; (D) the polyararmid showing strong N-H stretching vibrations.

Figure 6.3 shows the TGA weight loss profiles for the Matrimid® polyimide, Torlon® polyamide-imide, and MTI polyaramid. The trend in thermal decomposition

temperature of the polymeric precursors was as follows: PA: 400 °C < PAI: 420 °C < PI: 475 °C. The Matrimid® polyimide, Torlon® polyamide-imide, and MTI polyaramid had comparable carbon residue (~50-55 %) at 950°C. Figure 6.4 shows the WAXD spectra for the Matrimid® polyimide, Torlon® polyamide-imide, and MTI polyaramid. Comprising both imide and amide backbones, the polyamide-imide showed intermediate d-spacing (PA: 3.86 Å; PAI: 4.31 Å; PI: 6.22 Å), density (PA: 1.37 g/cm^3; PAI: 1.36 g/cm^3; PI: 1.25 g/cm^3[115]), and FFV (PA: 0.057[132]; PAI: 0.084[138]; PI: 0.110[115]) compared to the Matrimid® polyimide and MTI polyaramid.

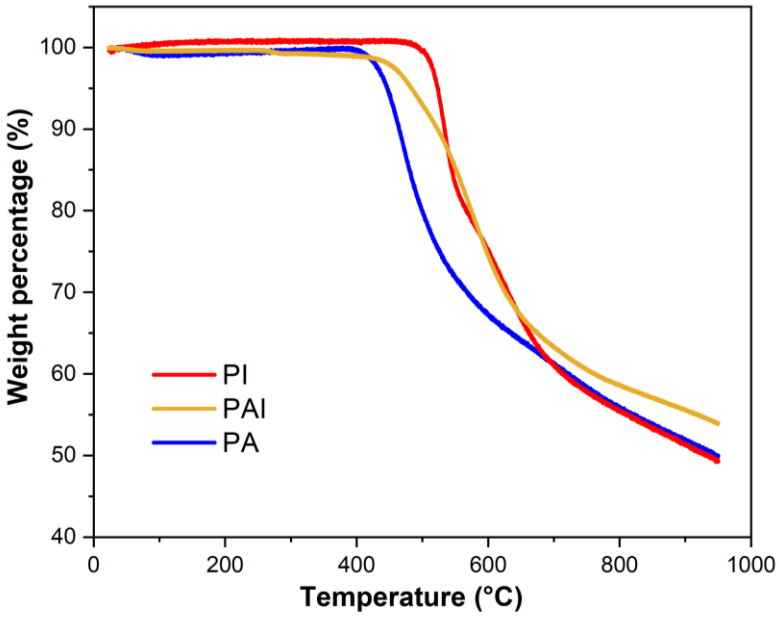

Figure 6.3: TGA weight loss profiles of polymer precursors up to 950°C (N_2 purge).

A strong correlation between the precursor hydrogen bonding strength and polymer properties (d-spacing, FFV, and density) of the polymer precursors can be seen from these results. While moieties other than amide or imide can be found in the polymer backbones (e.g., ketone in the PI and ether in the PAI), it was apparent that

the precursor polymer properties were strongly affected by hydrogen bonding. With strong hydrogen bonding provided by the highly concentrated amide moieties, the PA had closely packed chains giving the smallest d-spacing and FFV and largest density. Without amide moiety and hydrogen bonding, the PI precursor had the least closely packed chains giving the largest d-spacing and FFV and the smallest density. With mixed amide and imide backbone chemistry and weaker hydrogen bonding, the PAI precursor had intermediate d-spacing, FFV, and density.

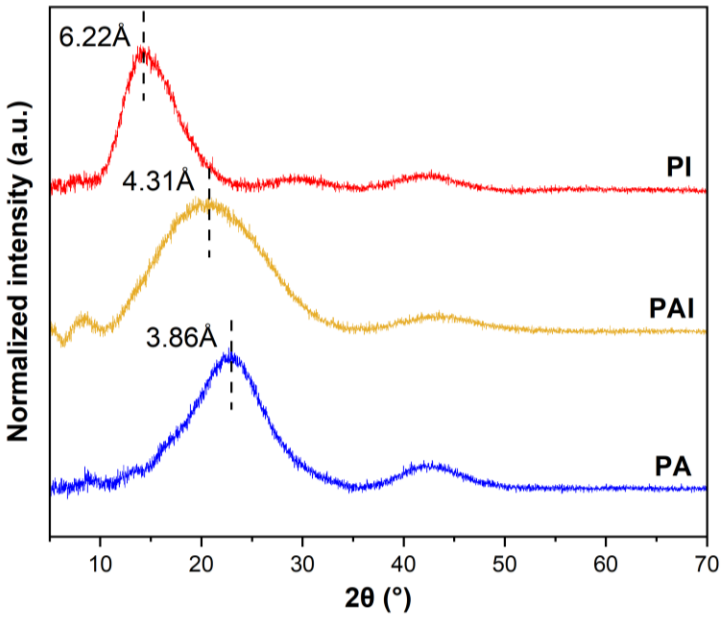

Figure 6.4: WAXD spectra of polymer precursors indicating d-spacing.

6.2.2 Fabrication of Monolithic Matrimid®-derived CMS hollow fiber membranes

Monolithic Matrimid® polyimide precursor hollow fiber membranes were fabricated using the dry-jet/wet-quench spinning process using the polymer dope composition and spinning conditions shown in Table 6.1, as reported in Liu et al. 2021. [116]Figure 6.5A shows a photo of the PI precursor hollow fiber bundle. Figure 6.5(B-

C) shows the SEM images of the PI precursor hollow fiber. SEM shows that the PI precursor hollow fibers (outer diameter ~ 435 μm) exhibited an asymmetric structure with a porous substrate having large and interconnected pores and a dense skin layer on the outer surface. The PI precursor hollow fiber membranes showed He permeance of 45 GPU and He/N_2 ideal selectivity of 72 under single gas He/N_2 permeation at room temperature. The He/N_2 ideal selectivity was within 90% of the intrinsic value measured in thick Matrimid® dense films[52], indicating that the PI precursor hollow fiber membranes were defect-free.

Table 6.1: Polymer dope composition and hollow fiber spinning conditions for fabrication of Matrimid® polyimide precursor hollow fiber membranes. [116]

Spinning Conditions	Unit	Value
Dope composition	wt% Matrimid®	26.2
	wt% NMP	53.0
	wt% THF	5.9
	wt% Ethanol	14.9
Spinning temperature	°C	60
Lab relative humidity	%	10
Quench bath temperature	°C	50
Dope/bore fluid flow rate	cm^3/h	180/60
Bore fluid composition	NMP/H_2O	90/10
Air gap height	cm	10
Fiber take-up rate	m/min	20

PI-derived CMS hollow fiber membranes were successfully made by pyrolysis of the defect-free Matrimid® PI precursor hollow fiber membranes at 925°C under continuous argon purge. Figure 6.5(D-E) shows the SEM images of the PI-derived CMS hollow fiber. Without pre-treatments, pore collapse and wall densification are known to occur in precursor hollow fibers during pyrolysis.[126] The PI precursor

hollow fibers underwent pore collapse during pyrolysis and hence the PI-derived CMS hollow fiber membranes (outer diameter ~ 225 μm) had totally densified wall of 40 μm. The totally densified wall allowed for unambiguous determination of the CMS membrane's separation layer thickness (40 μm).

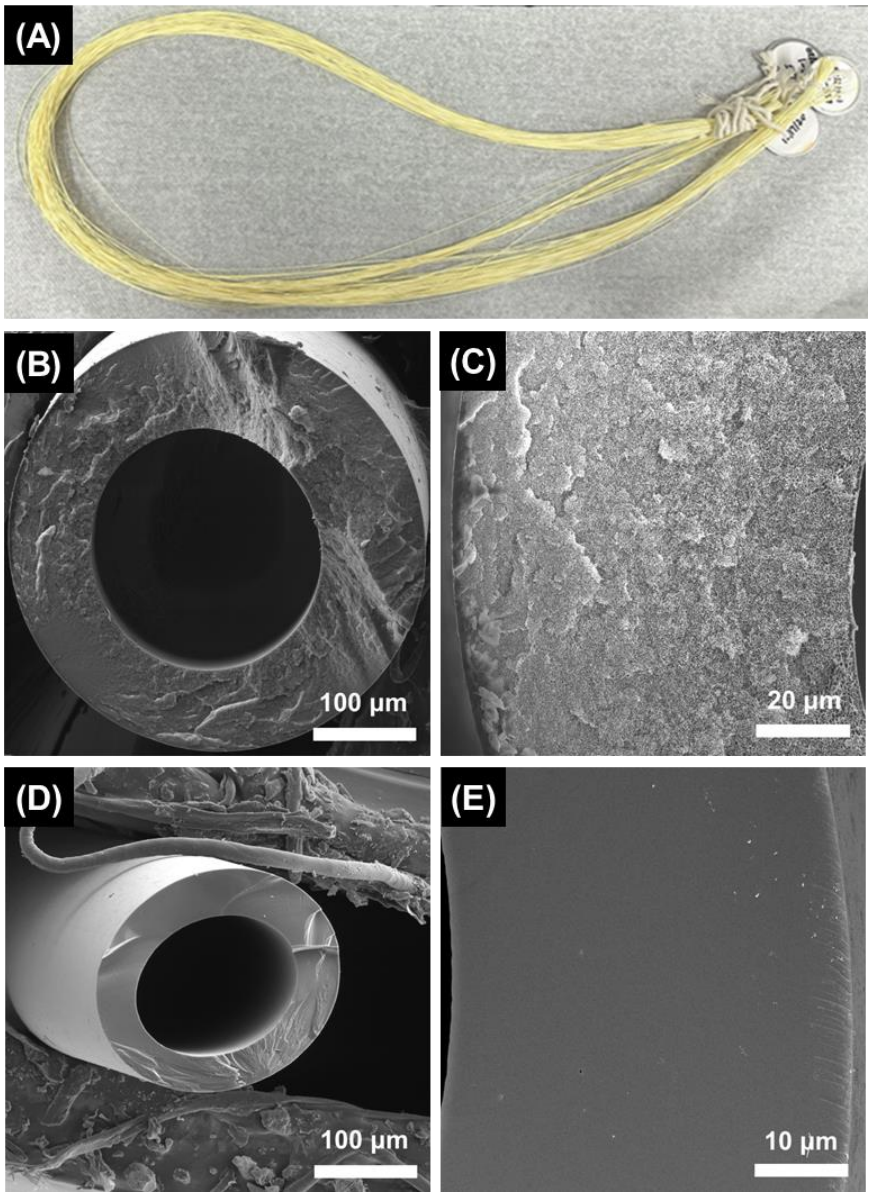

Figure 6.5: (A) Photo of the Matrimid® PI precursor hollow fiber bundle; SEM images of defect-free Matrimid® PI precursor hollow fiber membranes and PI-derived CMS hollow fiber membranes. (B) Precursor hollow fiber overview; (C) Precursor hollow fiber wall; (D) CMS hollow overview; (E) CMS hollow fiber wall.

6.2.3 Fabrication of Monolithic Torlon®-derived CMS hollow fiber membranes

Monolithic Torlon® PAI precursor hollow fiber membranes were fabricated using the dry-jet/wet-quench spinning process based on spinning dope composition and spinning parameters indicated in Table 6.2, identified by Kosuri and Koros.[137] Figure 6.6A shows a photo of the PAI precursor hollow fiber bundle. Figure 6.6(B-C) shows the SEM images of PAI precursor hollow fibers. SEM shows that the PAI precursor hollow fibers (outer diameter ~ 280 μm) exhibited an asymmetric structure with a porous substrate having large and interconnected pores and a dense skin layer on the outer surface. The PAI precursor hollow fiber membranes showed CO_2 permeance of 1.54 GPU and CO_2/N_2 ideal selectivity of 31.2 under single-gas CO_2/N_2 permeation at room temperature. The CO_2/N_2 ideal selectivity was within 90% of the intrinsic value measured in thick Torlon® dense films, indicating that the PAI precursor hollow fiber membranes were defect-free.[137] Notably, although the lab relative humidity (62%) during hollow fiber spinning was much higher than a previous work (18%), defect-free hollow fiber membranes were still obtained.[139]

Table 6.2: Polymer dope composition and hollow fiber spinning conditions for fabrication of Torlon® polyamide-imide precursor hollow fiber membranes.

Spinning Conditions	Unit	Value
Dope composition	wt% Torlon®	34.0
	wt% NMP	47.2
	wt% THF	11.8
	wt% Ethanol	7.0
Spinning temperature	°C	50
Lab relative humidity	%	62
Quench bath temperature	°C	50
Dope/bore fluid flow rate	cm^3/h	180/60
Bore fluid composition	NMP/H_2O	80/20
Air gap height	cm	22
Fiber take-up rate	m/min	32

PAI-derived CMS hollow fiber membranes (outer diameter ~ 185 μm) were successfully made by pyrolysis of the defect-free Torlon® PAI precursor hollow fiber membranes at 925°C under continuous argon purge. Figure 6.6(D-E) shows the SEM images of PAI-derived CMS hollow fibers. CMS hollow fiber membranes are traditionally made from precursor hollow fibers comprising polymers with high glass transition temperature (T_g) above 320°C (e.g., polyimides, polybenzimidazoles). Pyrolysis of precursor hollow fibers comprising low-T_g polymers (e.g., PVDF) can lead to structural deformation in CMS hollow fiber membranes.[96] Although the Torlon® PAI had lower T_g (273°C) than polyimides and polybenzimidazoles, CMS hollow fiber membranes were successfully formed without any structural deformation.[137] Without pre-treatments, pore collapse and wall densification are known to occur in precursor hollow fibers during pyrolysis.[91, 126] The PAI precursor hollow fibers underwent pore collapse during pyrolysis and hence the PAI-derived CMS hollow fiber

membranes had totally densified wall of 51 μm with few macrovoids. The totally densified wall allowed for unambiguous determination of the CMS membrane's separation layer thickness (51 μm).

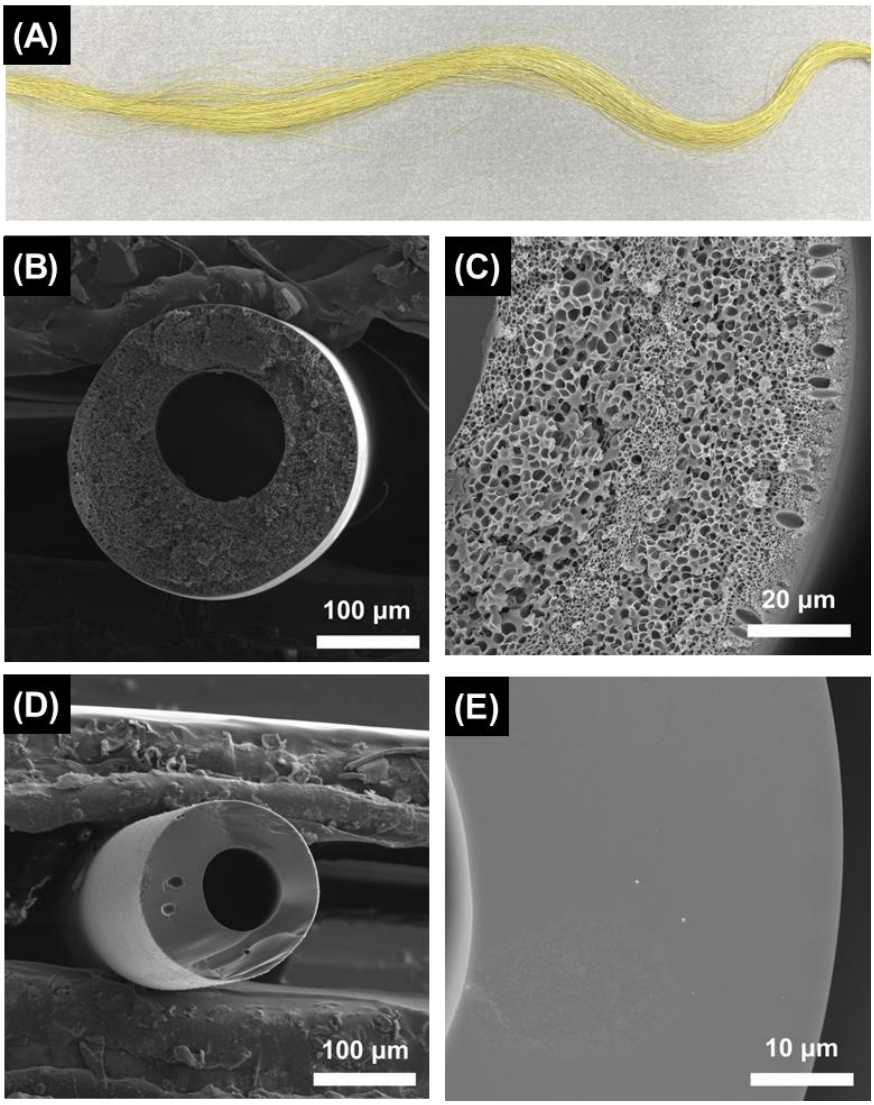

Figure 6.6: (A) Photo of the Torlon® PAI precursor hollow fiber bundle; SEM images of defect-free Torlon® PAI precursor hollow fiber membranes and PAI-derived CMS hollow fiber membranes. (B) Precursor hollow fiber overview; (C) Precursor hollow fiber wall; (D) CMS hollow overview; (E) CMS hollow fiber wall.

6.3 Gas separation performance in CMS membranes derived from different polymer precursors

To understand the effect of precursor amide moieties on the gas separation performance of the CMS membranes, we carried out single-gas He, H_2, and CO_2 permeation at 10 bar and 35°C in the CMS hollow fiber membranes derived from the polyimide (Matrimid®), polyamide-imide (Torlon®) and polyaramid (MTI) precursors at 925°C (Table 6.3). The H_2/CO_2 and He/CO_2 separation performance on the Robeson 2008 upper bound plots are shown in Figure 6.7 (A and B).[28] While the three polymer precursor membranes demonstrated unattractive single-gas H_2/CO_2 and He/CO_2 separation performance, the CMS membranes derived from these precursors showed significant improvements in the single-gas H_2/CO_2 and He/CO_2 separation performance. Notably, CMS membranes derived from all three precursors demonstrated single-gas H_2/CO_2 separation performance above the Robeson 2008 upper bound. However, only the PA-derived CMS membrane showed He/CO_2 separation performance beyond the Robeson 2008 upper bound. While He/CO_2 permeation results are much less reported than the H_2/CO_2 pair, it is an important separation for helium extraction from natural gas.[140]

H_2 permeability of the three CMS membranes had the following order: PI-CMS > PAI-CMS > PA-CMS while H_2/CO_2 ideal selectivity of the three CMS membranes had the following trend: PI-CMS < PAI-CMS < PA-CMS. Interestingly, the trend was translated into the CMS membranes. The PA-derived CMS membrane had ultra-high H_2/CO_2 ideal selectivity (366), however, had low H_2 permeability of 9 Barrer. The PI-derived CMS membrane had much higher H_2 permeability (117 Barrer) yet with

unattractive H_2/CO_2 ideal selectivity (12.7). In comparison, the PAI-derived CMS membrane showed intermediate H_2 permeability (33 Barrer) and H_2/CO_2 ideal selectivity (94). Similar trend in He permeability and He/CO_2 ideal selectivity was observed for the He/CO_2 pair. As the concentration of precursor amide moiety follows the trend: PI-CMS < PAI-CMS < PA-CMS, we see an increase in ideal selectivity and a decrease in single-gas permeability in the CMS membranes derived from polymer precursors with an increasing trend in concentration of precursor amide moieties.

In addition to single-gas permeation, we performed H_2/CO_2 mixed-gas permeation measurements using an equimolar H_2/CO_2 mixture at 2 bar and 35°C in the CMS membranes derived from the polyimide (Matrimid®), polyamide-imide (Torlon®) and polyaramid (MTI) precursors at 925°C. Figure 6.7(A) shows the H_2/CO_2 mixed-gas separation performance on the Robeson 2008 upper bound plot. The trends in mixed-gas separation performance of the three CMS membranes were similar to those observed in case of single-gas permeation. The mixed-gas H_2 permeability and H_2/CO_2 separation factor were lower than H_2 permeability and H_2/CO_2 ideal selectivity measured under single-gas permeation possibly due to competitive sorption effects from the highly condensable CO_2. Similar reduction in H_2 permeability and H_2/CO_2 separation factor were observed in CMS membranes derived from other polymer precursors.[10, 50]

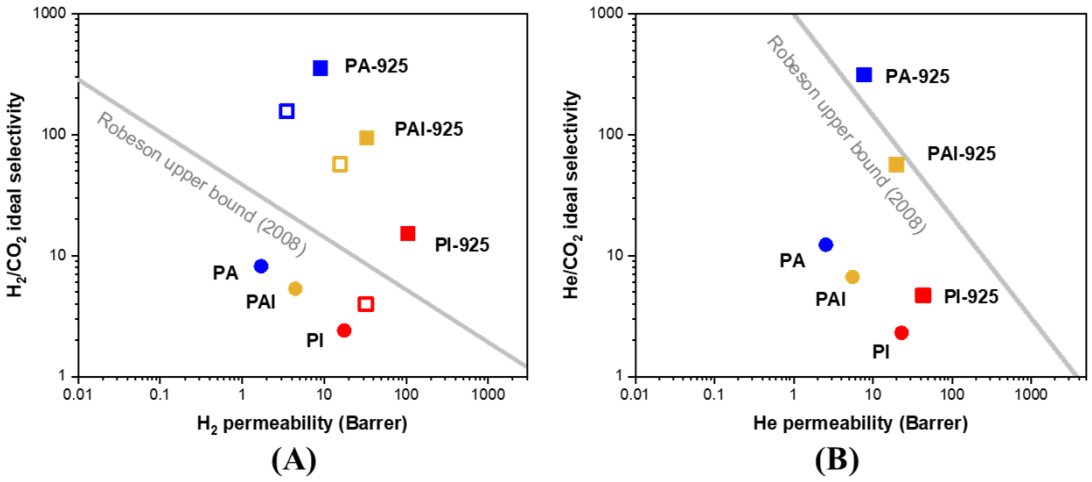

Figure 6.7: (A) H_2/CO_2 separation performance of precursor polymer membranes and CMS membranes. (B) He/CO_2 separation performance of precursor polymer membranes and CMS membranes. Single-gas permeation tests on the precursor membranes was performed at 1 bar and 35°C. Single-gas permeation tests on the CMS membranes were performed at 10 bar and 35°C. Mixed-gas permeation tests on the CMS membranes were performed at 2 bar and 35°C using an equimolar H_2/CO_2 feed mixture. (Solid symbols: single-gas permeation results; hollow symbols: mixed- gas permeation results; stars: permeation results of CMS membranes; squares: permeation results of precursor polymer membranes).

Table 6.3: Gas permeabilities (35°C) in the CMS membranes. Numbers in () represent permeabilities measured under mixed-gas permeation.

Membrane	Module #	P(He)/ Barrer	P(H_2) /Barrer	P(CO_2) /Barrer
PI-925	M1	42.96	116.51 (32.3)	9.16 (8.12)
	M2	-	93.49	4.63
PA-925	M1	7.24	8.31 (3.5)	0.02 (0.02)
	M2	8.21	9.77	0.031
PAI-925	M1	19.3	30.7 (14.5)	0.277 (0.27)
	M2	20.6	35.7 (16.8)	0.428 (0.28)

Although Matrimid®-derived CMS membranes can give ultra-high H_2/CH_4 selectivity above 40000 and CO_2/CH_4 selectivity above 3600,[43] it is not competitive

with the PAI-derived CMS membrane and PA-derived CMS membrane for H_2/CO_2 and He/CO_2 separation. The results shown in Figure 6.7 had three implications to the fundamental understanding of structure-property relationships in CMS membranes. First, precursor backbone chemistry is crucial to determine the separation performance of CMS membranes. Second, differences in precursor transport properties may be amplified in the derived CMS membranes. For example, the PAI precursor had 1.2 times higher H_2/CO_2 ideal selectivity than the PI precursor, whereas the PAI-derived CMS membrane had almost 7 times higher H_2/CO_2 ideal selectivity than the PI-derived CMS membrane. Third, the concentration of amide moieties in polymer precursor backbone can significantly affect the gas separation performance of the resulting CMS membranes.

6.4 Gas sorption and diffusion in CMS membranes derived from different polymer precursors

We measured H_2 and CO_2 sorption isotherms at 35°C in the CMS dense films derived from the polyimide (Matrimid®), polyamide-imide (Torlon®) and polyaramid (MTI) precursors at 925°C. Figure 6.8 compares the H_2 and CO_2 sorption isotherms of the CMS membranes derived from PI, PAI and PA precursors. Henry's law was used to fit the H_2 sorption isotherm, whereas the dual-mode sorption model[74] was used to fit the CO_2 sorption isotherm to obtain the sorption parameters. Table 6.4 compares the H_2 and CO_2 sorption parameters for the CMS membranes derived from PI, PAI and PA precursors. The sorption parameters allowed us to calculate H_2 and CO_2 sorption coefficients and H_2/CO_2 sorption selectivity in the CMS membranes. Based on the single-gas H_2/CO_2 permeation results and the sorption-diffusion model,[66] H_2 and

CO_2 diffusivities and H_2/CO_2 diffusion selectivity in the CMS membranes were obtained. Table 6.5 compares the evaluated diffusivities, sorption coefficients, diffusion selectivities, and sorption selectivities of the CMS membranes derived from PI, PAI and PA precursors. Figure 6.9 shows the diffusion and sorption selectivities in the CMS membranes derived from PI, PAI and PA precursors.

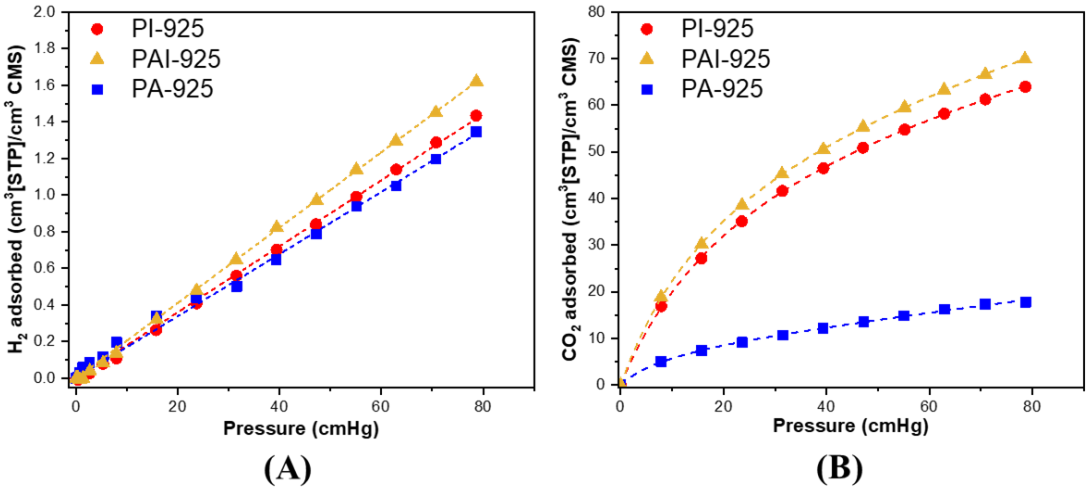

Figure 6.8: (A) H_2 sorption isotherms and (B) CO_2 sorption isotherms (35°C) in CMS membranes.

Table 6.4: Sorption parameters of the CMS membranes obtained from fitting the experimental sorption isotherms (35°C) with Henry's Law (H_2) or the dual-mode sorption model (CO_2).

CMS membrane	H_2	CO_2		
	k_d, $cm^3(STP)/cm^3(CMS)$ cmHg	k_d, $cm^3(STP)/cm^3(CMS)$ cmHg	C_H', $cm^3(STP)/cm^3(CMS)$	b, $cmHg^{-1}$
PI-CMS	0.0180	0.209	62.96	0.040
PAI-CMS	0.0205	0.278	61.16	0.047
PA-CMS	0.0170	0.135	8.544	0.105

Table 6.5: H_2 and CO_2 sorption coefficients and diffusivities in the CMS membranes. The sorption coefficients were evaluated at 10 bar and 35°C using the sorption parameters in Table 6.4. The diffusivities were calculated using single-gas permeabilities and the sorption coefficients according to the sorption-diffusion model.

Membrane	D (H_2) ×10^9, cm^2/s	D (CO_2) ×10^9, cm^2/s	S (H_2), cm^3(STP)/cm^3(CMS) cmHg	S (CO_2), cm^3(STP)/cm^3(CMS) cmHg
PI-CMS	646	3.16	0.018	0.289
PAI-CMS	157	0.099	0.021	0.356
PA-CMS	53.2	0.017	0.017	0.146

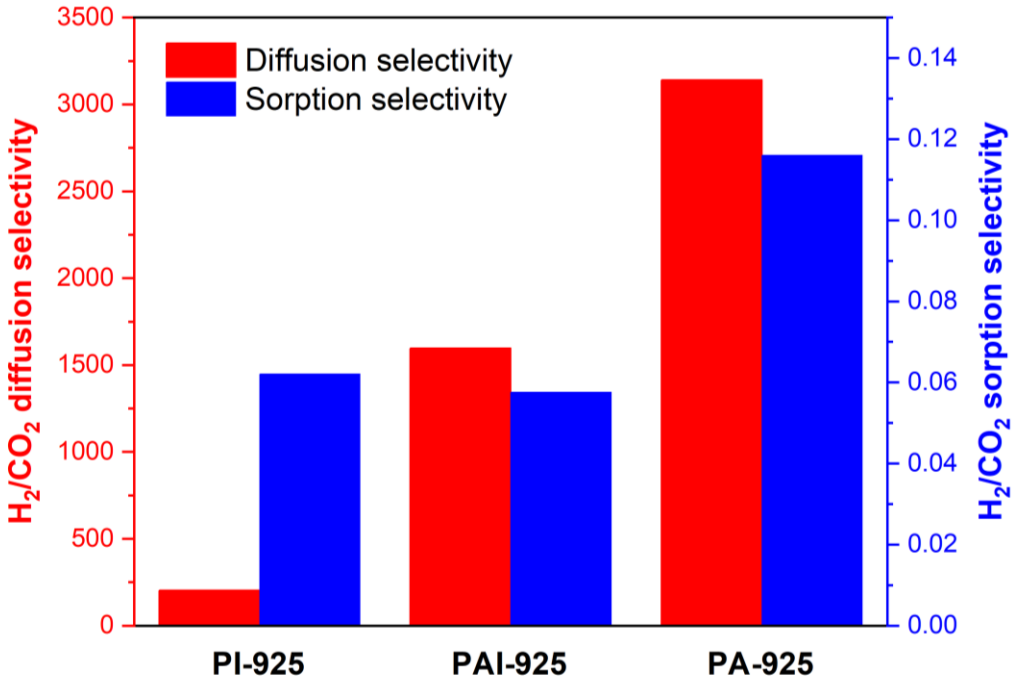

Figure 6.9: H_2/CO_2 diffusion selectivity and H_2/CO_2 sorption selectivity in CMS membranes.

All CMS membranes had similar H_2 sorption coefficients. The PAI-derived CMS membrane had comparable H_2/CO_2 sorption selectivity with the PI-derived CMS membrane (~0.06), which was lower than the PA-derived CMS membrane (~0.11). The H_2/CO_2 diffusion selectivity of the PI-derived CMS membrane was only 204, which

was responsible for its unattractive H_2/CO_2 ideal selectivity. The ultra-high H_2/CO_2 ideal selectivity of the PA-derived CMS membrane can be attributed to its H_2/CO_2 diffusion selectivity of 3000.[132] Notably, the H_2 diffusivity of the three CMS membranes observed the following trend: PI-CMS > PAI-CMS > PA-CMS while the H_2/CO_2 diffusion selectivity of the three CMS membranes had the following trend: PI-CMS < PAI-CMS < PA-CMS. Hence, the trends observed in the H_2 diffusivity and the H_2/CO_2 diffusion selectivity were in direct correlation with the trends in H_2 permeability and H_2/CO_2 ideal selectivity.

The H_2/CO_2 diffusion selectivity reflects the CMS membrane ultramicropore's capability to differentiate H_2 and CO_2 molecules based on their kinetic diameter difference (2.9 vs 3.3 Å). Based on the trend observed for H_2/CO_2 diffusion selectivity in the three CMS membranes, we hypothesize that the increase in H_2/CO_2 diffusion selectivity is related to the decreasing trend in ultramicropore size as follows: PI-CMS > PAI-CMS > PA-CMS. Under identical pyrolysis conditions, polymer precursors with closely packed chains can provide closely packed aromatic strands and graphitic plates during pyrolysis to give CMS membranes with small ultramicropores. Therefore, the trend in ultramicropore size of the CMS membranes derived from the different polymer precursors can be correlated to the trends in d-spacing and FFV in the polymer precursors as explained in section 6.2.1.

6.5 Characterization of CMS membranes derived from different polymer precursors

To support the hypothesis that the ultra-high H_2/CO_2 ideal selectivity in the PA-derived CMS membrane is due to the presence of highly refined ultramicropores, we characterized and compared the pore structure of the CMS dense films derived from

the polyimide (Matrimid®), polyamide-imide (Torlon®) and polyaramid (MTI) precursors at 925°C. Physisorption of CO_2 at 0°C is widely used to examine CMS membrane pore structure. The CO_2 sorption isotherms were fitted with a DFT model (0°C, carbon slit pores) to obtain the pore size distribution curves and cumulative pore volume. The pore size distribution and cumulative pore volume of the CMS membranes are depicted in Figure 6.10. The PAI-derived CMS membrane had similar pore volume with the PI-derived CMS membrane, which were both much larger than the PA-derived CMS membrane. Notably, no appreciable differences in pore size were seen in the three CMS membranes. While CO_2 physisorption is broadly used to study the pore structure of nanoporous carbon,[43, 141] we believe it has limitations to characterize CMS membranes for H_2/CO_2 separations. First, it cannot reliably characterize CMS membrane pore structure if the CO_2 probe molecule is excluded from CMS membrane pores such as in the PA-derived CMS membrane with highly refined ultramicropores.[132] Second, the DFT model can only calculate pores larger than 3.6 Å if CO_2 sorption isotherms are used. Hence, CO_2 physisorption cannot characterize pores between 2.9 and 3.3 Å to obtain the crucial pore structure knowledge needed to evaluate CMS membranes for H_2/CO_2 separation.

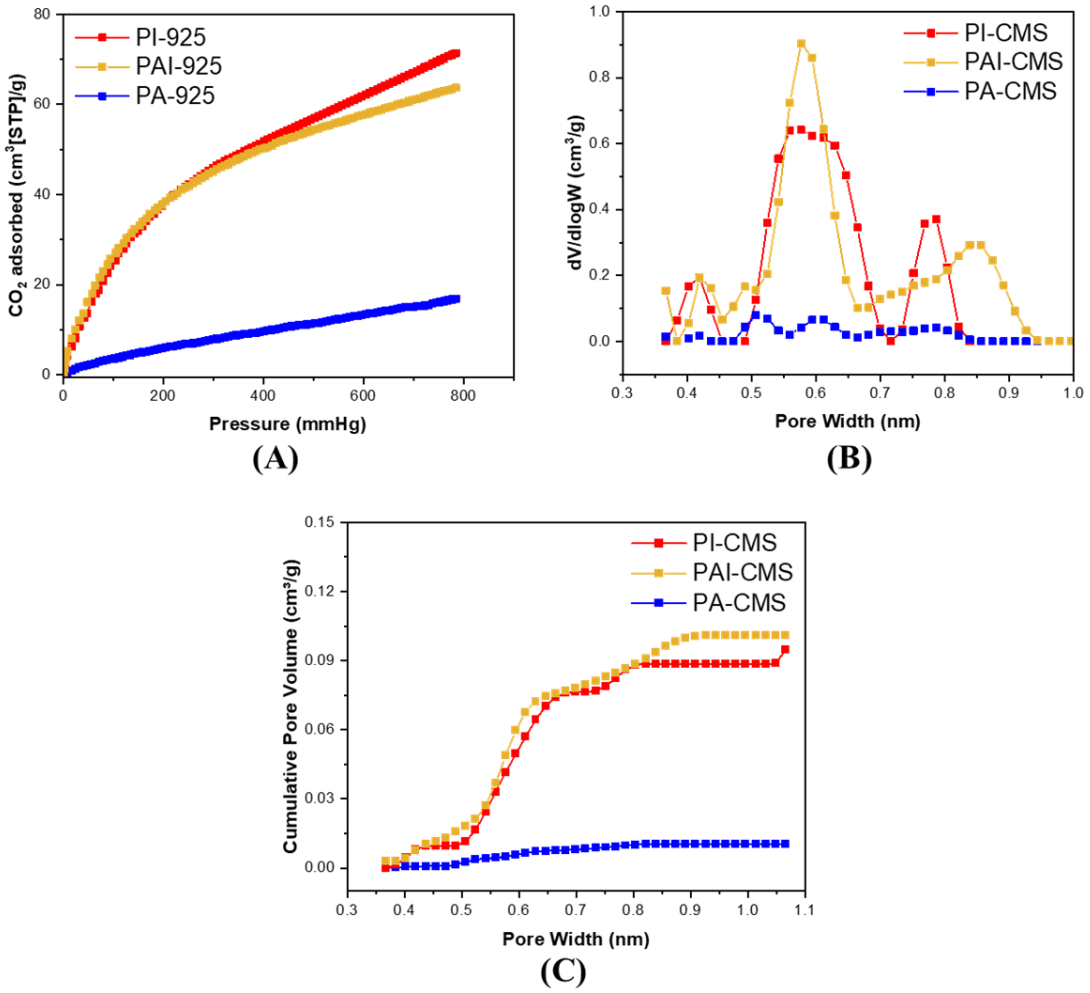

Figure 6.10: Characterizing the CMS membrane pore structure using CO_2 physisorption at 0°C. (A) CO_2 sorption isotherms (0°C), (B) Pore size distribution curves; (C) Cumulative pore volume.

Since CO_2 physisorption was not useful for this study, X-ray photoelectron spectroscopy (XPS) was carried out to characterize the CMS membrane pore structure. Table 6.6 shows the elemental composition calculated in polymer precursors. XPS full spectral scans for the CMS membranes are shown in Figure 6.11. The results show that all three CMS membranes contained carbon, nitrogen, and oxygen. Elemental

compositions in the CMS membranes were evaluated using the peaks obtained in the XPS full spectral scans and are shown as insets in Figure 6.11.

Table 6.6: Theoretical elemental compositions of the precursor polymers calculated from their repeat units.

Element	Composition (wt%)		
	PI	PAI	PA
Carbon	76.1	70.2	70.6
Nitrogen	5.1	8.5	11.8
Oxygen	14.5	18.0	13.5
Hydrogen	4.3	3.3	4.1

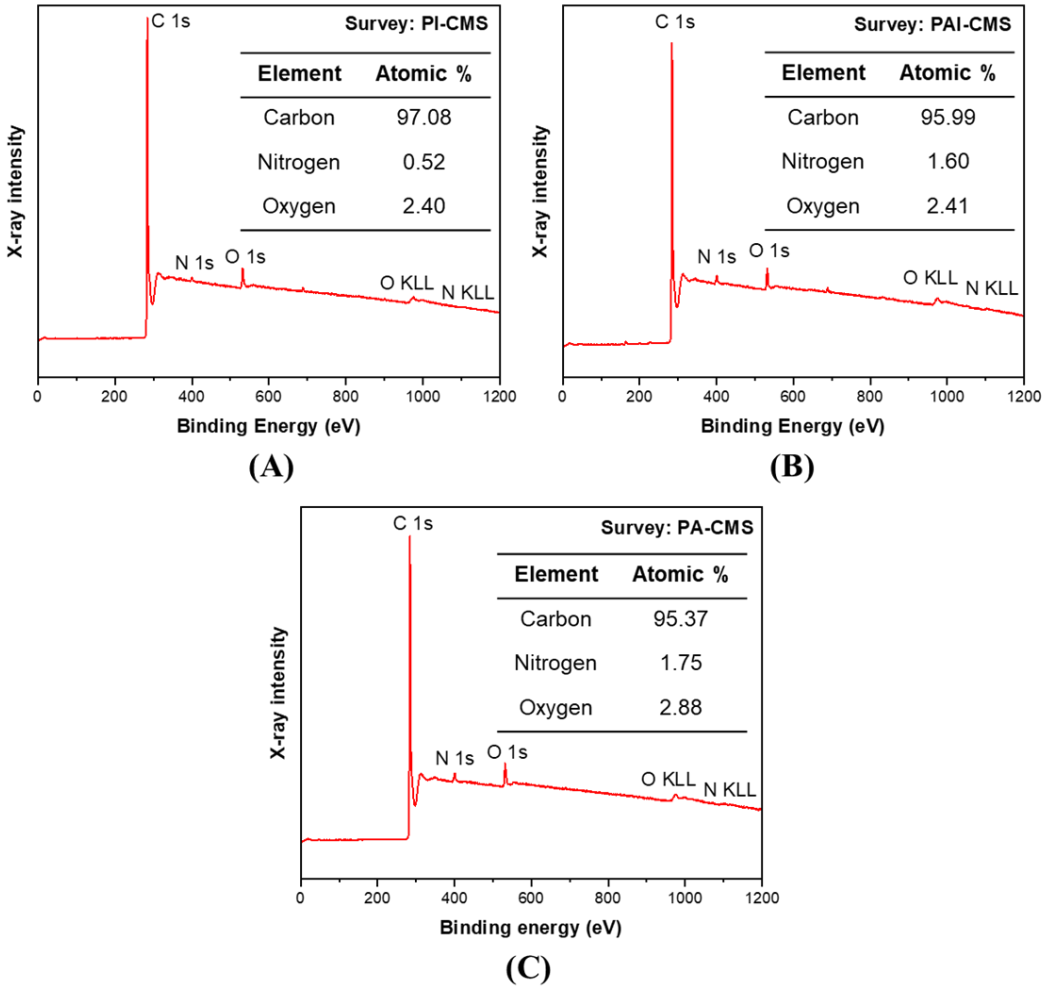

Figure 6.11: XPS survey spectra of CMS membranes with indicated elemental composition.

High-resolution N1s spectra shown in Figure 6.12 indicate the types of nitrogen functionalities present in the CMS membranes. CMS membranes show characteristic peaks at binding energies of 398eV, 401eV, and 403eV which can be attributed to pyridinic-N, graphitic-N, and valley-N nitrogen functionalities, respectively.[142] The order of nitrogen weight percentage (PA-CMS [1.75%] > PAI-CMS [1.6%] > PI-CMS [0.52%]) shown in Figure 6.11 is consistent with the elemental composition in polymer precursors shown in Table 6.5.

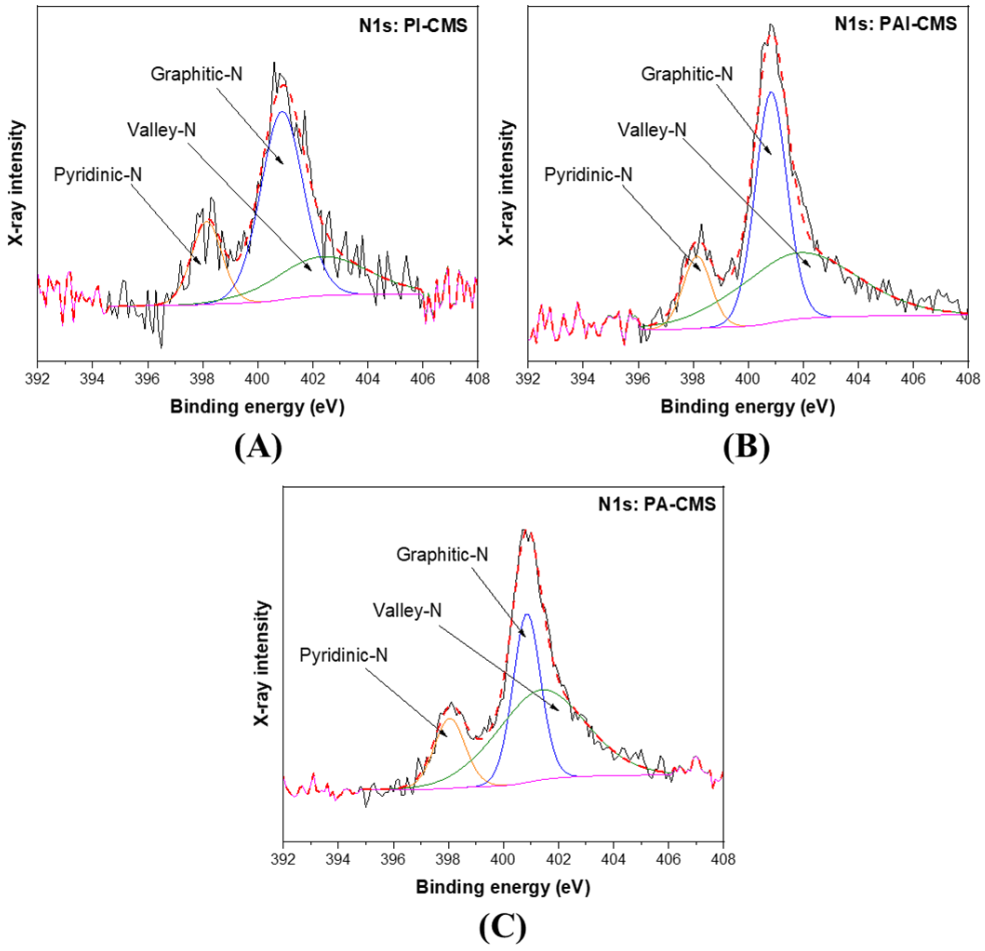

Figure 6.12: High resolution XPS N1s spectra of (A) PI-derived CMS membrane; (B) PAI-derived CMS membrane and (C) PA-derived CMS membrane.

High-resolution O1s spectra shown in Figure 6.13 indicate the types of oxygen functionalities in the CMS membranes. CMS membranes show characteristic peaks at binding energies of 530.5eV and 532.5eV corresponding to double-bonded oxygen to carbon (oxygen in carbonyl or carboxylic acid functionalities) and single-bonded oxygen to carbon (oxygen in phenolic or epoxide functionalities), respectively. An additional peak at binding energy of 535.5eV can be attributed to chemisorbed/intercalated O_2 and H_2O.[143] The larger percentage of oxygen functionalities in the PA-derived CMS membrane can be attributed to more strongly sorbed molecular O_2 and H_2O due to its higher surface polarity as evidenced by the larger Langmuir affinity constant as shown in Table 6.3.

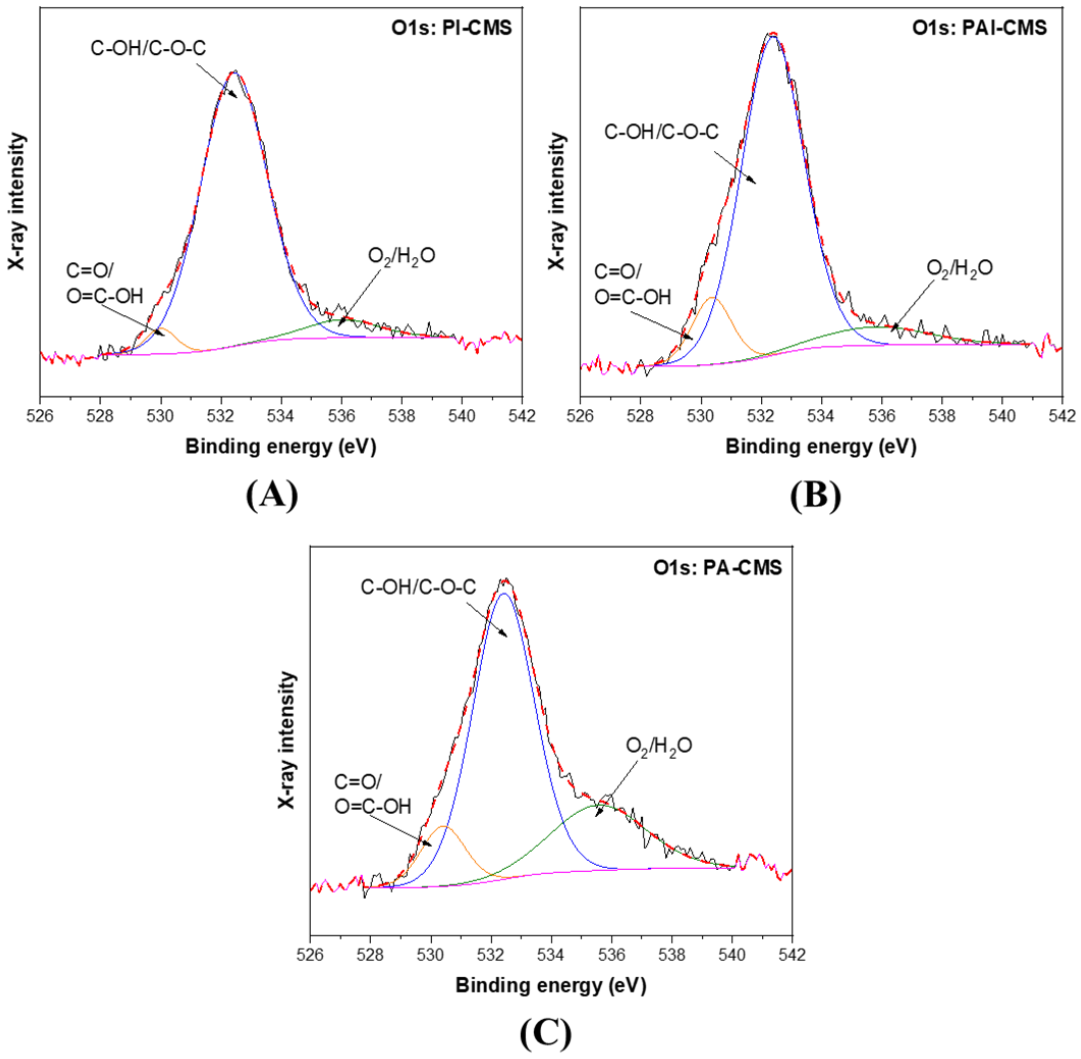

Figure 6.13: High resolution XPS O1s spectra of (A) PI-derived CMS membrane; (B) PAI-derived CMS membrane and (C) PA-derived CMS membrane.

High-resolution C1s spectra shown in Figure 6.14 were obtained to quantify the sp^3/sp^2 carbon ratio in the CMS membranes. The C1s spectra were deconvoluted into three peaks corresponding to sp^2 C (284 eV), sp^3 C (286 eV) and C-O functionalities (290 eV).[64] The ratio of sp^3/sp^2 carbon was evaluated using the ratio of the respective peak areas in the C1s spectra. The sp^3/sp^2 carbon ratio is indicative of the level of disorder in the amorphous graphitic structure of the CMS membranes, i.e., smaller

sp^3/sp^2 carbon ratio suggests a more ordered graphitic structure and hence smaller CMS membrane inter-plate spacing and ultramicropore size. The sp^3/sp^2 carbon ratio of the three CMS membranes had the following order: PI-CMS > PAI-CMS > PA-CMS. The finding thus supports the hypothesis that the PA-derived CMS membrane has highly refined ultramicropores that can efficiently discriminate between the permeating H_2 and CO_2 molecules.

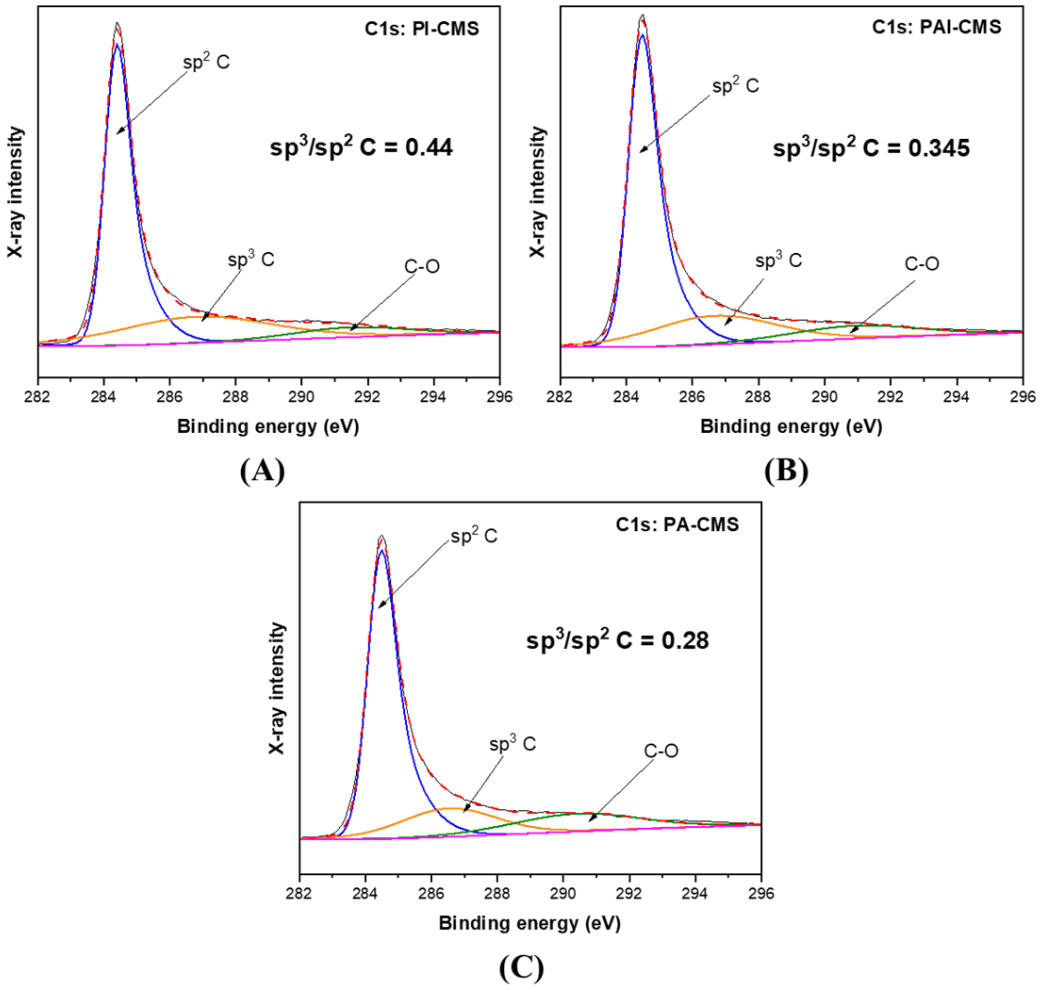

Figure 6.14: High resolution XPS C1s spectra of (A) PI-derived CMS membrane; (B) PAI-derived CMS membrane and (C) PA-derived CMS membrane.

To complement the XPS analysis, we carried out Raman spectroscopy to further investigate the CMS membrane pore structure. Raman spectra for the CMS membranes are shown in Figure 6.15. Two characteristic bands commonly observed for amorphous carbonaceous materials – the D band (~1350 cm^{-1}) and G band (~1590 cm^{-1}) were seen in the Raman spectra of all three CMS membranes. The D band was related to the A_{1g}-symmetry vibrational mode of structural defects, indicating presence of disorder in the carbon structure. The G band was related to the E_{2g}-symmetry mode of the aromatic sp^2-carbon and linear chains corresponding to C=C in-plane stretching in graphitic carbon materials. With increasing degree of disorder and presence of oxygenated functionalities, secondary peaks appear in the D band. Therefore, each Raman spectrum was decoupled using 5 Gaussian peaks – D1, D2, D3, D4, G to fit the experimental data.[98] The D1 peak (~1350 cm^{-1}) was associated with the basal plane defects in the graphitic structure. The I_{D1}/I_G ratio[98] can be used as a measure of the concentration of sp^2 carbon, i.e., lower I_{D1}/I_G ratio indicates higher concentration of sp^2 carbon and smaller ultramicropores. The I_{D1}/I_G ratio of the three CMS membranes had the following order: PI-CMS > PAI-CMS > PA-CMS. The finding is hence consistent with the results of XPS and supports the hypothesis that the PA-derived CMS membrane has highly refined ultramicropores.

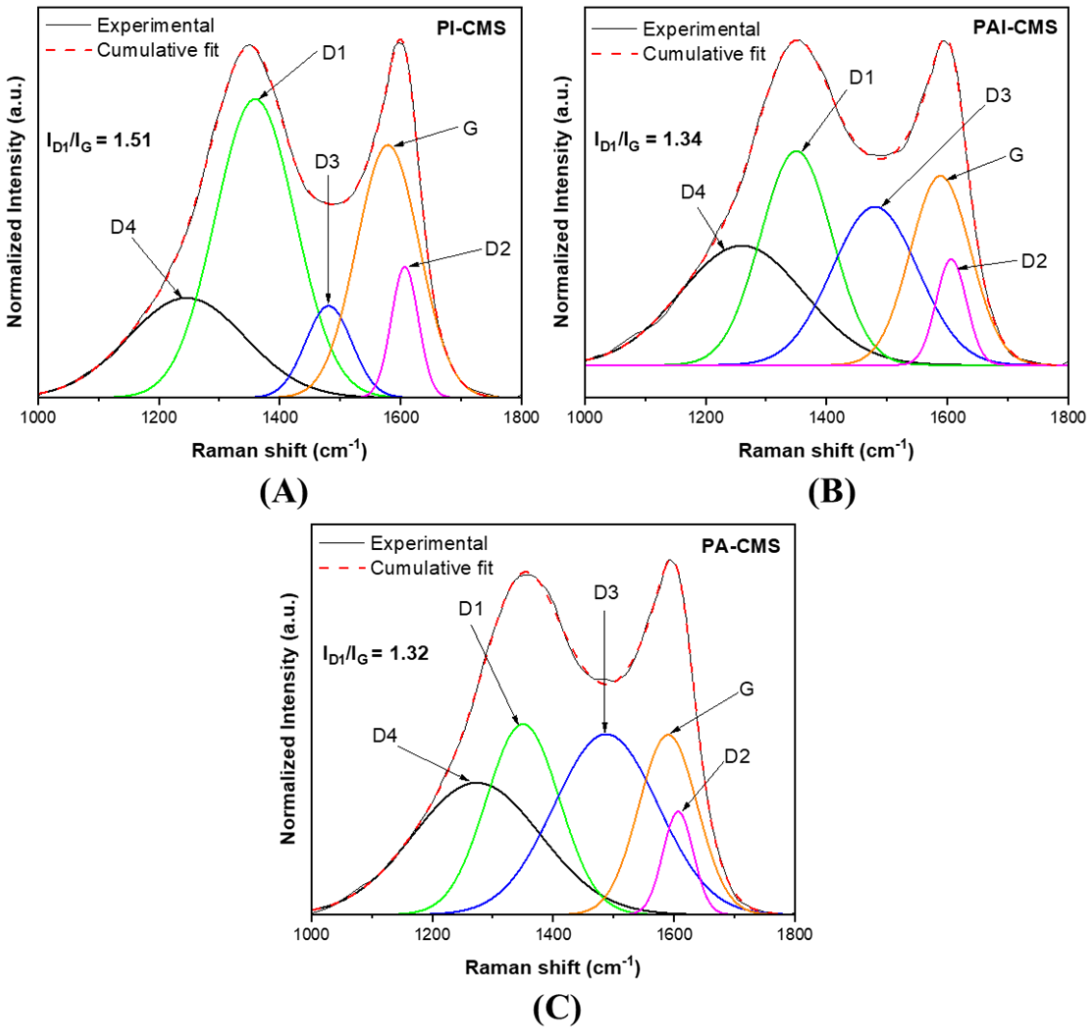

Figure 6.15: Raman spectra of (A) PI-derived CMS membrane; (B) PAI-derived CMS membrane and (C) PA-derived CMS membrane.

6.6 Effect of precursor amide moieties on the CMS membrane pore structure and separation performance

Amide moieties in the polymer precursor provide strong intermolecular hydrogen bonding interactions between the neighboring polymer chains thereby restricting the segmental motions of the polymer chains.[59] FTIR spectra (Figure 6.1) indicate the difference in hydrogen bonding strength arising due to differences in the

concentration of backbone amide moieties in the polyimide (Matrimid®), polyamide-imide (Torlon®) and polyaramid (MTI) precursors. The trends observed in the d-spacing, density and FFV of the polymer precursors indicate that the hydrogen bonding between amide moieties in the polymer backbone strongly affect the properties of the polymer precursor. Higher the concentration of precursor amide moieties, stronger the hydrogen bonding, higher the density and lower the d-spacing and FFV of the polymer precursors. Hence, the MTI polyaramid precursor exhibits the highest density and lowest d-spacing and FFV as compared to the Torlon® polyamide-imide and Matrimid® polyimide.

The gas permeation and sorption results provide clear evidence of the effect of precursor amide moiety concentration on the gas separation performance of the CMS membranes. The higher the concentration of precursor amide moieties, lower the gas diffusivity and permeability, and higher the diffusion selectivity and ideal selectivity. The trends observed in gas separation performance of the CMS membranes was due to differences in the ultramicropore size of the CMS membranes derived from the different polymer precursor, which is evidenced by the CMS pore structure characterization results. Under identical pyrolysis conditions, the PA-derived CMS membrane possesses highly refined ultramicropores compared to the PI-derived CMS membrane and the PAI-derived CMS membrane, leading to the ultra-high diffusion selectivity and ideal selectivity.

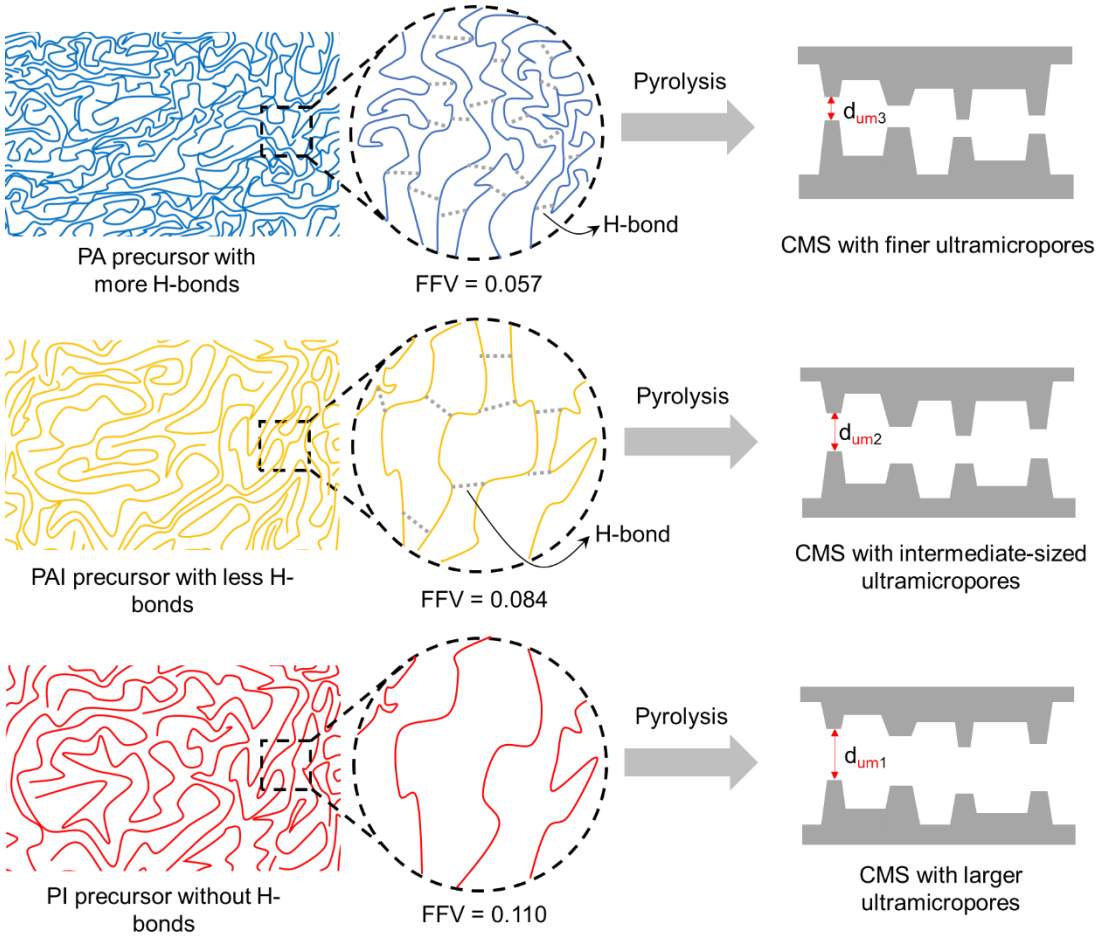

Figure 6.16: Schematic correlating the CMS ultramicropore size to polymer precursor hydrogen bonding between amide moieties in the polymer precursors.

The difference in CMS ultramicropore size can be correlated to the difference in precursor amide moiety concentration. Figure 6.16 provides a schematic representation of this correlation. The MTI polyaramid precursor with the highest precursor amide moiety concentration, has stronger hydrogen bonds and hence closer chain packing than the Torlon® polyamide-imide and Matrimid® polyimide. The closer chain packing in the MTI polyaramid precursor is evident from its higher density, lower FFV and lower d-spacing compared to the polyamide-imide and polyimide precursors. The closer chain packing in polyaramid provides more intimately spaced aromatic

strands following pyrolysis, thereby giving smaller ultramicropores and higher diffusion selectivity and ideal selectivity in the PA-derived CMS membrane. Hence, the highly refined ultramicropores in the PA-derived CMS membrane is directly related to the high concentration of hydrogen-bonded amide moieties in the MTI polyaramid precursor.

Chapter 7: Conclusions and Recommendations

7.1 Conclusions

Membrane separation processes can potentially debottleneck the H_2 purification process by providing an energy-efficient and cost-effective alternative to the conventional separation technologies such as pressure-swing adsorption (PSA) and cryogenic distillation. To achieve commercial success, high performance membrane materials with high H_2 productivity and H_2/CO_2 separation efficiency are required to minimize membrane area and maximize H_2 product purity. This dissertation presents the development of carbon molecular sieve (CMS) membranes derived from interfacially polymerized polyaramids intended for H_2/CO_2 separation application. The results towards achieving the objectives highlighted in Chapter 1 are summarized below.

1. **Investigate the formation and gas transport properties of CMS membranes derived from polyaramid.**

In chapter 4, we showed that pyrolysis of a polyaramid precursor can provide CMS membranes with highly attractive gas separation performance. An uncrosslinked polyaramid was synthesized by stirred interfacial polymerization. The polyaramid's excellent solution processability allowed the fabrication of polyaramid precursor hollow fibers by solution spinning, which gave dense-wall CMS hollow fiber membranes by pyrolysis. We systematically studied the pore structure and gas permeation characteristics of the polyaramid-derived CMS membranes at different pyrolysis temperatures, which enabled us to optimize the CMS fabrication conditions

for H_2/CO_2 separation. Single-gas permeation suggested that the polyaramid-derived CMS membrane pyrolyzed at 925℃ had competitive H_2 permeability and ultra-high H_2/CO_2 ideal selectivity of 366. The polyaramid-derived CMS membrane also showed outstanding H_2/CO_2 separation factor (~156) under H_2/CO_2 mixed-gas permeation tests, suggesting its promise for H_2 purification and CO_2 capture applications for blue H_2 production. To our best knowledge, this is the first report of CMS membranes derived from polyaramids or interfacially polymerized polymers. The findings of this work pave the way for a new class of scalable and tunable CMS membranes for separations.

2. **Investigate the H_2/CO_2 separation performance of polyaramid-derived CMS membranes under realistic syngas operating conditions.**

In chapter 5, we fabricated polyaramid-derived CMS hollow fiber membranes at 1050°C (i.e., MTI-1050) to push the limit of H_2/CO_2 selectivity. The ultramicropores were more refined in CMS membranes pyrolyzed at 1050°C as compared to the CMS membranes pyrolyzed at 925°C, which was confirmed using pore structure characterizations. The finer ultramicropores in CMS membrane pyrolyzed at 1050°C enabled outstanding H_2/CO_2 mixed-gas separation factors up to ~ 4500 under high temperature mixed-gas permeation experiments, which was more than one order of magnitude higher than the most selective CMS membrane reported in literature. The separation factor showed a decreasing trend with increasing permeation temperature as the CO_2 permeation activation energy was larger than that of H_2. The larger CO_2 permeation activation energy was attributed to a large CO_2 diffusion activation energy possibly due to the highly refined ultramicropores. Finally, a one-dimensional hollow

fiber membrane model was used to demonstrate the attractiveness of the MTI-1050 CMS membrane for enrichment of highly pure H_2 product. The simulation results indicated that a membrane separator consisting of the MTI-1050 CMS membrane is capable of producing 99.95% H_2 product with 90% H_2 recovery.

3. Elucidate the role of precursor amide moiety on pore structure-transport property relationship of CMS membranes.

In chapter 6, we fabricated CMS membranes derived from polyimide (PI) and polyamide-imide (PAI) precursors at identical pyrolysis conditions with the MTI-925 CMS membrane. The results of this chapter allowed us to gain an understanding on the effect of precursor amide moiety on the pore structure and transport properties of CMS membranes. The PAI had intermediate H_2 permeability and H_2/CO_2 selectivity between the PI and PA. The trend was translated into the CMS membranes, with the PAI-derived CMS membrane showing intermediate H_2 permeability and H_2/CO_2 selectivity between the PI-derived CMS membrane and the PA-derived CMS membrane, in both single-gas and mixed-gas permeation studies. Sorption studies suggest that it was because the PAI-derived CMS membrane had intermediate H_2 diffusivity and H_2/CO_2 diffusion selectivity, which was attributed to its intermediate ultramicropore size, supported using CMS pore structure characterization. Hence, the results of this chapter show that introducing precursor amide moiety is a powerful tool to control the pore structure and transport properties of CMS membranes, i.e., increasing concentration of precursor amide moieties can provide CMS membranes with more refined ultramicropores and therefore stronger size-sieving abilities. These findings can provide a valuable guide to

control and finely tune the pore structure and gas transport properties in CMS membranes.

The findings of this chapter have three implications to the fundamental understanding of structure-property relationships in CMS membranes. First, precursor backbone chemistry is crucial to determine the separation performance of CMS membranes. Second, differences in precursor transport properties may be amplified in the derived CMS membranes. Third, pyrolysis of copolymers with mixed backbone chemistry can be used as a strategy to develop CMS membranes with simultaneously attractive permeability and selectivity.

7.2 Recommendations for future work

The results of this dissertation provide the proof-of-concept for polyaramid-derived CMS membranes for H_2 separation and CO_2 capture applications. The systematic investigation of intrinsic gas separation performance and pore structure characteristics of the polyaramid-derived CMS membranes shows promising evidence which could lead to the commercial success of these membranes. However, to provide additional support for establishing commercial viability of polyaramid-derived CMS membranes, certain aspects need to be further investigated.

1. Translating the promising intrinsic H_2/CO_2 separation performance to defect-free polyaramid-derived CMS hollow fiber membranes with ultra-thin separation layers.

This dissertation has successfully achieved fabrication of CMS hollow fiber membranes derived from interfacially polymerized polyaramid precursor. The dense-

wall CMS hollow fiber membranes show promising intrinsic H_2/CO_2 separation performance under single-gas permeation as well as mixed-gas permeation conditions. The H_2 permeance in the dense-walled CMS hollow fibers was low. To achieve successful commercial application, the separation performance presented in this work needs to be translated to CMS hollow fiber membranes with ultra-thin defect-free separation layers and enhanced H_2 permeance.

Developing CMS hollow fiber membranes with ultra-thin defect-free separation layers can achieve high H_2 permeance and consequently reduced membrane area and separator footprint for commercial application. The first strategy to be investigated for developing ultra-thin defect-free membranes involves fabrication of thin-film composite (TFC) CMS hollow fiber membranes from TFC polymer precursor hollow fiber membranes with polyaramid separation layers formed by in situ polymerization. The self-limiting nature of interfacial polymerization can be exploited to achieve successful fabrication of ultra-thin sub-100nm separation layers on porous polymeric substrates.[57] Polyaramid TFC flat sheet membranes are proven to be commercially viable for desalination membrane applications.[57] Researchers have also studied fabrication of TFC hollow fiber membranes with interfacially-polymerized separation layers for desalination application.[144] There are challenges associated with achieving defect-free gas separation performance in the TFC hollow fiber membranes with interfacially-polymerized separation layers. Moreover, development of TFC CMS hollow fiber membranes from TFC polymer precursor hollow fiber membranes with interfacially-polymerized separation layers has not been investigated yet.

Another strategy for developing ultra-thin, defect-free CMS hollow fiber membranes involves fabrication of composite CMS hollow fiber membranes derived from dual-layer polymer precursor hollow fiber membranes with polyaramid sheath layer. Dual-layer polymer hollow fiber membranes have been successfully developed using dry-jet/wet-quench spinning and pyrolyzed to provide composite CMS hollow fiber membranes with separation layers of ~ 1 μm.[46] The separation layer thickness can be more accurately controlled using this strategy by varying the sheath dope flow rate during dual-layer hollow fiber spinning. The sheath dope composition needs to be optimized to achieve formation of defect-free separation layers.

In both these strategies, substrate densification issues need to be circumvented. Pyrolysis-induced substrate densification can adversely affect the formation of ultra-thin CMS separation layers. Highly rigid and solution-processable polymers with smaller $\Delta = T_d - T_g$ need to be selected as the hollow fiber substrates to minimize substrate densification effects.[145] Further, engineering substrate morphology using vinyltrimethoxysilane (VTMS) treatment is reported previously in literature for avoiding substrate densification in both asymmetric and composite CMS hollow fiber membranes.[126]

2. <u>Engineering the polyaramid backbone to achieve tailored separation performance in polyaramid-derived CMS membranes.</u>

In this research, CMS membranes have been developed using the simplest possible aromatic diamine and diacid chloride monomers without any bulky side groups to provide a linear solution-processable polyaramid by stirred interfacial polymerization. This leads to low fractional free volume in the polyaramid due to

strong intermolecular hydrogen bonding interactions, providing CMS membranes with highly refined ultramicropores and moderate H_2 permeability. Due to the availability of an extensive library of aromatic diamines and aromatic diacid chlorides, the polyaramid backbone chemistry can be further engineered to provide CMS membranes with enhanced H_2 permeability. The introduction of bulky side groups into the polyaramid backbone can possibly weaken the intermolecular hydrogen bonding interactions and increase the FFV of the polyaramid, thereby increasing the CMS membranes ultramicropore size and hence H_2 diffusivity and permeability.

Another possible strategy to further engineer the polyaramid backbone chemistry involves incorporation of ion-exchangeable side groups such as $-SO_3H$ into the polyaramid backbone. Interfacial polymerization using aromatic diamine monomers containing pendant $-SO_3H$ functional groups along with aromatic diacid chloride monomers can be done to achieve this. Presence of ion-exchangeable side groups can enable introduction of metal ions such as Fe^{2+} or Fe^{3+} into the polyaramid backbone using ion-exchange protocols, which can eventually provide Fe-containing CMS membranes. Introduction of Fe species may disrupt packing of graphene sheets and increase the ultramicropore size and permeability. Also, the Fe species can potentially allow for C_2H_4/C_2H_6 or C_3H_6/C_3H_8 separations based on olefin facilitated transport.[146]

In chapter 6, a scenario wherein the CMS membrane pore structure and gas separation performance is affected by the intermolecular hydrogen bonding in the polymeric precursor was visualized. Similarly, in other scenarios where the polymeric precursor shows existence of other intermolecular interactions such as π-π stacking,

host-guest chemistry, ion-dipole interactions, etc. the effect of these intermolecular interactions on the CMS membrane pore structure and gas separation performance need to be systematically studied. Findings from these studies can provide an effective tool to effectively control and finely tune the CMS membrane properties for a specific target separation application.

3. Investigation of H_2/CO_2 separation performance in ultra-thin polyamide-imide (PAI)-derived CMS membranes under realistic syngas operating conditions.

In Chapter 6, PAI-derived CMS membranes were reported to demonstrate balanced H_2/CO_2 separation performance, with intermediate H_2 permeability and intermediate H_2/CO_2 separation performance compared to polyaramid-derived CMS membranes and polyimide-derived CMS membranes. Notably, the H_2/CO_2 separation performance was well above the Robeson 2008 upper bound for both single gas and mixed-gas permeation. Hence, pyrolysis of PAI copolymer with mixed backbone chemistry can be used as a strategy to develop CMS membranes with simultaneously attractive H_2 permeability and H_2/CO_2 selectivity. It would be valuable to investigate the H_2/CO_2 separation performance of the PAI-derived CMS membranes under realistic syngas operating conditions at temperatures of 150-250°C and pressures > 7 bar.[7]

The effect of permeation temperature and feed pressure on the H_2/CO_2 separation performance using mixed-gas feeds can be systematically studied in the PAI-derived CMS membrane. The Arrhenius relationship can be used to evaluate permeation activation energy for H_2 and CO_2 in the PAI-derived CMS membrane. The possibility to mitigate competitive sorption effects under mixed-gas feeds at higher temperatures can be investigated. Further, H_2 and CO_2 sorption studies can be

performed at different temperatures to obtain diffusion activation energy and heat of sorption and hence understand the individual contributions of diffusion and sorption. Moreover, the separation performance of the PAI-derived CMS membrane can be tested for stability under long-term operation.

Further, investigating the optimum fabrication strategy to develop ultra-thin, defect-free PAI-derived CMS hollow fiber membranes would be valuable to obtain membranes with enhanced H_2 permeance. Dual-layer hollow fiber spinning can be an effective tool to achieve fabrication of composite CMS hollow fiber membranes with controlled separation layer thickness. The polymer dope composition and hollow fiber spinning conditions need to be systematically studied and optimized to achieve ultra-thin, defect-free polymer hollow fiber membrane fabrication. Additionally, VTMS treatment strategy can be implemented to avoid substrate densification during pyrolysis, thereby translating ultra-thin, defect-free polymer hollow fiber membranes to ultra-thin, defect-free CMS hollow fiber membranes.

4. Characterization of CMS membrane pore structure using CMS hollow fibers.

Polymer chain orientation is known to be an important factor in determining the membrane transport properties. Although polymer chains exist as random coils in solution, external forces such as shear and elongation stresses acting on the polymer chains during hollow fiber spinning can induce molecular orientation and conformational changes in the polymer chains present in the resulting polymeric hollow fiber membranes. Hence, shear and elongation stresses acting on the polymer chains during hollow fiber spinning can affect the polymer chain orientation, thereby affecting the gas separation performance of the polymeric hollow fiber membranes.[147-149] In

this dissertation, CMS dense films were used for CMS membrane pore structure characterization because of easy sample fabrication. However, due to the influence of the hollow fiber spinning process on the polymer chain orientation and conformation, it is suggested to characterize the CMS membrane pore structure using CMS hollow fibers and compare the characterization results with the CMS dense films. For instance, comparing the wide-angle X-ray diffraction (WAXD) spectra using CMS dense films and CMS hollow fibers would provide insights for the effect of polymer chain orientation on pore structure of the resulting CMS membranes.

Appendices

Appendix A: Python code for one-dimensional co-current hollow fiber membrane separator model

Showing example code for simulation (MTI-1050):

Co-current hollow fiber membrane separator model for hydrogen purification

```
import numpy as np
import matplotlib.pyplot as plt
import pandas as pd
from scipy.integrate import odeint
```

ODE input function definition with system input parameters

```
## function definition
def odes(y, z):
  ## Input Parameters
  #Component 1: Hydrogen; Component 2: Carbon dioxide

  #Permeance of H2
  Q_1 = 7.2*3.35*10**-10 #mol/m^2.s.Pa

  #Permeance of CO2
  Q_2 = (7.2*3.35*10**-10)/2677 #mol/m^2.s.Pa
```

```
#Feed pressure

P_f = 10**6 #Pa


#Permeate pressure

P_p = 1*10**5 #Pa


#Fiber dimensions

d_0 = 600*10**-6 #m



#Feed temperature

T_f = 250 + 273.15 #K


#Module ID

d_i_module = 0.3 #m


#Number of fibers

N = 16050000


R = 8.314 #Universal Gas Constant in J/mol.K


# Assigning each ODE to a vector element
```

```
  u_x_1 = y[0]
  u_x_2 = y[1]
  v_y_1 = y[2]
  v_y_2 = y[3]

  #Defining each ODE
  dux1dz = - N*np.pi*d_0*Q_1*(P_f*(u_x_1/(u_x_1 + u_x_2)) - P_p*(v_y_1/(v_y_1
+ v_y_2)))
  dux2dz = - N*np.pi*d_0*Q_2*(P_f*(u_x_2/(u_x_1 + u_x_2)) - P_p*(v_y_2/(v_y_1
+ v_y_2)))
  dvy1dz = N*np.pi*d_0*Q_1*(P_f*(u_x_1/(u_x_1 + u_x_2)) - P_p*(v_y_1/(v_y_1 +
v_y_2)))
  dvy2dz = N*np.pi*d_0*Q_2*(P_f*(u_x_2/(u_x_1 + u_x_2)) - P_p*(v_y_2/(v_y_1 +
v_y_2)))

  return [dux1dz, dux2dz, dvy1dz, dvy2dz]
```

Model Solution

##Solving the system of ODEs

```
#Hydrogen mole fraction in feed
x_f_1 = 0.73
```

```
#CO2 mole fraction in feed

x_f_2 = 1 - x_f_1


#Total Feed flow rate

#Hydrogen feed flow rate

#CO2 feed flow rate

u_f = (2*10**5*28316.8)/(3600*22400) #mol/s

u_f_1 = u_f*x_f_1 #mol/s

u_f_2 = u_f - u_f_1 #mol/s


#Feed temperature

T_f = 250 + 273.15 #K


R = 8.314 #Universal Gas Constant in J/mol.K


#Fiber dimensions

d_i = 400*10**-6 #m

l_fiber = 1.6 #m


y0 = [u_f_1, u_f_2, 10**-20, 10**-20] #Initial conditions


z = np.linspace(0, l_fiber, 1000)
```

```
solODE = odeint(odes, y0, z)

u_x_1 = solODE[:,0]
u_x_2 = solODE[:,1]
v_y_1 = solODE[:,2]
v_y_2 = solODE[:,3]
```

Plotting the profiles

```
##Creating the DataFrame for results
df_sol = pd.DataFrame()
df_sol['Length of fiber [m]'] = z
df_sol['Retentate side flow rate (Component 1) [mol/s]'] = u_x_1
df_sol['Retentate side flow rate (Component 2) [mol/s]'] = u_x_2
df_sol['Permeate side flow rate (Component 1) [mol/s]'] = v_y_1
df_sol['Permeate side flow rate (Component 2) [mol/s]'] = v_y_2
df_sol

##Calculating permeate and retentate composition
df_sol['Mole fraction in retentate (Component 1)']=df_sol['Retentate side flow rate (Component 1) [mol/s]']/(df_sol['Retentate side flow rate (Component 1) [mol/s]']+df_sol['Retentate side flow rate (Component 2) [mol/s]'])
```

```
df_sol['Mole fraction in retentate (Component 2)']=df_sol['Retentate side flow rate (Component 2) [mol/s]']/(df_sol['Retentate side flow rate (Component 1) [mol/s]']+df_sol['Retentate side flow rate (Component 2) [mol/s]'])
df_sol['Mole fraction in permeate (Component 1)']=df_sol['Permeate side flow rate (Component 1) [mol/s]']/(df_sol['Permeate side flow rate (Component 1) [mol/s]']+df_sol['Permeate side flow rate (Component 2) [mol/s]'])
df_sol['Mole fraction in permeate (Component 2)']=df_sol['Permeate side flow rate (Component 2) [mol/s]']/(df_sol['Permeate side flow rate (Component 1) [mol/s]']+df_sol['Permeate side flow rate (Component 2) [mol/s]'])
df_sol

##Calculate total permeate and retentate flow rate
df_sol['Retentate flow rate [mol/s]']=df_sol['Retentate side flow rate (Component 1) [mol/s]']+df_sol['Retentate side flow rate (Component 2) [mol/s]']
df_sol['Permeate flow rate [mol/s]']=df_sol['Permeate side flow rate (Component 1) [mol/s]']+df_sol['Permeate side flow rate (Component 2) [mol/s]']
df_sol

##Plotting concentration profiles in permeate
fig, ax1 = plt.subplots()
ax2 = ax1.twinx()
```

```
ax1.plot(df_sol['Length of fiber [m]'], df_sol['Mole fraction in permeate (Component 1)'], 'r-')
ax2.plot(df_sol['Length of fiber [m]'], df_sol['Mole fraction in permeate (Component 2)'], 'b-')
ax1.set_ylim(0.9996, 0.9999)
ax1.set_xlim(0, 1.6)
ax2.set_ylim(0.0001, 0.0004)
ax2.set_xlim(0, 1.6)

ax1.set_xlabel('Length of fiber [m]')
ax1.set_ylabel('Permeate composition [mol/mol]')
ax2.set_ylabel('Permeate composition [mol/mol]')
plt.figlegend(['Hydrogen', 'Carbon dioxide'])
fig.suptitle('Concentration profiles (permeate)', fontsize = 12)

##Plotting concentration profiles in retentate
fig, ax1 = plt.subplots()
ax2 = ax1.twinx()

ax1.plot(df_sol['Length of fiber [m]'], df_sol['Mole fraction in retentate (Component 1)'], 'r-')
ax2.plot(df_sol['Length of fiber [m]'], df_sol['Mole fraction in retentate (Component 2)'], 'b-')
```

```
ax1.set_xlim(0, 1.6)
ax2.set_xlim(0, 1.6)

ax1.set_xlabel('Length of fiber [m]')
ax1.set_ylabel('Retentate composition [mol/mol]')
ax2.set_ylabel('Retentate composition [mol/mol]')
plt.figlegend(['Hydrogen', 'Carbon dioxide'])
fig.suptitle('Concentration profiles (retentate)', fontsize = 12)

##Plotting flow rate profiles
fig, ax1 = plt.subplots()
ax2 = ax1.twinx()

ax1.plot(df_sol['Length of fiber [m]'], df_sol['Retentate flow rate [mol/s]'], 'r-')
ax2.plot(df_sol['Length of fiber [m]'], df_sol['Permeate flow rate [mol/s]'], 'b-')

ax1.set_xlim(0, 1.6)
ax2.set_xlim(0, 1.6)

ax1.set_xlabel('Length of fiber [m]')
ax1.set_ylabel('Molar flow rate [mol/s]')
ax2.set_ylabel('Molar flow rate [mol/s]')
```

```
plt.figlegend(['Retentate flow rate', 'Permeate flow rate'])
fig.suptitle('Flow rate profiles', fontsize = 12)

df_sol

##Calculating H2 recovery and purity in permeate
y_p_1 = df_sol['Mole fraction in permeate (Component 1)'].iloc[-1]
y_p_2 = df_sol['Mole fraction in permeate (Component 2)'].iloc[-1]
x_r_1 = df_sol['Mole fraction in retentate (Component 1)'].iloc[-1]
x_r_2 = df_sol['Mole fraction in retentate (Component 2)'].iloc[-1]

print('Purity of Hydrogen product is', y_p_1*100, '%')
print('Purity of Carbondioxide in retentate is', x_r_2*100, '%')

v_p_1 = df_sol['Permeate side flow rate (Component 1) [mol/s]'].iloc[-1]
u_r_2 = df_sol['Retentate side flow rate (Component 2) [mol/s]'].iloc[-1]

Recovery_1 = v_p_1*100/u_f_1
Recovery_2 = u_r_2*100/u_f_2

print('Hydrogen recovery is', Recovery_1, '%')
print('Carbondioxide recovery is', Recovery_2, '%')
```

Bibliography

[1] N.W. Ockwig, T.M. Nenoff, Membranes for Hydrogen Separation, Chemical Reviews 107(10) (2007) 4078-4110.

[2] IEA, Global Hydrogen Review 2021 – Analysis - IEA, IEA, 2021.

[3] D. Teichmann, W. Arlt, P. Wasserscheid, Liquid Organic Hydrogen Carriers as an efficient vector for the transport and storage of renewable energy, International Journal of Hydrogen Energy 37(23) (2012) 18118-18132.

[4] G. Bernardo, T. Araújo, T. da Silva Lopes, J. Sousa, A. Mendes, Recent advances in membrane technologies for hydrogen purification, International Journal of Hydrogen Energy 45(12) (2020) 7313-7338.

[5] N. Merchant, Grey, blue, green – why are there so many colours of hydrogen? https://www.weforum.org/agenda/2021/07/clean-energy-green-hydrogen/, 2021.

[6] D.B. Pal, R. Chand, S.N. Upadhyay, P.K. Mishra, Performance of water gas shift reaction catalysts: A review, Renewable and Sustainable Energy Reviews 93 (2018) 549-565.

[7] Z. Ali, F. Pacheco, E. Litwiller, Y. Wang, Y. Han, I. Pinnau, Ultra-selective defect-free interfacially polymerized molecular sieve thin-film composite membranes for H2 purification, Journal of Materials Chemistry A 6(1) (2018) 30-35.

[8] U.S.D.o.E. Office of Fossil Energy, Washington, DC 20585, Hydrogen Strategy: Enabling A Low-Carbon Economy, 2020.

[9] J.L. Aprea, “Quality specification and safety in hydrogen production, commercialization and utilization”, International Journal of Hydrogen Energy 39(16) (2014) 8604-8608.

[10] M. Omidvar, H. Nguyen, H. Liang, C.M. Doherty, A.J. Hill, C.M. Stafford, X. Feng, M.T. Swihart, H. Lin, Unexpectedly Strong Size-Sieving Ability in Carbonized Polybenzimidazole for Membrane H2/CO2 Separation, ACS Applied Materials & Interfaces 11(50) (2019) 47365-47372.

[11] L. Hu, V.T. Bui, A. Krishnamurthy, S. Fan, W. Guo, S. Pal, X. Chen, G. Zhang, Y. Ding, R.P. Singh, M. Lupion, H. Lin, Tailoring sub-3.3 Å ultramicropores in advanced carbon molecular sieve membranes for blue hydrogen production, Science Advances 8(10) eabl8160.

[12] J.H. Bitter, A. Asadi Tashvigh, Recent Advances in Polybenzimidazole Membranes for Hydrogen Purification, Industrial & Engineering Chemistry Research 61(18) (2022) 6125-6134.

[13] S. Adhikari, S. Fernando, Hydrogen Membrane Separation Techniques, Industrial & Engineering Chemistry Research 45(3) (2006) 875-881.

[14] A. Naquash, M.A. Qyyum, Y.D. Chaniago, A. Riaz, F. Yehia, H. Lim, M. Lee, Separation and purification of syngas-derived hydrogen: A comparative evaluation of membrane- and cryogenic-assisted approaches, Chemosphere 313 (2023) 137420.

[15] L. Hu, S. Pal, H. Nguyen, V. Bui, H. Lin, Molecularly engineering polymeric membranes for H2/CO2 separation at 100–300 °C, Journal of Polymer Science 58(18) (2020) 2467-2481.

[16] M.Z. Shahid, J.-K. Kim, Design and economic evaluation of a novel amine-based CO2 capture process for SMR-based hydrogen production plants, Journal of Cleaner Production 402 (2023) 136704.

[17] B. Dutcher, M. Fan, A.G. Russell, Amine-Based CO2 Capture Technology Development from the Beginning of 2013—A Review, ACS Applied Materials & Interfaces 7(4) (2015) 2137-2148.

[18] W.A. Bollinger, D.L. Maclean, R.S. Narayan, Separation systems for oil refining and production, Chem. Eng. Prog.;(United States) 78(10) (1982).

[19] M. Galizia, W.S. Chi, Z.P. Smith, T.C. Merkel, R.W. Baker, B.D. Freeman, 50th Anniversary Perspective: Polymers and Mixed Matrix Membranes for Gas and Vapor Separation: A Review and Prospective Opportunities, Macromolecules 50(20) (2017) 7809-7843.

[20] R.W. Baker, K. Lokhandwala, Natural Gas Processing with Membranes: An Overview, Industrial & Engineering Chemistry Research 47(7) (2008) 2109-2121.

[21] R.W. Baker, B.T. Low, Gas Separation Membrane Materials: A Perspective, Macromolecules 47(20) (2014) 6999-7013.

[22] R.W. Baker, Future Directions of Membrane Gas Separation Technology, Industrial & Engineering Chemistry Research 41(6) (2002) 1393-1411.

[23] R.W. Baker, Membrane Technology and Applications (3rd edition), Wiley, West Sussex, England, UK, 2012.

[24] U.S.D.o. Energy, Basic Research Needs for the Hydrogen Economy. 2003.

[25] T.C. Merkel, M. Zhou, R.W. Baker, Carbon dioxide capture with membranes at an IGCC power plant, Journal of Membrane Science 389 (2012) 441-450.

[26] U.S.D.o. Energy, Cost and Performance Baseline for Fossil Energy Plants: Report Number DOE/NETL-2007/1281, 2007.

[27] D.E. Sanders, Z.P. Smith, R.L. Guo, L.M. Robeson, J.E. McGrath, D.R. Paul, B.D. Freeman, Energy-efficient polymeric gas separation membranes for a sustainable future: A review, Polymer 54(18) (2013) 4729-4761.

[28] L.M. Robeson, The upper bound revisited, Journal of Membrane Science 320(1–2) (2008) 390-400.

[29] L. Shao, B.T. Low, T.-S. Chung, A.R. Greenberg, Polymeric membranes for the hydrogen economy: Contemporary approaches and prospects for the future, Journal of Membrane Science 327(1) (2009) 18-31.

[30] W.J. Koros, C. Zhang, Materials for next-generation molecularly selective synthetic membranes, Nat. Mater. 16(3) (2017) 289-297.

[31] K. Atsonios, K.D. Panopoulos, A. Doukelis, A.K. Koumanakos, E. Kakaras, T.A. Peters, Y.C. van Delft, 1 - Introduction to palladium membrane technology, in: A. Doukelis, K. Panopoulos, A. Koumanakos, E. Kakaras (Eds.), Palladium Membrane Technology for Hydrogen Production, Carbon Capture and Other Applications, Woodhead Publishing2015, pp. 1-21.

[32] J.K. Das, N. Das, S. Bandyopadhyay, Highly oriented improved SAPO 34 membrane on low cost support for hydrogen gas separation, Journal of Materials Chemistry A 1(16) (2013) 4966-4973.

[33] O. Ovalle-Encinia, J.Y.S. Lin, Water-gas shift reaction in ceramic-carbonate dual-phase membrane reactor at high temperatures and pressures, Chemical Engineering Journal 448 (2022) 137652.

[34] Y. Peng, Y. Li, Y. Ban, W. Yang, Two-Dimensional Metal–Organic Framework Nanosheets for Membrane-Based Gas Separation, Angewandte Chemie International Edition 56(33) (2017) 9757-9761.

[35] Y. Peng, Y. Li, Y. Ban, H. Jin, W. Jiao, X. Liu, W. Yang, Metal-organic framework nanosheets as building blocks for molecular sieving membranes, Science 346(6215) (2014) 1356-1359.

[36] H.W. Kim, H.W. Yoon, S.-M. Yoon, B.M. Yoo, B.K. Ahn, Y.H. Cho, H.J. Shin, H. Yang, U. Paik, S. Kwon, Selective gas transport through few-layered graphene and graphene oxide membranes, Science 342(6154) (2013) 91-95.

[37] H. Li, Z. Song, X. Zhang, Y. Huang, S. Li, Y. Mao, H.J. Ploehn, Y. Bao, M. Yu, Ultrathin, Molecular-Sieving Graphene Oxide Membranes for Selective Hydrogen Separation, Science 342 (2013) 95.

[38] Z. Kang, M. Xue, L. Fan, L. Huang, L. Guo, G. Wei, B. Chen, S. Qiu, Highly selective sieving of small gas molecules by using an ultra-microporous metal–organic framework membrane, Energy & Environmental Science 7(12) (2014) 4053-4060.

[39] A. Huang, W. Dou, J.r. Caro, Steam-stable zeolitic imidazolate framework ZIF-90 membrane with hydrogen selectivity through covalent functionalization, Journal of the American Chemical Society 132(44) (2010) 15562-15564.

[40] Ø. Hatlevik, S.K. Gade, M.K. Keeling, P.M. Thoen, A.P. Davidson, J.D. Way, Palladium and palladium alloy membranes for hydrogen separation and production: History, fabrication strategies, and current performance, Separation and Purification Technology 73(1) (2010) 59-64.

[41] L. Lei, F. Pan, A. Lindbråthen, X. Zhang, M. Hillestad, Y. Nie, L. Bai, X. He, M.D. Guiver, Carbon hollow fiber membranes for a molecular sieve with precise-cutoff ultramicropores for superior hydrogen separation, Nature Communications 12(1) (2021) 268.

[42] X. Ning, W.J. Koros, Carbon molecular sieve membranes derived from Matrimid® polyimide for nitrogen/methane separation, Carbon 66 (2014) 511-522.

[43] C. Zhang, W.J. Koros, Ultraselective Carbon Molecular Sieve Membranes with Tailored Synergistic Sorption Selective Properties, Advanced Materials 29(33) (2017) 1701631.

[44] M. Rungta, L. Xu, W.J. Koros, Carbon molecular sieve dense film membranes derived from Matrimid® for ethylene/ethane separation, Carbon 50(4) (2012) 1488-1502.

[45] C. Zhang, G.B. Wenz, P.J. Williams, J.M. Mayne, G. Liu, W.J. Koros, Purification of Aggressive Supercritical Natural Gas Using Carbon Molecular Sieve Hollow Fiber Membranes, Industrial & Engineering Chemistry Research 56(37) (2017) 10482-10490.

[46] C. Zhang, R. Kumar, W.J. Koros, Ultra-thin skin carbon hollow fiber membranes for sustainable molecular separations, AIChE Journal 65(8) (2019) e16611.

[47] M. Kiyono, P.J. Williams, W.J. Koros, Effect of polymer precursors on carbon molecular sieve structure and separation performance properties, Carbon 48(15) (2010) 4432-4441.

[48] K.M. Steel, W.J. Koros, An investigation of the effects of pyrolysis parameters on gas separation properties of carbon materials, Carbon 43(9) (2005) 1843-1856.

[49] H. Hatori, H. Takagi, Y. Yamada, Gas separation properties of molecular sieving carbon membranes with nanopore channels, Carbon 42(5) (2004) 1169-1173.

[50] K. Hazazi, Y. Wang, N.M.S. Bettahalli, X. Ma, Y. Xia, I. Pinnau, Catalytic arene-norbornene annulation (CANAL) ladder polymer derived carbon membranes with unparalleled hydrogen/carbon dioxide size-sieving capability, Journal of Membrane Science 654 (2022) 120548.

[51] L. Lei, A. Lindbråthen, M. Hillestad, X. He, Carbon molecular sieve membranes for hydrogen purification from a steam methane reforming process, Journal of Membrane Science 627 (2021) 119241.

[52] S.S. Hosseini, T.S. Chung, Carbon membranes from blends of PBI and polyimides for N2/CH4 and CO2/CH4 separation and hydrogen purification, Journal of Membrane Science 328(1) (2009) 174-185.

[53] M.C. Campo, F.D. Magalhães, A. Mendes, Carbon molecular sieve membranes from cellophane paper, Journal of Membrane Science 350(1) (2010) 180-188.

[54] E.L. Wittbecker, P.W. Morgan, Interfacial polycondensation. I, Journal of Polymer Science 40(137) (1959) 289-297.

[55] M.J.T. Raaijmakers, N.E. Benes, Current trends in interfacial polymerization chemistry, Progress in Polymer Science 63 (2016) 86-142.

[56] P.W. Morgan, Condensation polymers: by interfacial and solution methods, Interscience Publishers1965.

[57] J.E. Cadotte, F. Corp, Interfacially synthesized reverse osmosis membrane, 1981.

[58] J. Glater, The early history of reverse osmosis membrane development, Desalination 117(1) (1998) 297-309.

[59] G.M. Iyer, L. Liu, C. Zhang, Hydrocarbon separations by glassy polymer membranes, Journal of Polymer Science 58(18) (2020) 2482-2517.

[60] O.M. Ekiner, G. Vassilatos, Polyaramide hollow fibers for hydrogen/methane separation — spinning and properties, Journal of Membrane Science 53(3) (1990) 259-273.

[61] O.M. Ekiner, G. Vassilatos, Polyaramide hollow fibers for H2/CH4 separation: II. Spinning and properties, Journal of Membrane Science 186(1) (2001) 71-84.

[62] C.W. Jones, W.J. Koros, Carbon molecular sieve gas separation membranes-I. Preparation and characterization based on polyimide precursors, Carbon 32(8) (1994) 1419-1425.

[63] R. Kumar, C. Zhang, A.K. Itta, W.J. Koros, Highly permeable carbon molecular sieve membranes for efficient CO2/N2 separation at ambient and subambient temperatures, Journal of Membrane Science 583 (2019) 9-15.

[64] H.D. White, C. Li, R.P. Lively, Tailoring the Structure of Carbon Molecular Sieves Derived from an Aromatic Polyamide, Industrial & Engineering Chemistry Research 61(15) (2022) 5314-5323.

[65] W.J. Koros, Membranes: learning a lesson from nature, Chemical engineering progress 91(10) (1995).

[66] W.J. Koros, G.K. Fleming, MEMBRANE-BASED GAS SEPARATION, Journal of Membrane Science 83(1) (1993) 1-80.

[67] A.L. Hines, R.N. Maddox, Mass transfer: fundamentals and applications, Prentice-Hall Englewood Cliffs, NJ1985.

[68] W.J. Koros, W.C. Madden, Transport Properties, Encyclopedia of Polymer Science and Technology2004.

[69] L. Xu, Carbon molecular sieve hollow fiber membranes for olefin/paraffin separations, (2013).

[70] D.R. Paul, W.J. Koros, Effect of partially immobilizing sorption on permeability and the diffusion time lag, Journal of Polymer Science: Polymer Physics Edition 14(4) (1976) 675-685.

[71] W.J. Koros, Barrier polymers and structures: overview, (1990).

[72] R. Haul, J. Kärger, D.M. Ruthven, Diffusion in zeolites and other microporous solids, John Wiley & Sons, Inc., New York, 1993.

[73] K.M. Steel, Carbon membranes for challenging gas separations, The University of Texas at Austin2000.

[74] O. Sanyal, S.S. Hays, N.E. León, Y.A. Guta, A.K. Itta, R.P. Lively, W.J. Koros, A Self-Consistent Model for Sorption and Transport in Polyimide-Derived Carbon Molecular Sieve Gas Separation Membranes, Angewandte Chemie International Edition 59(46) (2020) 20343-20347.

[75] J. Crank, G.S. Park, Diffusion in polymers, (No Title) (1968).

[76] A. Singh, Membrane materials with enhanced selectivity: an entropic interpretation, The University of Texas at Austin1997.

[77] M. Das, Membranes for olefin/paraffin separations, Georgia Institute of Technology2009.

[78] H. Suda, K. Haraya, Gas permeation through micropores of carbon molecular sieve membranes derived from Kapton polyimide, The Journal of Physical Chemistry B 101(20) (1997) 3988-3994.

[79] G.M. Jenkins, K. Kawamura, Polymeric carbons: carbon fibre, glass and char, Cambridge University Press1976.

[80] H.O. Pierson, Handbook of carbon, graphite, diamonds and fullerenes: processing, properties and applications, William Andrew2012.

[81] I.A.S. Edwards, H. Marsh, R. Menendez, Introduction to carbon science, Butterworth-Heinemann2013.

[82] D.Q. Vu, Formation and characterization of asymmetric carbon molecular sieve and mixed-matrix membranes for natural gas purification, (2003).

[83] M. Rungta, G.B. Wenz, C. Zhang, L. Xu, W. Qiu, J.S. Adams, W.J. Koros, Carbon molecular sieve structure development and membrane performance relationships, Carbon 115 (2017) 237-248.

[84] G.F.L. Ehlers, K.R. Fisch, W.R. Powell, Thermal degradation of polymers with phenylene units in the chain. IV. Aromatic polyamides and polyimides, Journal of Polymer Science Part A-1: Polymer Chemistry 8(12) (1970) 3511-3527.

[85] H. Hatori, Y. Yamada, M. Shiraishi, M. Yoshihara, T. Kimura, The mechanism of polyimide pyrolysis in the early stage, Carbon 34(2) (1996) 201-208.

[86] Y. Ma, M.L. Jue, F. Zhang, R. Mathias, H.Y. Jang, R.P. Lively, Creation of Well-Defined “Mid-Sized” Micropores in Carbon Molecular Sieve Membranes, Angewandte Chemie International Edition 58(38) (2019) 13259-13265.

[87] L. Xu, M. Rungta, J. Hessler, W. Qiu, M. Brayden, M. Martinez, G. Barbay, W.J. Koros, Physical aging in carbon molecular sieve membranes, Carbon 80 (2014) 155-166.

[88] S.S. Hays, O. Sanyal, N.E. León, P. Arab, W.J. Koros, Envisioned role of slit bypass pores in physical aging of carbon molecular sieve membranes, Carbon 157 (2020) 385-394.

[89] A.F. Ismail, L.I.B. David, A review on the latest development of carbon membranes for gas separation, Journal of membrane science 193(1) (2001) 1-18.

[90] S. Fu, E.S. Sanders, S.S. Kulkarni, W.J. Koros, Carbon molecular sieve membrane structure–property relationships for four novel 6FDA based polyimide precursors, Journal of Membrane Science 487 (2015) 60-73.

[91] L. Xu, M. Rungta, W.J. Koros, Matrimid® derived carbon molecular sieve hollow fiber membranes for ethylene/ethane separation, J. Membr. Sci. 380(1–2) (2011) 138-147.

[92] W. Qiu, J.E. Leisen, Z. Liu, W. Quan, W.J. Koros, Key Features of Polyimide-Derived Carbon Molecular Sieves, Angewandte Chemie International Edition 60(41) (2021) 22322-22331.

[93] X. Ma, Y.S. Lin, X. Wei, J. Kniep, Ultrathin carbon molecular sieve membrane for propylene/propane separation, AIChE Journal 62(2) (2016) 491-499.

[94] W. Ogieglo, T. Puspasari, A. Alabdulaaly, T.P. Nga Nguyen, Z. Lai, I. Pinnau, Gas separation performance and physical aging of tubular thin-film composite carbon molecular sieve membranes based on a polyimide of intrinsic microporosity precursor, Journal of Membrane Science 652 (2022) 120497.

[95] Z. Wang, H. Ren, S. Zhang, F. Zhang, J. Jin, Carbon Molecular Sieve Membranes Derived from Tröger's Base-Based Microporous Polyimide for Gas Separation, ChemSusChem 11(5) (2018) 916-923.

[96] D.-Y. Koh, B.A. McCool, H.W. Deckman, R.P. Lively, Reverse osmosis molecular differentiation of organic liquids using carbon molecular sieve membranes, Science 353(6301) (2016) 804-807.

[97] J. Liu, J. Goss, T. Calverley, G. Meyers, M.A. Thorseth, C.S. Todd, J. Kang, A. Denise, H. Clements, J. Klann, K. Mabe, L. Xu, M. Brayden, M. Martinez, Self-standing permselective CMS membrane from melt extruded PVDC, Journal of Membrane Science 615 (2020) 118554.

[98] T. Araújo, M. Andrade, G. Bernardo, A. Mendes, Stable cellulose-based carbon molecular sieve membranes with very high selectivities, Journal of Membrane Science 641 (2022) 119852.

[99] P.J. Williams, Analysis of factors influencing the performance of CMS membranes for gas separation, 2007.

[100] A. Singh-Ghosal, W.J. Koros, Air separation properties of flat sheet homogeneous pyrolytic carbon membranes, Journal of Membrane Science 174(2) (2000) 177-188.

[101] D.S. Lafyatis, J. Tung, H.C. Foley, Poly (furfuryl alcohol)-derived carbon molecular sieves: dependence of adsorptive properties on carbonization temperature, time, and poly (ethylene glycol) additives, Industrial & engineering chemistry research 30(5) (1991) 865-873.

[102] D.Q. Vu, W.J. Koros, S.J. Miller, High Pressure CO2/CH4 Separation Using Carbon Molecular Sieve Hollow Fiber Membranes, Industrial & Engineering Chemistry Research 41(3) (2002) 367-380.

[103] P.J. Williams, W.J. Koros, Gas separation by carbon membranes, Advanced membrane technology and applications (2008) 599-631.

[104] Y.K. Kim, H.B. Park, Y.M. Lee, Preparation and characterization of carbon molecular sieve membranes derived from BTDA–ODA polyimide and their gas separation properties, Journal of membrane science 255(1-2) (2005) 265-273.

[105] V.C. Geiszler, Polyimide precursors for carbon molecular sieve membranes, The University of Texas at Austin1997.

[106] M. Kiyono, Carbon molecular sieve membranes for natural gas separations, Georgia Institute of Technology2010.

[107] M. Kiyono, P.J. Williams, W.J. Koros, Effect of pyrolysis atmosphere on separation performance of carbon molecular sieve membranes, Journal of Membrane Science 359(1) (2010) 2-10.

[108] M. Kiyono, P.J. Williams, W.J. Koros, Generalization of effect of oxygen exposure on formation and performance of carbon molecular sieve membranes, Carbon 48(15) (2010) 4442-4449.

[109] R.O. Grisdale, The properties of carbon contacts, Journal of Applied Physics 24(10) (1953) 1288-1296.

[110] D.T. Clausi, W.J. Koros, Formation of defect-free polyimide hollow fiber membranes for gas separations, Journal of Membrane Science 167(1) (2000) 79-89.

[111] I.C. Omole, S.J. Miller, W.J. Koros, Increased molecular weight of a cross-linkable polyimide for spinning plasticization resistant hollow fiber membranes, Macromolecules 41(17) (2008) 6367-6375.

[112] C.-C. Chen, W. Qiu, S.J. Miller, W.J. Koros, Plasticization-resistant hollow fiber membranes for CO2/CH4 separation based on a thermally crosslinkable polyimide, Journal of membrane science 382(1-2) (2011) 212-221.

[113] H.A. Shawky, Performance of aromatic polyamide RO membranes synthesized by interfacial polycondensation process in a water–tetrahydrofuran system, Journal of Membrane Science 339(1) (2009) 209-214.

[114] J. Vaughn, Development and Evaluation of Aromatic Polyamide-imide Membranes for H2S and CO2 Separations from Natural Gas, (2013).

[115] M. Rungta, Carbon molecular sieve dense film membranes for ethylene/ethane separations, (2012).

[116] L. Liu, D. Liu, C. Zhang, High-temperature hydrogen/propane separations in asymmetric carbon molecular sieve hollow fiber membranes, Journal of Membrane Science 642 (2022) 119978.

[117] J.Y. Park, D.R. Paul, Correlation and prediction of gas permeability in glassy polymer membrane materials via a modified free volume based group contribution method, Journal of Membrane Science 125(1) (1997) 23-39.

[118] R.J. Petersen, Composite reverse osmosis and nanofiltration membranes, Journal of Membrane Science 83(1) (1993) 81-150.

[119] J.M. García, F.C. García, F. Serna, J.L. de la Peña, High-performance aromatic polyamides, Progress in Polymer Science 35(5) (2010) 623-686.

[120] J. Ren, M.R. Chowdhury, J. Qi, L. Xia, B.D. Huey, J.R. McCutcheon, Relating osmotic performance of thin film composite hollow fiber membranes to support layer surface pore size, Journal of Membrane Science 540 (2017) 344-353.

[121] G.M. Geise, D.R. Paul, B.D. Freeman, Fundamental water and salt transport properties of polymeric materials, Progress in Polymer Science 39(1) (2014) 1-42.

[122] J.-E. Gu, S. Lee, C.M. Stafford, J.S. Lee, W. Choi, B.-Y. Kim, K.-Y. Baek, E.P. Chan, J.Y. Chung, J. Bang, J.-H. Lee, Molecular Layer-by-Layer Assembled Thin-Film Composite Membranes for Water Desalination, Advanced Materials 25(34) (2013) 4778-4782.

[123] S.L. Kwolek, P.W. Morgan, Preparation of polyamides, polyurethanes, polysulfonamides, and polyesters by low temperature solution polycondensation, Journal of Polymer Science Part A: General Papers 2(6) (1964) 2693-2703.

[124] Matrimid 5218 Technical datasheet, Huntsman.

[125] S. Thomas, I. Pinnau, N. Du, M.D. Guiver, Pure- and mixed-gas permeation properties of a microporous spirobisindane-based ladder polymer (PIM-1), Journal of Membrane Science 333(1) (2009) 125-131.

[126] N. Bhuwania, Y. Labreche, C.S.K. Achoundong, J. Baltazar, S.K. Burgess, S. Karwa, L. Xu, C.L. Henderson, P.J. Williams, W.J. Koros, Engineering substructure morphology of asymmetric carbon molecular sieve hollow fiber membranes, Carbon 76 (2014) 417-434.

[127] P. Li, T.S. Chung, D.R. Paul, Gas sorption and permeation in PIM-1, Journal of Membrane Science 432 (2013) 50-57.

[128] E.P. Favvas, E.P. Kouvelos, G.E. Romanos, G.I. Pilatos, A.C. Mitropoulos, N.K. Kanellopoulos, Characterization of highly selective microporous carbon hollow fiber membranes prepared from a commercial co-polyimide precursor, Journal of Porous Materials 15(6) (2008) 625-633.

[129] P. Bénard, R. Chahine, Determination of the Adsorption Isotherms of Hydrogen on Activated Carbons above the Critical Temperature of the Adsorbate over Wide Temperature and Pressure Ranges, Langmuir 17(6) (2001) 1950-1955.

[130] D.H. Weinkauf, H.D. Kim, D.R. Paul, Gas transport properties of liquid crystalline poly(p-phenyleneterephthalamide), Macromolecules 25(2) (1992) 788-796.

[131] M. Thommes, K. Kaneko, A.V. Neimark, J.P. Olivier, F. Rodriguez-Reinoso, J. Rouquerol, K.S.W. Sing, Physisorption of gases, with special reference to the evaluation of surface area and pore size distribution (IUPAC Technical Report), 87(9-10) (2015) 1051-1069.

[132] G.M. Iyer, C. Zhang, Precise Hydrogen Sieving by Carbon Molecular Sieve Membranes Derived from Solution-Processable Aromatic Polyamides, ACS Materials Letters 5(1) (2023) 243-248.

[133] J. Jagiello, M. Thommes, Comparison of DFT characterization methods based on N2, Ar, CO2, and H2 adsorption applied to carbons with various pore size distributions, Carbon 42(7) (2004) 1227-1232.

[134] Y. Chu, A. Lindbråthen, L. Lei, X. He, M. Hillestad, Mathematical modeling and process parametric study of CO2 removal from natural gas by hollow fiber membranes, Chemical Engineering Research and Design 148 (2019) 45-55.

[135] X. Ma, I. Pinnau, A novel intrinsically microporous ladder polymer and copolymers derived from 1,1′,2,2′-tetrahydroxy-tetraphenylethylene for membrane-based gas separation, Polymer Chemistry 7(6) (2016) 1244-1248.

[136] J. Park, K.E. Gaines, L.-C. Jheng, J.S. Riffle, S.J. Mecham, J.E. McGrath, H.B. Park, D.R. Paul, B.D. Freeman, Characterization and gas transport properties of UV-irradiated polydimethylsiloxane (PDMS)-containing polyimide copolymer membranes, Polymer 210 (2020) 122966.

[137] M.R. Kosuri, W.J. Koros, Defect-free asymmetric hollow fiber membranes from Torlon®, a polyamide–imide polymer, for high-pressure CO2 separations, Journal of Membrane Science 320(1) (2008) 65-72.

[138] W.F. Yong, F.Y. Li, T.S. Chung, Y.W. Tong, Molecular interaction, gas transport properties and plasticization behavior of cPIM-1/Torlon blend membranes, Journal of Membrane Science 462 (2014) 119-130.

[139] H.-Y. Jang, J.R. Johnson, Y. Ma, R. Mathias, D.A. Bhandari, R.P. Lively, Torlon® hollow fiber membranes for organic solvent reverse osmosis separation of complex aromatic hydrocarbon mixtures, AIChE Journal 65(12) (2019) e16757.

[140] K. Li, Q. Li, Z. Cai, Y. Weng, C. Ye, W. Ji, J. Li, B. Cheng, X. Ma, Microporosity effect of intrinsic microporous polyimide membranes on their helium enrichment performance after direct fluorination, Journal of Membrane Science 660 (2022) 120868.

[141] J. Garrido, A. Linares-Solano, J.M. Martin-Martinez, M. Molina-Sabio, F. Rodriguez-Reinoso, R. Torregrosa, Use of nitrogen vs. carbon dioxide in the characterization of activated carbons, Langmuir 3(1) (1987) 76-81.

[142] W. Ouyang, D. Zeng, X. Yu, F. Xie, W. Zhang, J. Chen, J. Yan, F. Xie, L. Wang, H. Meng, D. Yuan, Exploring the active sites of nitrogen-doped graphene as catalysts for the oxygen reduction reaction, International Journal of Hydrogen Energy 39(28) (2014) 15996-16005.

[143] A. Ganguly, S. Sharma, P. Papakonstantinou, J. Hamilton, Probing the Thermal Deoxygenation of Graphene Oxide Using High-Resolution In Situ X-ray-Based Spectroscopies, The Journal of Physical Chemistry C 115(34) (2011) 17009-17019.

[144] J. Ren, J.R. McCutcheon, Making Thin Film Composite Hollow Fiber Forward Osmosis Membranes at the Module Scale Using Commercial Ultrafiltration Membranes, Industrial & Engineering Chemistry Research 56(14) (2017) 4074-4082.

[145] S. Fu, E.S. Sanders, S.S. Kulkarni, W.J. Koros, Carbon molecular sieve membrane structure–property relationships for four novel 6FDA based polyimide precursors, J. Membr. Sci. 487 (2015) 60-73.

[146] Y.-H. Chu, D. Yancey, L. Xu, M. Martinez, M. Brayden, W. Koros, Iron-containing carbon molecular sieve membranes for advanced olefin/paraffin separations, Journal of Membrane Science 548 (2018) 609-620.

[147] C.Y. Feng, K.C. Khulbe, T. Matsuura, A.F. Ismail, Recent progresses in polymeric hollow fiber membrane preparation, characterization and applications, Separation and Purification Technology 111 (2013) 43-71.

[148] M. Khayet, M.C. García-Payo, X-Ray diffraction study of polyethersulfone polymer, flat-sheet and hollow fibers prepared from the same under different gas-gaps, Desalination 245(1) (2009) 494-500.

[149] C. Cao, T.-S. Chung, S.B. Chen, Z. Dong, The study of elongation and shear rates in spinning process and its effect on gas separation performance of Poly(ether sulfone) (PES) hollow fiber membranes, Chemical Engineering Science 59(5) (2004) 1053-1062.